Characterization of Semiconductor-Based Guided Wave Structures Using Field Theoretical Analysis Techniques

by
Shuoqi Chen
B. Sc., Xiamen University, China, 1982
M. Sc. Nanjing Electronic Devises Institute, China, 1988

A Dissertation Submitted in Partial Fulfillment of the
Requirements for the Degree of

DOCTOR OF PHILOSOPHY

in the Department of
Electrical & Computer Engineering

We accept this dissertation as conforming
to the required standard

Dr. R. Vahldieck, Supervisor (Dept. of Elec. & Comp. Engineering)

Dr. W.J.R. Hoefer, Department Member (Dept. of Elec. & Comp. Engineering)

Dr. M.A. Stuchly, Department Member (Dept. of Elec. & Comp. Engineering)

Dr. S. Dost, Outside Member (Dept. of Mechanical Engineering)

Dr. K. Wu, External Examiner (Dept. de Génie Électrique et de Génie Informatique, École Polytechnique de Montréal)

Supervisor: Dr. R. Vahldieck

ABSTRACT

In this dissertation, a variety of semiconductor based transmission lines are investigated. Among them are metal-insulator-semiconductor (MIS) coplanar waveguide (CPW) slow-wave structures and laser diodes. Although laser diodes are electro-optic devices, their microwave parameters are of great importance for broadband matching to their driver networks. It will be shown that, besides their optical characteristics, laser diodes can be regarded as bias-dependent lossy and dispersive slow-wave transmission lines for the driving RF/microwave signal.

The analysis of this kind of transmission lines is very difficult or even impossible through a single numerical approach. Therefore, in this thesis a combination of two methods is applied, namely, the complex finite difference method (CFDM) and the frequency-domain transmission line matrix (FDTLM) method. The CFDM provides a self-consistent solution to the semiconductor equations, which determines the conductivity distribution in the semiconductor layer as a function of the bias current. The FDTLM method utilizes this information to calculate the microwave characteristics of such a multilayered, lossy transmission line.

The development of the CFDM, based on information available from the literature, is described in detail. For the FDTLM method, an investigation is presented analyzing the errors of the various node representations. On the basis of this investigation, a new node, the hybrid node with shunt decomposition, is developed. This node shows better accuracy than other nodes and is particularly well suited for the analysis of lossy, semiconductor-based structures. Furthermore, by using finite differencing and averaging, the theoretical foundation of the FDTLM method is expanded and, for the first time, a direct relationship between the electromagnetic field and the voltages and currents in the hybrid node with shunt decomposition is established.

On the basis of the numerical techniques developed in the first part of the thesis, mode propagation and scattering of electromagnetic field in a variety of semiconductor-

based structures are investigated. Besides the microwave effects in semiconductor lasers and the slow-wave characteristics in MIS CPW structures, the second part of this thesis concentrates on the scattering of fields at discontinuities between transmission lines. This includes wire bond and flip-chip transitions between transmission lines and laser diodes as well as direct transitions, for example, between slow-wave CPW structures on doped silicon and CPW on the same but an undoped substrate.

Whenever possible, these results are compared with those from other methods and measurements. However, since most of the structures and transitions considered in this thesis are investigated for the first time, the data available in the open literature is limited. From the comparison of obtained results with the available data and measurements one can safely conclude that the numerical analysis presented for all structures is a true picture of the physical reality.

Examiners:

Dr. R. Vahldieck, Supervisor (Dept. of Elec. & Comp. Engineering)

Dr. W.J.R. Hoefer, Department Member (Dept. of Elec. & Comp. Engineering)

Dr. M.A. Stuchly, Department Member (Dept. of Elec. & Comp. Engineering)

Dr. S. Dost, Outside Member (Dept. of Mechanical Engineering)

Dr. K. Wu, External Examiner (Dept. de Génie Électrique et de Génie Informatique, École Polytechnique de Montréal)

Table of Contents

List of Tables

List of Figures

Acknowledgements

I would like to gratefully acknowledge my supervisor, Dr. R. Vahldieck, not only for his continuous support and encouragement, but also for his help and many new ideas he has contributed during the course of this research.

I am also grateful to Dr. H. Jin and Dr. J. Huang for helping me getting started with the frequency-domain TLM method and for their encouragement and discussion on many aspects of the research work. It is my pleasure to thank my colleagues in the LLIMIC research group at the University of Victoria for their association and support. Special thanks also to Dr. M. Kim, Philips Laboratories, North American Philips Corp. for helpful discussions and for providing the measurements for the slow-wave structures.

I express my full gratitude to all members of my family, especially my wife Dr. Q. Zhang, for her consistent encouragement and helpful discussions.

Finally, the financial assistance by a Graduate Research Engineering and Technology (GREAT) Award from the Science Council of British Columbia, MPR Teltech, and Seastar Optics during the period of this research is acknowledged with gratitude.

Dedication

To my parents,

my wife Qi Zhang

and my daughter Susan Chen

Chapter 1

Introduction

1.1 Numerical Modeling of Planar Microwave Structures on Insulating and Semiconducting Substrates

With the progress of the monolithic microwave integrated circuits (MMICs) and optical monolithic integrated circuits (OMICs) engineering, RF and microwave technology have become an integrate part of modern wireless communication systems and high-capacity microwave/fiber optic links. MMIC and OMIC technologies integrate all passive and active components such as planar or coplanar transmission lines, resistors, capacitors, inductors, transistors, diodes, laser diodes, photodetectors and modulators on a single chip for a given circuit function. By using monolithic integrated circuits, the parasitic reactances associated with the packages and bonding wires can be reduced to minimum and in general, the circuit response can be improved. In addition, there are several advantages of using MMICs in different applications: (1) the availability of the compound semiconductors such as GaAs and InP, which provide high electron mobility, (2) the availability of the semi-insulating substrates on which it is possible to fabricate the low-loss planar or coplanar transmission lines for interconnection and signal delay such as microstrip and coplanar waveguide (CPW), (3) the availability of various expitaxial growth techniques to produce multi-layered device structures, (4) the availability of computer aided design (CAD) software for circuit performance optimization. One of the important features of MMICs or OMICs engineering is that these systems rely heavily on miniature-sized planar or coplanar transmission lines on

insulating or semiconducting substrates with complicated three-dimensional (3D) conductor structures which, for active devices and metal-insulator-semiconductor (MIS) structures, contain also multi-layered dielectrics with inhomogeneous properties. The complexity of these transmission lines makes the microwave circuit design difficult and requires, in general, field theory-based numerical modeling of circuit discontinuities to accurately characterize their effects on the overall circuit performance. Developing numerical methods that provide accurate simulations of electromagnetic fields in generalized transmission line structures is indeed a challenging research topic.

Over the past 20 years, a large number of research articles has been published on this topic. The presence of inhomogeneous dielectric layers with doped regions and varying doping depths is usually excluded or included only with rough approximations. However, these effects become more and more important, the higher the integration level of microwave and RF components become, the numerical analysis methods used must be capable of handling very general three-dimensional configurations.

Numerical modeling is concerned with the representation of physical systems by specific quantities which can be obtained through numerical methods. For electromagnetic systems, it is generally required to obtain the electric and magnetic fields within a volume of space, subject to appropriate boundary conditions. There are several numerical methods for solving electromagnetic field problems that have been well established, each possessing unique features that are advantageous to a particular type of problems or structures [1, 2]. These methods can be classified into generic groups based on the domain of the variable (time or frequency domain) and the type of the operator (differential or integral). Hybrid methods involving more than one technique have also been developed. A hybrid analysis or combination of several numerical techniques is often necessary to solve a given problem efficiently. The guided wave problem associated with semiconductor-based transmission lines (lossy media) will be extensively studied in this dissertation. The method adopted for this work is mainly based on the frequency-domain transmission line matrix (FDTLM) method, which can be classified as a differential frequency domain method based on the time-harmonic Maxwell's equations. This method is also known as

the frequency-domain counterpart of the time-domain TLM method.

For the semiconductor laser problem, wide bandwidth directly modulated laser diodes are attractive for microwave/fiber optical links. A crucial step in the design of integrated circuit is the fabrication of low-threshold-current laser diodes, in which the relaxation oscillation frequency as well as frequency bandwidth can be extended by driving laser diodes to higher current levels. At the same time it is important to integrate laser diodes with their driving circuits to reduce parasitic effects introduced by commonly used wire bond interconnections to the microwave circuitry. In this context the transition between the microwave circuit and the lasers must be designed with impedance matching in mind. To find the characteristic impedance of laser diodes, the traditional approach is to represent a laser diode by a lumped element circuit. At low modulation frequencies this approach is usually acceptable because of the short length of the laser cavity (~300 μm). However, at modulating frequencies in excess of 20 GHz, the distributed microwave effect becomes a dominant factor. Under these circumstances, only a rigorous electromagnetic field analysis can characterize the structure accurately. This applies also to the characterization of the interconnection with passive microwave transmission lines, *i.e.* microstrip line or coplanar waveguide (CPW). In this problem, Maxwell's equations and the static-state semiconductor device equations must be solved consistently by using a combination of numerical methods, such as a combination of the frequency-domain transmission line matrix (FDTLM) method and the extended complex finite difference (ECFD) method as presented in this thesis. In this combination, the active device problem is first solved for the static-state case to yield the bias-dependent parameters. Then, the semiconductor laser is further treated as a lossy, slow-wave and dispersive multilayer microwave transmission line with a conductivity distribution of the active layers as determined by the ECFD method. Its microwave characteristics are then determined by the FDTLM method.

The analysis of the laser diode was followed by a groundwork laid for research on other semiconductor-based transmission lines. MIS transmission lines are one of those known to support slow-wave mode propagation. This phenomenon has been observed

both experimentally and theoretically and the physics behind it has been explained from different points of views. The slow-wave properties of such transmission lines can be used to reduce the circuit dimensions by a factor of 10 ~ 20, which is very attractive for MMICs in the frequency range of 1 GHz ~ 2 GHz. Potential applications are in pulse delay circuits for phased arrays, electronically controlled phase shifters and filters, and high speed integrated circuits for reducing crosstalk. However, the slow-wave mode propagation in those transmission lines comes at the price of relatively high losses and low Q-factors, which is a problem that has prevented the widespread use of these transmission lines in the past. Generally, a thin film lossy doping layer is less lossy than a thick one. To reduce losses, it is known that the electric field must be confined in the insulating layer, but the slow-wave factor also be reduced. Hence, a compromise must be found between maximum slow-wave factor and minimum losses by either carefully controlling the doping layer thickness, or limiting the lateral width of the doping region. To predict accurately the dimensions of the structure for optimum slow-wave characteristics, full wave electromagnetic field simulation is required. In this thesis, this task is accomplished by using the frequency-domain TLM method alone since the doping distribution depends only on the doping process and can be determined analytically.

The FDTLM method is a versatile numerical simulation tool for electromagnetic scattering problems in guided wave structures. This method was originally derived from the time-domain TLM method [3, 4]. The FDTLM method presents a complementary tool to the time-domain TLM (TDTLM) method. As such, it expands the framework of the TLM technique to algorithms in both time and frequency domain, whereby in both domain the same space discretization network can be utilized.

Although the frequency-domain response of a circuit can be obtained directly from the time domain output data of the TDTLM method by means of a Fourier transform, this may not always be a computationally efficient approach if a guided wave structure needs to be characterized at only a few frequencies or the material constitutive parameters are frequency-dependent. In this case the computation of the entire transient response, as required in the TDTLM method, appears to be an unnecessary computational expense. To

avoid this problem, a first attempt of formulating the TLM algorithm directly in the frequency-domain was described in 1980 [5]. However, it was not until 1992 that this idea was revisited [6, 7, 8] and a more complete algorithm was developed to the FDTLM.

The concept of the frequency-domain TLM method, including frequency-domain symmetrical condensed nodes (SCN) and a novel S-parameter extraction technique, was first introduced by Jin and Vahldieck [6, 7]. At about the same time a TLM technique for steady-state field solution was published by Johns, *et al* [8]. Both approaches, although developed independently, share the following common features that distinguish them from the time-domain TLM method: First, no impulse excitation is required. The transmission line network is considered to be in steady-state. Second, the same transmission line network as in the TDTLM can be utilized to discretize the computational domain. Third, there is more flexibility in the FDTLM concerning the space discretization since the modeling of media with arbitrary constitutive parameters becomes possible without the need for reactive stubs. All these features lead to a number of computational advantages for the FDTLM that can be summarized as follows: No time discretization and thus no time iterations are necessary; since time synchronism need not be preserved, graded mesh layouts with larger grading ratios can be utilized (the grading ratio is only limited by the acceptable numerical dispersion error); for isotropic substrates the node scattering matrix is always a 12x12 matrix, irrespective whether homogeneous or inhomogeneous structures are investigated. The network theory can be applied to greatly enhance the numerical versatility, efficiency and accuracy of the frequency-domain computations. Therefore, most of the numerical investigations presented in this thesis are based on the FDTLM method.

1.2 The Objective of the Dissertation

The objective of this research work is to analyze electromagnetic fields in a class of semiconductor-based microwave transmission lines and to characterize the scattering of fields at discontinuities between transmission line on insulating and semiconducting substrates. Two typical structures are considered in the dissertation. The first structure is a

semiconductor laser diode and its interconnection with a normal microwave transmission line by using flip-chip and airbridge/bond wire techniques. This investigation reveals the nature of the microwave effect in a semiconductor laser and quantifies the parameters in the design of transitions between passive microwave transmission lines and active devices. In this phase, a two-step numerical approach is developed which combines the FDTLM symmetrical condensed node (SCN) scheme with the complex finite difference method is developed. In this simulation the field problem of the semiconductor device is solved for the static-state case to derive the bias-dependent conductivity distribution over the laser cross-section. Subsequently, the laser is regarded as a lossy microwave transmission line, for which the propagation parameters are determined from a FDTLM analysis.

The second structure is a semiconductor-based metal-insulator-semiconductor (MIS) coplanar waveguide (CPW) with a laterally inhomogeneous doping profile. After a systematic development of the symmetrical condensed node in the frequency-domain, a rigorous field theoretical analysis of slow-wave propagation in this structure is presented. The structure is similar to the laser chip but less complicated because the doping distribution is determined by the fabrication process alone and can be calculated explicitly. After the doping distribution obtained, the FDTLM method is then applied to determine the propagation characteristics. For the first time in the literature also the abrupt transition between MIS CPW and transmission lines on insulating substrate is presented.

1.3 Contributions of the Dissertation

The main contributions of the dissertation can be summarized as follows:

1) The results presented in this dissertation give a better understanding of the behavior of electromagnetic fields in complicated semiconductor-based guided wave structures.

2) A combination of numerical techniques has been developed systematically to analyze the microwave distributed effect and the transition effects of laser diodes. The

transition between microwave transmission lines and active devices through flip-chip and airbridge/bond wire techniques is a truly three-dimensional problem which has previously not been investigated rigorously.

3) Using a generalized symmetrical condensed node in the frequency domain, the FDTLM scheme has been applied for the first time to solve the eigenvalue problem in slow-wave MIS CPW with a lateral inhomogeneous doping profile. This research also includes the analysis of three-dimensional field scattering at the discontinuity between slow-wave MIS CPW and normal microwave transmission lines on an insulating substrate. An investigation of the latter problem has not been reported before in the literature.

4) The FDTLM method has been further improved by generalizing the SCN to allow for link lines with different characteristic impedances and propagation constants which can be of either real or complex values. A methodology has been proposed for directly deriving the scattering properties of the frequency-domain symmetrical condensed node both from the equivalent circuit model as well as directly from the time-harmonic Maxwell's equations. The latter is based on the initial work by Jin and Vahldieck [9]. Hence, a rigorous field theoretical foundation was successfully built for all the FDTLM nodes.

5) A detailed analysis of the dispersion relations for the different frequency-domain TLM SCNs is presented based on the general dispersion equation with respect to the port scattering matrix of the SCN. A detailed comparison of the propagation errors for the SCNs in the frequency domain is presented.

1.4 Overview of the Dissertation

The objective of this section is to demonstrate the structure of the research work described in the following chapters. The research work consists of mainly two parts: First, further development of the frequency-domain symmetrical condensed node TLM scheme and combination with a finite difference method to model semiconductor laser

physics. Second, the application of this numerical approach to model the electromagnetic field in practical semiconductor-based transmission lines.

In Chapter 2, a three-dimensional (3D) self-consistent numerical approach for semiconductor lasers with strip discontinuities along the longitudinal direction is presented in detail. The specific features of the transverse distribution of the bias-dependent conductivity profile in the active region is used in the later chapters to simulate the transition between a laser diode and passive microwave transmission lines.

Chapter 3 introduces the general frequency-domain constitutive relation, which provides the basic framework formulating the FDTLM parameters with six degrees of freedom. Based on the general scattering procedure in the symmetrical condensed node and the new node port numbering, a simple and elegant procedure of deriving the scattering properties of the FDTLM SCNs is presented.

In Chapter 4, the scattering equations of a frequency-domain TLM symmetrical condensed node is derived directly from the time-harmonic Maxwell's equations by using centered differencing and averaging scheme. Based on this derivation, a direct correspondence between the general FDTLM condensed nodes and the finite difference scheme will be established. This approach provides a rigorous field theoretical foundation for the FDTLM SCNs. Furthermore, by applying the equivalent network modeling scheme, the lossy stub-loaded symmetrical condensed node (LSLSCN) and the general lossy stub-loaded symmetrical condensed node (GLSLSCN) are introduced.

Chapter 5 concentrates on the propagation errors of the frequency-domain SCNs. The complete dispersion characteristics of a class of frequency-domain symmetrical condensed TLM nodes is investigated based on the numerical solution of the dispersion eigenvalue equation.

Chapter 6 is the results section. A rigorous field theory analysis of the microwave effects and electromagnetic field propagation in semiconductor-based guided wave structures is pursued using the FDTLM method. Applications of the method and

discussions are focused on the semiconductor laser diode analysis, transition characteristics for junctions between passive microwave transmission lines and active devices by flip-chip or airbridge (or bond wire) techniques, as well as the mode propagation and field scattering in semiconductor-based coplanar metal-insulator-semiconductor (MIS) slow-wave structures with a laterally inhomogeneous doping profile.

Chapter 7 presents an overall discussion and conclusion of the dissertation and proposes possible future research directions.

Chapter 2

Semiconductor Waveguide: Modeling of Electromagnetic Field Propagation in Laser Devices

2.1 Introduction

Microwave/fiber optic links require semiconductor laser chips viewed from electrical side that can be modulated over a broad frequency range. The parasitic reactances and impedance mismatching are the major effects limiting these broadband applications. Usually the modulation frequencies are below 15GHz because of large packaging parasitic parameters. However, recently high speed laser structures have been reported with modulation frequencies above 20GHz [10, 11]. When the modulation frequencies are far beyond 20GHz, the wavelength becomes compatible with the lasers dimensions (approximately 300 μm long) and a distributed microwave effect along the laser chip occurs. This was found experimentally in a recent paper by Tauber *et. al.* [12]. The results of analysis and measurement have shown that the laser diode exhibit a slow-wave effect due to the highly doped layers. The propagation of the modulating microwave signal in the laser diode is therefore very lossy and dispersive [12]. Because of interaction of electrons and photons, a laser diode can be considered as an active microwave transmission line. To analyze its microwave effect, the simple distributed circuit model described in [12] presents only a first-order approximation of the propagation characteristics. It is very important that a more accurate characterization of the distributed microwave effect is provided to aid the integration of RF and optical design in terms of

better electrical performance. As a first step towards this goal the laser diode is described as a multilayer semiconducting substrate microstrip transmission line. Electrically, the biasing currents and the microwave modulation signals change the conductivity profile in the laser active layer which are dependent upon the carrier density distribution. Optically, the near-field modes are confined by the local gain profile and the refractive index profile, which are also dependent upon the carrier density distribution. Consequently, the basic physical phenomena that need to be considered in describing the microwave behavior of laser diodes are based on: 1) current spreading in the confining layer, and 2) lateral carrier diffusion in the active layer beneath the electrode strip.

Numerical techniques that have been developed for passive transmission lines can be utilized to incorporate a self-consistent scheme, which solves Poisson's equations and the carrier continuity equations simultaneously. If the laser diode is only regarded as a 2D discontinuity (no longitudinal change in the refractive index or in the electrode strip dimensions), this problem has been solved in the literature [14-22]. For the cases, however, in which the bias current contact pad is wider than the electrode strip, the 2D model will not be valid anymore since the current spreading and the carrier density distribution are constant in longitudinal direction. These changes affect the laser mode profile as well as the microwave characteristics of the laser diodes and therefore require a 3D treatment of the problem.

In this chapter, a 3D self-consistent numerical approach for single and double heterojunction (DH) strip lasers with strip discontinuities along the longitudinal direction. This technique is based on the complex finite difference method and takes into account the complex refractive index in the active layer which is a function of the bias current. The important feature here is that the imaginary part of the refractive index represents optical gain or loss which, in gain-guided lasers, is a function of the location of the electrode strip. Furthermore, the transverse distribution of the conductivity profile must be known for any calculation of the complex impedance of the laser diode and the transition between a laser diode and passive microwave transmission lines (i.e. microstrip or CPW). The imaginary part of the dielectric permittivity represents the conductivity corresponding to injection

carriers (inhomogeneous) or impurity doping (homogeneous). The conductivity profile in the active layer is obtained by a self-consistent solution of the nonlinear semiconductor device equations.

In the following we provide the numerical algorithm to analyze DH semiconductor lasers with single and double electrode strip containing discontinuities in longitudinal direction of the electrode. Single and double strip laser mode profiles as a function of the biasing current will be presented. The complex propagation constant, the current and the carrier distribution at the interface of the active region will be described. The algorithms will be implemented and validated.

2.2 Semiconductor Laser Device Modeling

Traditionally, the electric behavior of semiconductor media is described by the equations from semiconductor device physics. In this section, we will briefly review the conventional semiconductor device equations. For photoelectronic devices, such as semiconductor laser diodes, the equations have to be extended to include the wave and photon rate equations in order to model photon generation and propagation. Modeling of semiconductor laser diodes is based on device physics which includes the carrier drift caused by the field and diffusion caused by the carrier concentration gradient, photon emission (spontaneous and stimulated emission), and electromagnetic fields propagation.

2.2.1 Basic Semiconductor Laser Device Equations

The physics of semiconductor lasers is very different from other semiconductor devices in the following respects. First, a laser diode is composed of an optical waveguide structure and both stimulated and spontaneous emissions occur. Second, heterojunctions are the key building blocks of semiconductor lasers. Third, carrier degeneracy occurs in the active layers where large concentrations of carriers are injected. The basic equations of a semiconductor laser device describe the static and dynamic behavior of carriers, the generation of photons and their recombination of electron-hole pairs in the semiconductor, as well as the electromagnetic wave propagating in the semiconductor waveguide. The

motion of these carriers is influenced by the external fields that cause deviation from the thermal-equilibrium conditions. Therefore, the semiconductor lasing operation can be considered by the following four groups of equations: Maxwell's equations which include the wave equation, current density equations, carrier continuity equations [13] and the photon rate equation [14].

Maxwell Equations:

$$\nabla \times \boldsymbol{E} = -\frac{\partial \boldsymbol{B}}{\partial t} \tag{2.1a}$$

$$\nabla \times \boldsymbol{H} = \frac{\partial \boldsymbol{D}}{\partial t} + \boldsymbol{J}_{cond} \tag{2.1b}$$

$$\nabla \cdot \boldsymbol{D} = \rho \tag{2.1c}$$

$$\nabla \cdot \boldsymbol{B} = 0 \tag{2.1d}$$

where $\boldsymbol{E}$ is the electric field intensity, $\boldsymbol{H}$ is the magnetic field intensity, $\boldsymbol{D}$ is the electric flux density, $\boldsymbol{B}$ is the magnetic flux density, $\boldsymbol{J}_{cond}$ is the conduction electric current density which includes both electron and hole current components in semiconductors, and ρ is the electric charge density. In media the constitutive relations can be represented as

$$\boldsymbol{D} = \varepsilon \boldsymbol{E} \tag{2.2}$$

$$\boldsymbol{B} = \mu \boldsymbol{H} \tag{2.3}$$

where ε is the permittivity and μ the permeability of the medium. Both of them can be complex scalars or tensors. In semiconductor device physics, the most important is Gauss law, Eq. (2.1c), which determines the properties of the *p-n* junction. For a semiconductor laser, the Poisson equation can be written in terms of the electrostatic potential V as follows [13]:

$$\nabla \cdot (\varepsilon \nabla V) = -q\left(p - n + N_D^{+} - N_A^{-} \right) \tag{2.4}$$

where n and p are respectively the electron and hole density, and N_D^{+} and N_A^{-} are the concentrations of ionized donors and acceptors. The dielectric constant ε is space-

dependent in heterostructure devices.

The optical field, $\boldsymbol{E}(x, y)$, in the laser device satisfies the following Helmholtz wave equation which can be directly derived from Maxwell's curl equations in (2.1a) and (2.1b):

$$\nabla^2 \boldsymbol{E}(x, y) + \left(k_0^2 \tilde{n}^2 - \beta^2\right) \boldsymbol{E}(x, y) = 0 \tag{2.5}$$

where $\boldsymbol{E}(x, y)$ is the electrical field vector of a wave propagating in the z direction. The orientation of the axes has the x direction in parallel and the y direction perpendicular to the heterojunction. β is the mode propagation constant, k_0 ($=2\pi/\lambda_0$) is the free space wave number with the emission wavelength λ_0. $\tilde{n}$ is the complex refractive index, which can be expressed in terms of the background (bulk) refractive index n_0 and the local gain factor.

Continuity Equations for electrons and holes are as follows:

$$\frac{\partial n}{\partial t} = G_n - U_n + \frac{1}{q} \nabla \cdot J_n \tag{2.6}$$

$$\frac{\partial p}{\partial t} = G_p - U_p + \frac{1}{q} \nabla \cdot J_p \tag{2.7}$$

where G_n and G_p are the electron and hole generation rate, respectively, caused by an external influence such as optical excitation with high-energy photons or ionization under large electric fields. U_n and U_p are the electron recombination rate in p-type semiconductor and the hole recombination rate in n-type semiconductor, respectively.

Current Density Equations [13] are:

$$J_n = q\mu_n n E + qD_n \nabla n \tag{2.8}$$

$$J_p = q\mu_p p E - qD_p \nabla p \tag{2.9}$$

$$J_{cond} = J_n + J_p \tag{2.10}$$

where J_n and J_p are the electron current density and the hole current density, respectively. μ_n and μ_p denote the carrier mobilities for electrons and holes. D_n and D_p are electron and hole diffusion coefficients, respectively. They consist of the drift component caused by the

field and the diffusion component caused by the carrier concentration gradient. These equations are valid for low electric fields. For sufficiently high fields the term $\mu_n E$ or $\mu_p E$ should be replaced by the saturation velocity v_s. Under nonisothermal conditions, an additional thermal diffusion current arises from temperature gradients. The current densities are then expressed by [15, 16, 17]

$$J_n = q\mu_n nE + qD_n \nabla n + qD_n^T \nabla T \tag{2.11}$$

$$J_p = q\mu_p pE - qD_p \nabla p - qD_p^T \nabla T \tag{2.12}$$

where D_n^T and D_p^T are electron and hole thermal diffusion coefficients, respectively.

Photon Rate Equation is:

$$\frac{dS}{dt} = \left(\frac{c_0}{n_{eff}} G_m - \frac{1}{\tau_{ph}} \right) S + CR_{sp} \tag{2.13}$$

where S is the photon density. c_0 is the light velocity in free space. n_{eff} is the effective refractive index. G_m denotes the mth mode gain. τ_{ph} is the photon lifetime. C denotes the spontaneous-emission factor. R_{sp} is the spontaneous-emission rate. Under the steady-state condition, the photon rate equation, after neglecting the spontaneous emission, can be written as

$$G_m = \alpha_T \tag{2.14}$$

where the modal gain is calculated by the local gain with the optical intensity,

$$G_m = \iint g(x,y) \left| E_m(x,y) \right|^2 dx\, dy \;/\; \iint \left| E_m(x,y) \right|^2 dx\, dy \tag{2.15}$$

The total loss, α_T, includes the bulk loss α_a, the free carrier absorption α_{fc} and the mirror loss α_m,

$$\alpha_T = \alpha_a + \alpha_{fc} + \alpha_m \tag{2.16}$$

where α_a and α_{fc} are the average loss of the local bulk and free carrier absorption loss. They are defined as:

$$\alpha_a = \iint \alpha'_a |E_m|^2 dx\, dy \,/\, \iint |E_m|^2 dx\, dy \tag{2.17}$$

$$\alpha_{fc} = \iint \alpha'_{fc} |E_m|^2 dx\, dy \,/\, \iint |E_m|^2 dx\, dy \tag{2.18}$$

where α'_a is the absorption coefficient and α'_{fc} is given by [14][18]:

$$\alpha'_{fc}[cm^{-1}] = 3\times 10^{-18} n + 7\times 10^{-18} p \tag{2.19}$$

The mirror loss, α_m, can be expressed as:

$$\alpha_m = \frac{1}{2L_c} \ln \frac{1}{R_f R_r} \tag{2.20}$$

where L_c is the cavity length, R_f and R_r are the front and rear facet reflectivities, respectively. The photon rate equation couples the optical equation and electrical equations through the photon density. When the device is under low bias, the modal gain G_m is less than the total loss α_T giving a photon density of zero. When the bias is increased to threshold value, where G_m becomes somewhat larger than α_T, the photon density S increases. The increase of the photon density leads to increasing stimulated emission transitions which causes the decrease of the carrier concentration that maintains the equality $G_m = \alpha_T$. This determines the steady-state photon density.

To complete the laser model, it is necessary to calculate the output power using the following expression [14, 15]:

$$\begin{aligned} P &= h\nu \eta_D \iiint \frac{S}{\tau_{ph}} dxdydz \\ &= \frac{hc_0^2 S}{2\lambda_0 n_{eff}} \cdot \frac{\ln(1/R_f R_r)}{1+\sqrt{R_f/R_r}(1-R_r)/(1-R_f)} \cdot \iint |\tilde{E}|^2 dxdy \end{aligned} \tag{2.21}$$

where $h\nu$ is the photon energy, η_D the differential quantum efficiency, and τ_{ph} the photon lifetime which is expressed as follows under the oscillation condition [14]:

$$\frac{1}{\tau_{ph}} = \frac{c_0}{n_{eff}} (\alpha_a + \alpha_{fc} + \alpha_m) = \frac{c_0}{n_{eff}} G_m \tag{2.22}$$

2.2.2 Theoretical Analysis of Semiconductor DH Lasers

Figure 2.1 shows the semiconductor laser configuration with a double-heterostructure (DH). The representation of the DH laser is a three layer dielectric slab waveguide. The active layer of the laser diode is assumed to be an intrinsic or lightly-doped *n*-type semiconductor medium such as GaAs or InGaAsP. Transverse confinement of the carriers and optical field in the active layer is provided by two relatively wide bandgap passive *p*-type and *n*-type cladding layers on either side to form a slab optical waveguide. However, in the lateral direction there is no well-defined guiding structure, and a weak waveguiding is provided by the lateral variation of the refractive index due to the spatial variation in the injected carriers. Below the electrode strip the carrier concentration depends on the level of injected current, which in turn defines the region of maximum local gain. From microwave perspective this DH laser diode represents a lossy, slow-wave microstrip transmission line, because of the high doping in the *p*- and *n*-type cladding layers and the high injected electron-hole pair density in the active region. It means that the conductivity depends on the bias level in the active layer. Considering the structure shown in Figure 2.1, a number of simplifications can be assumed for laser operation [20, 21, 22]:

1) Since the conductivity of the *n*-type cladding layer is much larger than that of the *p*-type cladding layer, the current spreading in the *n*-type layer can be neglected as well as the voltage drop in this layer.

2) The *p*-cladding layer behaves like a passive and homogeneous resistive region with a conductivity at a forward bias, where the interface space charge can be neglected [21, 22]. Thus, the potential distribution in the passive *p*-cladding layer is described by Laplace's equation:

$$\nabla^2 V = 0 \tag{2.23}$$

From the potential distribution, the current distribution can be expressed as

$$J = -\sigma_p \cdot \nabla V \tag{2.24}$$

The current density injected into the active layer, which is varying laterally, can be obtained by using the following expression:

$$J(x, y, z)\big|_{y=d} = -\sigma_p \cdot \nabla V(x, y, z)\big|_{y=d} \tag{2.25}$$

Where σ_p is the conductivity of the p-type cladding region and $V(x,y,z)$ is the potential distribution calculated from Eq. (2.23). This injected current density acts as the source of the carrier distribution, n, in the active layer. The total current injected into the active region from the electrode strip can be obtained from

$$I_{strip} = \int_{strip} J(x, y, z)\big|_{y=Yc} dxdz \tag{2.26}$$

3) Both the carrier quasi-Fermi levels and the carrier concentration across the heterojunction interface are continuous in the direction perpendicular to the junction, which leads naturally to the saturation of the diode voltage at the lasing threshold.

4) Charge neutrality condition can be assumed in the active layer due to very high carrier concentrations compared with the lightly-doped p and n regions:

$$n + N_A^- = p + N_D^+ \tag{2.27}$$

where n and p are the electron and hole densities, N_A^- and N_D^+ are the ionized acceptor and donor densities.

5) Along the device lateral direction the injected carrier distribution in the active region is described by the carrier continuity equation, which may be written as follows [20, 21]:

$$D_{eff}\nabla^2 n - Bn^2 - \frac{c}{n_0} g S_0 \Psi + \frac{J}{qt} = 0 \tag{2.28}$$

where the steady-state condition, $\partial n/\partial t = 0$, is assumed. D_{eff} is the effective diffusion constant, B the carrier recombination constant, g the gain profile across the active region,

q the electronic charge, t the active layer thickness, J the local injected current density, S_0 the average photon density in the optical cavity, and Ψ the normalized optical intensity which is defined as [14, 15, 22]:

$$\Psi(x, y) = \frac{|E(x, y)|^2}{\iint |E(x, y)|^2 \, dxdy} \tag{2.29}$$

Note that Eq. (2.28) assumes that the active layer thickness t is small compared to the carrier diffusion length. This means that no recombination occurs outside the active region.

Under these considerations, the potential difference across the active layer is related to the quasi-Fermi level separation, which dictates the carrier density, $n(x,z)$, at this point:

$$qV(x, y, z)\big|_{y=d} = F_c(x, z) - F_v(x, z) \qquad \text{(eV)} \tag{2.30}$$

The electron and hole densities in the active layer are known as, respectively,

$$n(x, z) = N_c F_{1/2}\left[\frac{F_c(x, z) - E_c(x, z)}{kT}\right] \tag{2.31}$$

$$p(x, z) = N_v F_{1/2}\left[\frac{F_v(x, z) - E_v(x, z)}{kT}\right] \tag{2.32}$$

$$E_c - E_v = E_g \tag{2.33}$$

$$F_c - F_v = q(\phi_h - \phi_e) \tag{2.34}$$

where k is the Boltzmann constant. F_c and F_v are the quasi-Fermi levels of electrons and holes, respectively. E_c and E_v are the conduction and valence band edges of the active region. N_c and N_v are the corresponding effective densities of states. E_g is the bandgap of the active layer material in *eV*. ϕ_h and ϕ_e are the electrostatic potentials on either side of the *p-n* heterojunction. $F_{1/2}$ is the Fermi-integral:

$$F_{1/2}(\theta) = \frac{2}{\sqrt{\pi}} \int_0^{\infty} \frac{\sqrt{\beta}}{1 + \exp(\beta - \theta)} d\beta \tag{2.35}$$

For the purpose of numerical analysis, an approximate solution of the Fermi integral was suggested by Joyce and Dixon [23]:

$$\phi_e = \left[\frac{F_c(x,z) - E_c(x,z)}{kT} \right]$$

$$= \ln\left[\frac{n}{N_c}\right] + K_1\left[\frac{n}{N_c}\right] + K_2\left[\frac{n}{N_c}\right]^2 + K_3\left[\frac{n}{N_c}\right]^3 + K_4\left[\frac{n}{N_c}\right]^4 + \cdots \tag{2.36}$$

According to the charge neutrality condition, a similar type of equation can be obtained for ϕ_h in terms of p, the hole density, and N_v:

$$\phi_h = \left[\frac{F_v(x,z) - E_v(x,z)}{kT} \right]$$

$$= \ln\left[\frac{p}{N_c}\right] + K_1\left[\frac{p}{N_c}\right] + K_2\left[\frac{p}{N_c}\right]^2 + K_3\left[\frac{p}{N_c}\right]^3 + K_4\left[\frac{p}{N_c}\right]^4 + \cdots \tag{2.37}$$

Where $K_1 = 3.53553 \times 10^{-1}$, $K_2 = -4.95009 \times 10^{-3}$, $K_3 = 1.48386 \times 10^{-4}$, $K_4 = -4.42563 \times 10^{-6}$. Consequently, the potential difference across the active layer at the point *(x, z)* can be written in the form:

$$V(x,z)\,|_{y=d} = \left[\phi_e(x,z) + \phi_h(x,z) + \frac{E_g}{kT} \right] \cdot \frac{kT}{q} \tag{2.38}$$

The local gain, *g(x,z)*, is related to the carrier concentration by the following relation [24]:

$$g(x,z) = a \cdot n(x,z) - b \tag{2.39}$$

where *a* and *b* are constants given in [21]. Eqs (2.23)~(2.39), together with the optical wave equation and the photon rate equation define the three-dimensional laser device model completely. It is obvious that all these equations are coupled. Hence, a self-consistent approach has to be applied. From the standpoint of solving the electrical behavior of the

laser model, the problem is to find an electrostatic potential distribution and the quasi-Fermi levels in the active layer that are consistent with the relationships defined above. This can be achieved by using the finite difference method. After the electron-hole pair concentration n is obtained the conductivity profile in the active region is readily found [13]:

$$\sigma_a = q(\mu_n + \mu_p)n \tag{2.40}$$

where μ_n and μ_p are the mobility of electrons and holes in the active layer, respectively.

The conductivity profile given in Eq. (2.40) can then be used to represent the active layer as a lateral inhomogeneous substrate layer. In the analysis of the laser diode as a lossy and slow-wave microwave transmission line structure, the knowledge of the conductivity profiles is then used as input parameter for the electromagnetic field simulation such as the frequency-domain TLM method (FDTLM). The FDTLM method is a rigorous full wave technique which can be used for 2D and 3D discontinuity problems. In the next chapter, the application of the FDTLM method in the analysis of wave propagation in microwave transmission lines with multi-layer semiconductor substrates and doped layers will be described,. A detailed discussion of the FDTLM algorithm has been given in reference [6, 7]. In this thesis, a new frequency-domain symmetrical condensed node (SCN) is being proposed in Chapter 3.

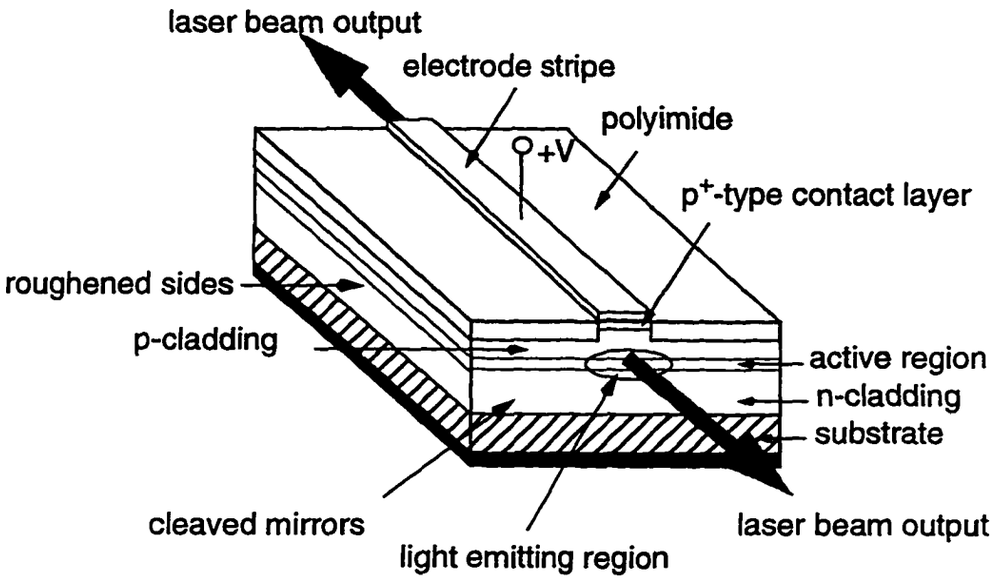

(a)

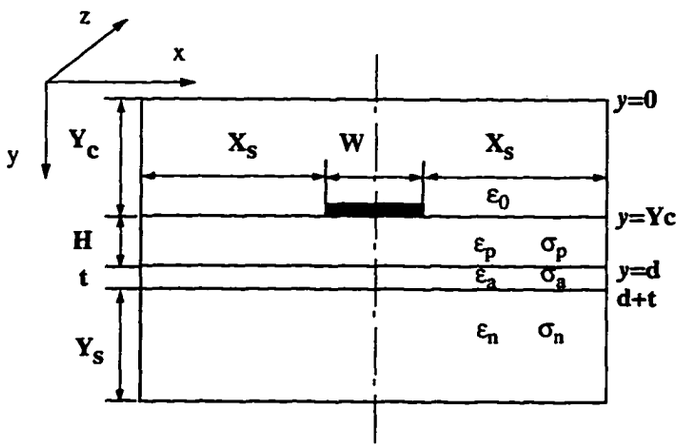

(b)

Figure 2.1 (a) Typical high speed semiconductor laser diode with double heterostructure (DH). (b) A three layer lossy and slow-wave microstrip transmission line model for semiconductor DH laser.

2.3 Numerical Solution for Current Spreading and Carrier Diffusion in DH Laser with Strip Discontinuities

The model used in the numerical analysis is shown in Figure 2.2, together with the boundary conditions used. In this figure, $\hat{x}$, $\hat{y}$ and $\hat{z}$ are the unit vectors in the x-, y- and z-directions, respectively. The heterojunction under consideration is at $y=d$ and the thickness of the active layer is t. A self-consistent numerical solution technique is based on the device being modeled by Laplace's equation and the carrier diffusion equation. The self-consistent scheme solves these equations simultaneously using the finite difference scheme.

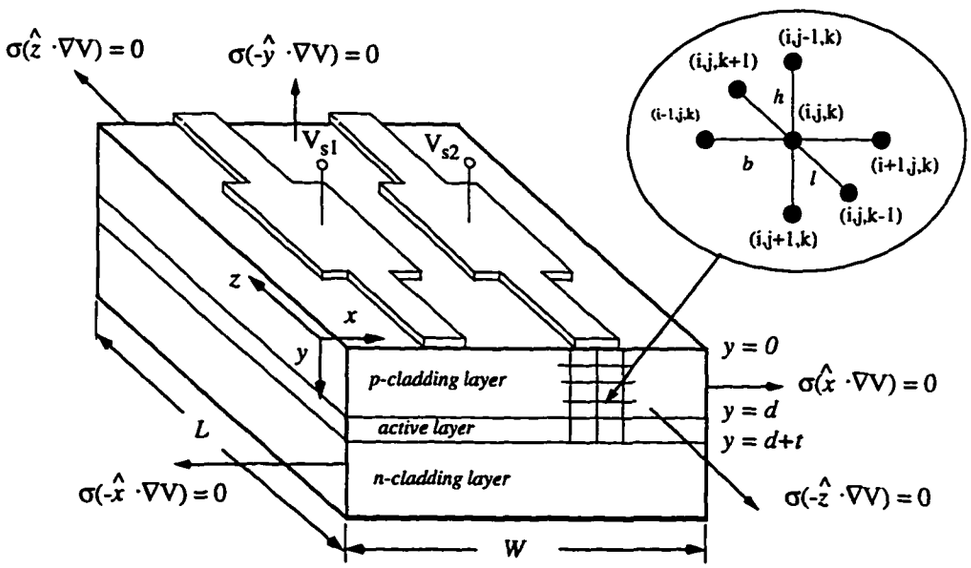

Figure 2.2 The 3D double-stripe DH laser model with discontinuity for the numerical computation of injection current intensity and carrier density in the active layer.

2.3.1 The Self-Consistent Solution Scheme

The finite difference (FD) method is used to solve Eqs. (2.23)-(2.25) consistently. These equations constitute a physical model of the 3D DH laser. The solution process can be described by the following two main steps.

1) The p-type resistive cladding layer: The resistive *p*-type cladding layer is discretized into a cuboid mesh in terms of the step length $\{b,h,l\}$ in the *x*-, *y*- and *z*-directions. At each internal node of the mesh the three-dimensional Laplace's equation

$$\left(\frac{\partial^2}{\partial x^2} + \frac{\partial^2}{\partial y^2} + \frac{\partial^2}{\partial z^2}\right) V(x,y,z) = 0 \tag{2.41}$$

can be written in finite difference form

$$\frac{V(i-1,j,k) + V(i+1,j,k) - 2\cdot V(i,j,k)}{b^2} + \frac{V(i,j-1,k) + V(i,j+1,k) - 2\cdot V(i,j,k)}{h^2} + \frac{V(i,j,k-1) + V(i,j,k+1) - 2\cdot V(i,j,k)}{l^2} = 0 \tag{2.42}$$

From the device model in Figure 2.2, it follows that the Neumann boundary condition for the static-state potential, *V*, can be applied at the boundary nodes since the components of the current have vanished. At the interface between the passive resistive layer and the active layer, the quasi-Fermi potential boundary condition, Eqs. (2.30)~(2.38), is enforced.

In this case, Eq. (2.41) reduces to a set of linear algebraic equations at the nodes in the *p*-type resistive cladding layer, which can be solved using a successive over-relaxation technique (SOR). Initially, an estimate of the potential distribution along the heterojunction is made, such as, $V(i, j, k)=1$. Laplace's equation is solved using SOR. $J(x,y,z)|_{y=d}$ is then solved numerically using the appropriate difference form, and the calculated values of $J(x,y,z)|_{y=d}$ are used in the second step to determine the injection carrier concentration.

2) The active layer: The diffusion equation is also solved using the finite difference method. The distribution of the nodes along the heterojunction, at $y = d$ in the previous step, becomes the desired discretization in solving the diffusion equation. The carrier concentration is generally a large quantity and causes numerical instability because of truncation errors and "exponential overload". To minimize this problem the carrier density is normalized by the intrinsic carrier density, n_i. The normalized finite difference form of the carrier diffusion equation can be written as

$$D_{eff}\left[\frac{n(i+1,k)/n_i + n(i-1,k)/n_i - 2\cdot n(i,k)/n_i}{b^2}\right]$$

$$+ D_{eff}\left[\frac{n(i,k+1)/n_i + n(i,k-1)/n_i - 2\cdot n(i,k)/n_i}{l^2}\right]$$

$$- Bn_i \cdot \left[\frac{n(i,k)}{n_i^2}\right] - \frac{c}{n_0 n_i} g(i,k) S_0 \Psi(i,j,k) + \frac{J(i,j,k)\big|_{y=d}}{qtn_i} = 0 \qquad (2.43)$$

This equation is valid at all the nodes along the heterojunction except at the end of the nodes, where approximations must be made to reduce the size of the problem. After that, a set of nonlinear algebraic equations is obtained which can be solved by the Newton-Raphson over-relaxation method. In the iterative scheme the iterations are stopped when the global error of the potential distribution is less than an acceptable value.

2.3.2 Boundary Conditions at the End of the Nodes

In the active layer the boundary conditions for the carrier density at the device both ends of the nodes exist at $x=0$, $x=W$, $z=0$, and $z=L$. The following alternative boundary conditions can be considered:

1) *Neumann boundary*: Carrier density is nonzero, and the derivative of the carrier density can be set to zero at the boundary of the active layer, *i. e.*

$$n(0,0) \neq 0, \qquad n(W,z) \neq 0, \qquad n(x,L) \neq 0$$

and

$$\left.\frac{dn}{dx}\right|_{x=0} = \left.\frac{dn}{dx}\right|_{x=W} = \left.\frac{dn}{dz}\right|_{z=0} = \left.\frac{dn}{dz}\right|_{z=L} = 0 \tag{2.44}$$

These are known as Neumann boundary conditions for the carrier density in the active layer. Eq. (2.44) can be expressed approximately in an appropriate finite difference form. It can be seen that this is a reasonable approximation because the quasi-Fermi levels for both electrons and holes approach the intrinsic Fermi level near the boundary edges, therefore becoming equal to each other.

2) *Decay boundary*: An alternative to the boundary condition at $x=W$ can be obtained in terms of an analytic extrapolation of $n(x,z)$ from $x=W$ to $x \to \infty$. It is reasonable to assume that the injected current density is approximately zero at the boundary edge in lateral direction. Therefore, the two set of boundary conditions are assumed as follows:

$$n(x,z)\big|_{x=-\infty} = n(x,z)\big|_{x=\infty} = 0 \tag{2.45}$$

and

$$\left.\frac{dn(x,z)}{dx}\right|_{x=-\infty} = \left.\frac{dn(x,z)}{dx}\right|_{x=\infty} = 0 \tag{2.46}$$

According to the condition of the injected current density at the boundary edge, the carrier continuity equation Eq. (2.28) for the regions of $-\infty < x < 0$ and $W < x < \infty$ can be written as

$$\frac{d^2 n(x,z)}{dx^2} = \frac{B}{D_{eff}} n^2(x,z) \tag{2.47}$$

where the photon generation term can be neglected. For the region $-\infty < x < 0$, solving Eq. (2.47) in the integral form and applying the boundary conditions in Eq. (2.45) and Eq. (2.46) yields

$$\frac{dn(0,z)}{dx} = -\left[\frac{2B}{3D_{eff}}\right]^{1/2} n^{3/2}(0,z) \tag{2.48}$$

A similar solution can be obtained for the region $W < x < \infty$

$$\frac{dn(W,z)}{dx} = -\left[\frac{2B}{3D_{eff}}\right]^{1/2} n^{3/2}(W,z) \tag{2.49}$$

In the z-direction, the Neumann boundary condition for the carrier density can be still enforced at the both boundary edges.

2.3.3 Single-Strip Laser with Strip Discontinuity

The accuracy of the finite difference technique is dependent on the size of the mesh. Since the injected current density below the electrode strip and the strip discontinuity changes rapidly, the discretization mesh must be fine enough to account for these changes accurately. Therefore, before the final analysis could begin, test problems were simulated to check the mesh size with respect to conversion error. It was found that the mesh size shown in Table 2.1. provided a satisfactory accuracy (the static-state potential error for of two iterations is lees than 10^{-5}) for the problems investigated. The various device parameters used in the simulation of the single- and double-strip lasers with strip discontinuity are also given in Table 2.1. The numerical results from the self-consistent scheme were obtained under different bias conditions and for two different electrode discontinuities.

Figure 2.3 and Figure 2.4 illustrate the injected current spreading and carrier density distribution along the active region of a single-strip laser with a symmetrical and asymmetrical discontinuity in the electrode. The direction of the injected current density is perpendicular to the active layer. The voltage applied to the stripe is 1.58V. The numerical analysis shows clearly that below the wider part of the electrode the carrier concentration is significantly higher than before and after this region. Depending on the injected current density, this will correspond to a higher local gain region in the active layer. Figure 2.3 (b) and Figure 2.4 (b) also show a noticeable dip in the current density distribution in the center of the wider stripe region (width > 6μm), which is not observed in the narrower stripe section (width = 4μm). This is due to the nonlinear boundary condition introduced by the heterojunction and the resistivity in the cladding layer. These current density profiles confirm the 2D analytical prediction of Kumer *et al* [20]. Furthermore, it should

be noted that these dip sections in the current density distribution are not accompanied by a corresponding dip in the carrier concentration distribution. The carrier concentration distribution is shown in Figure 2.3 (c) and Figure 2.4 (c). These figures show that the inclusion of the diffusion equation into the self-consistent scheme is very important to determine the current and carrier density distribution accurately. Since the local gain is proportional to the carrier density, the discontinuities in the longitudinal direction influences the local gain profile. This effect is important in laser array application to suppress undesired lateral modes

Table 2.1. Device Parameters

Parameter	Value	Unit
p-cladding thickness, d	2.0	μm
conductivity, σ	0.2	Ωcm
x-direction mesh size, b	0.5	μm
y-direction mesh size, h	0.05	μm
z-direction mesh size, l	2.0	μm
active layer thickness, t	0.1	μm
diffusion coefficient, D_{eff}	40	cm^2/s
recombination coefficient, B	$9.7x10^{-11}$	cm^3/s
CB density of states, N_c	$4.7x10^{17}$	cm^{-3}
VB density of states, N_v	$7.0x10^{18}$	cm^{-3}
bandgap E_g	1.43	eV

To exploit the nonuniform biasing for near-field laser beam steering, a double-stripe laser with stripe discontinuities was investigated. In this case, asymmetrical biasing is considered. Figure 2.5 shows the current and carrier density distribution for $V_{s1}=1.56V$ and $V_{s2}=1.58V$. In this case the carriers begin to be injected into the active layer and the carrier concentration exceeds $2.6x10^{18}cm^{-3}$ below the electrode region. In the active layer the carrier density is high enough for achieving lasing oscillation. From Figure 2.5 we find that for the lightly-doped *n*-type GaAs active layer the space charge is mainly determined by

the spreading of the injected current. The spreading in here is dependent on the shape of the discontinuity of both electrode strips. The current density profile below the discontinuities is therefore strongly affected by the current spreading in the *p*-type GaAlAs confining layer and the lateral diffusion of carriers in the active layer. At the same time the levels of injected current and the effective diffusion coefficient determine the lateral diffusion of carriers in the active layer. For the carrier concentration the effect of diffusion is extremely important when the stripe spacing is less than the carrier diffusion length. For the dimensions of the electrode strips chosen in this work, therefore, diffusion has a significant effect on the carrier concentration in the unpumped region between the stripes. Figure 2.5 shows the effect of electrode spacing on the current density and carrier density distributions, respectively. The stripes are closest in the region where the stripe discontinuity occurs. It is evident that with increased spacing between the electrode stripes, the local gain in the unpumped region will decrease relative to the carrier concentration distribution. Conversely, an increasing electrode width will cause a small increase in the peak value of the carrier concentration, which is also the case in the single-strip laser. It is clear from the 3D numerical simulation that the strong effects of carrier diffusion and current spreading in the discontinuities region are caused by the bias current bond wire contact. The effect of which must thus be taken into account if multiple stripe laser are used in applications where optical beam steering is required.

In this section, a self-consistent three-dimensional numerical modeling of semiconductor single- and double-stripe DH laser with electrode discontinuities along the longitudinal direction of the device has been introduced. Lateral current and carrier density distributions along the active layer have been calculated for different biasing conditions. It has been shown that different strip geometry and sudden steps in the stripe dimensions together with varying bias conditions have a direct effect on the local gain profile of the structure. This phenomenon must be attributed to beam steering of laser arrays made from these structures. The work presented is a first step towards a full-wave analysis of beam pattern analysis in laser array applications as well as in the accurate analysis and design of laser diodes.

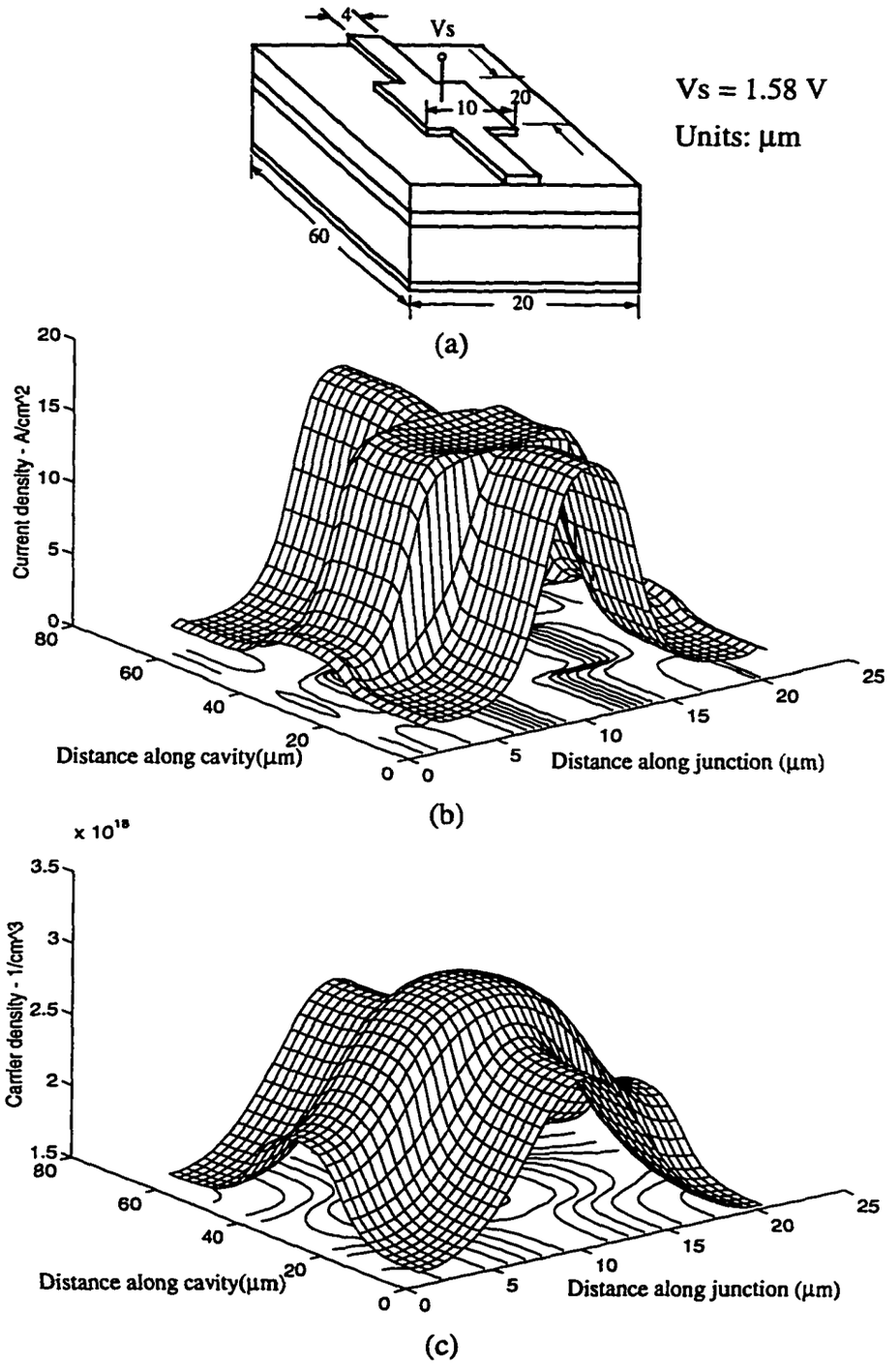

Figure 2.3 (a) Single-stripe DH laser with symmetrical discontinuity stripe. (b)The injected current density and (c) the carrier concentration distribution in the active layer with bias voltage V_s=1.58V.

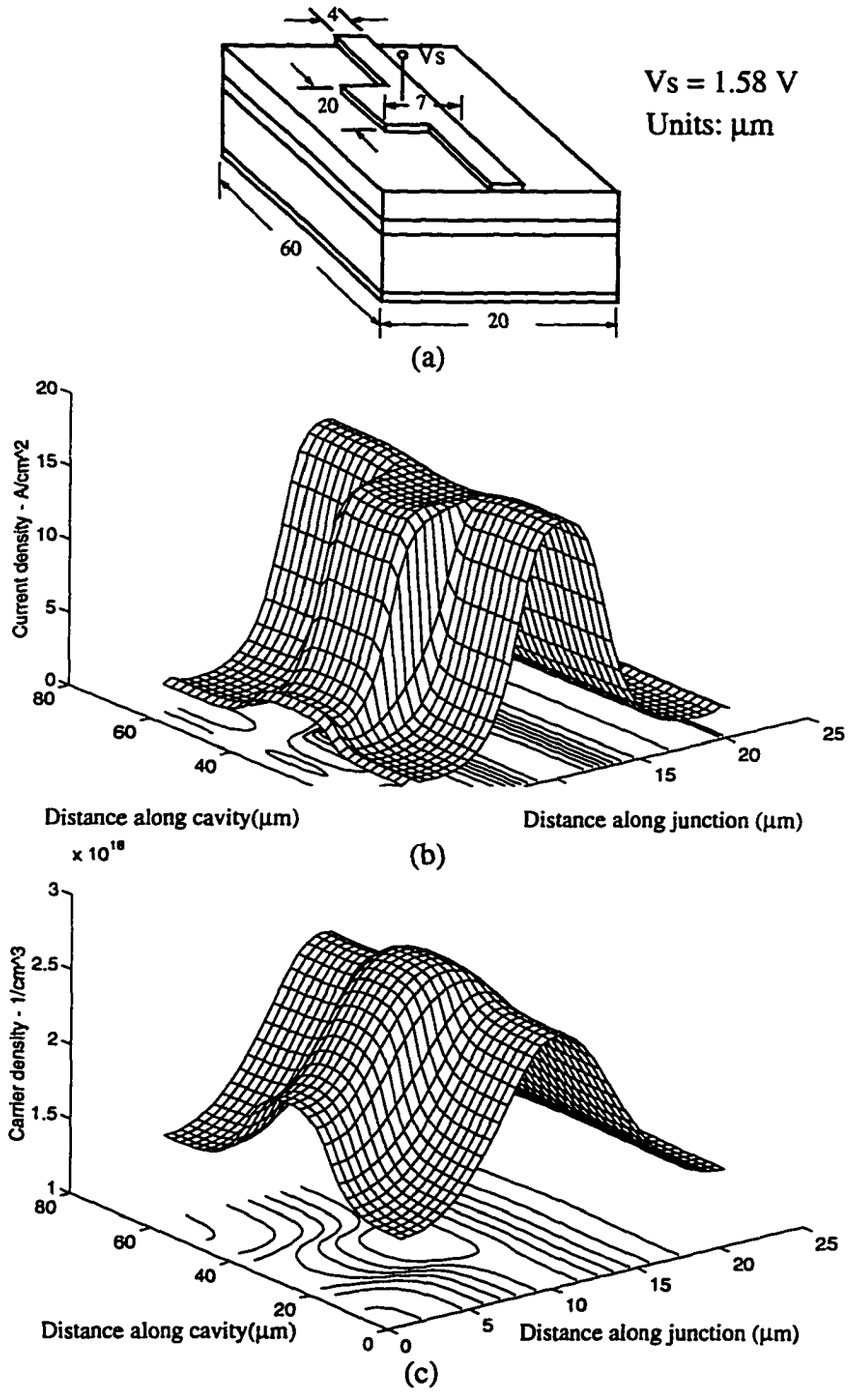

Figure 2.4 (a) Single-stripe DH laser with asymmetrical discontinuity stripe. (b)The injected current density and (c) the carrier concentration distribution in the active layer with bias voltage V_S=1.58V.

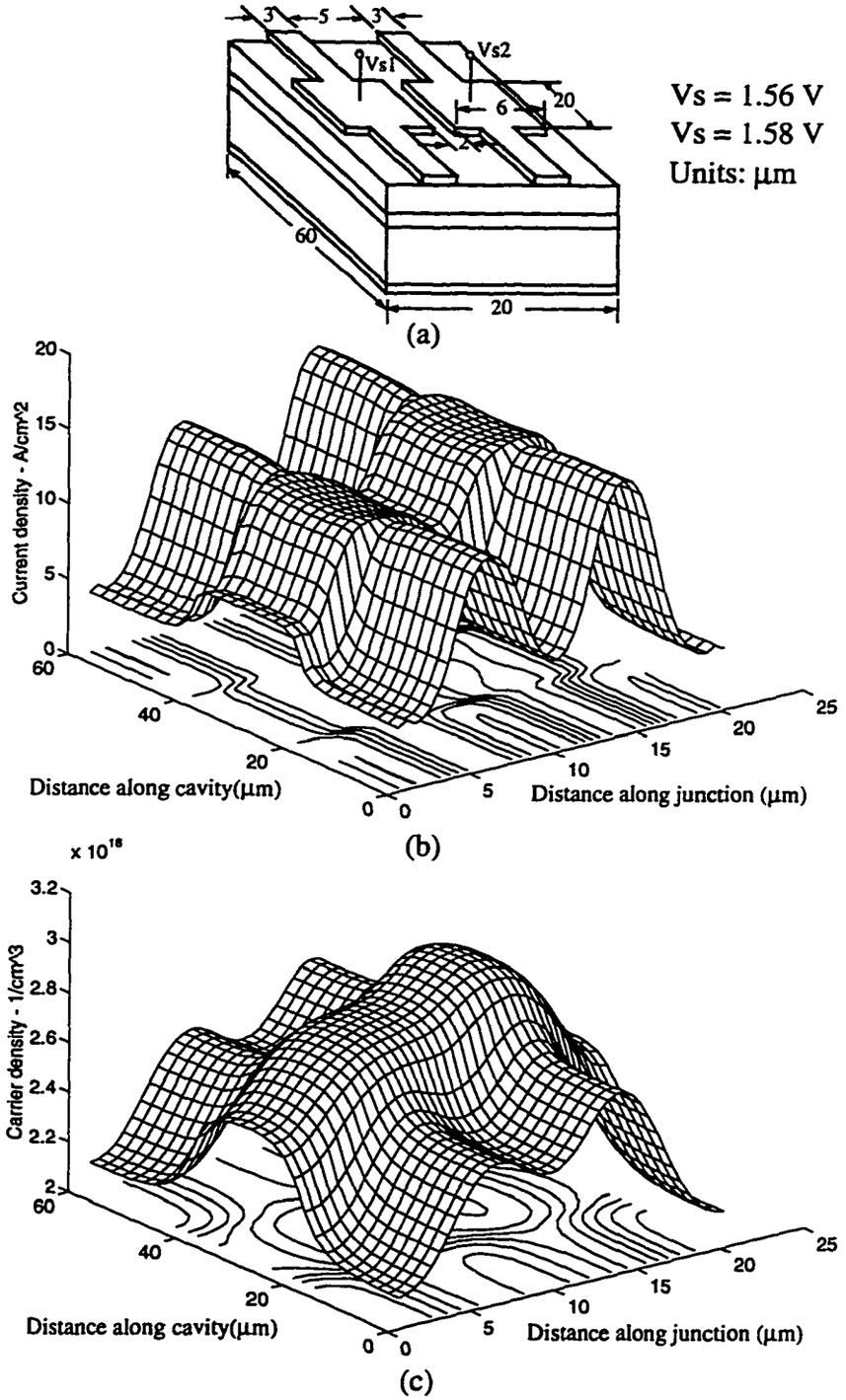

Figure 2.5 (a) Double-stripe DH laser with symmetrical discontinuity stripe. (b)The injected current density and (c) the carrier concentration distribution in the active layer with bias voltage V_{s1}=1.58V, V_{s1}=1.56.

2.4 Analysis of Active Optical Waveguides

With the progress in semiconductor technology, semiconductor dielectric waveguides are becoming increasingly important in the field of optoelectronic design. This has led to an increased interest in the theoretical analysis of the dielectric waveguide configurations, such as slab, strip-loaded, embossed, rib and ridge structures. The semiconductor laser diode, as well as optical amplifiers and optical modulators, which are typically formed by semiconductor slab or ridge waveguiding configurations, contain an active layer in which the local refractive index is complex depending on the bias. The important feature here is that the imaginary part of the refractive index. The positive sign of the imaginary part represents optical gain and the negative sign represents optical loss. In gain-guided lasers, the refractive index is a function of the bias current. In order to take the full function of this active layer into account, accurate knowledge of the waveguide mode propagation and associated field profiles are essential.

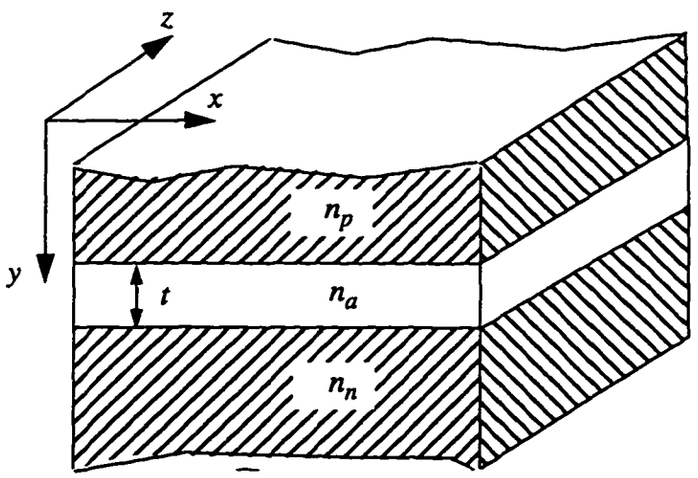

Figure 2.6 Sketch of a typical semiconductor slab waveguide and the coordinate system.

Electromagnetic wave propagation in semiconductor waveguides is governed by the Helmholtz vector wave equation with appropriate boundary conditions. An optical

waveguide supports the propagation of waves which have two possible field configurations. These waves are classified as the TE and TM waves (or modes) [25, 26]. We consider the semiconductor slab waveguide structure and coordinate system shown in Figure 2.6 where a dielectric layer with thickness t and refractive index n_a is sandwiched between two cladding layers of refractive indices n_p and n_n.The transverse field components of the TE mode are the electric field, E_x, and the magnetic field, H_y, while transverse field components of the TM mode are E_y and H_x. From [19] it is know that TE modes are dominant in semiconductor lasers. Therefore, only the Helmholtz wave equation for the electric field component, E_x, is solved [26~28], which refers to the horizontal polarizations.

2.4.1 An Extended Complex Finite Difference Method (ECFD)

For time-harmonic wave propagation in the longitudinal (z) direction of a semiconductor active optical waveguide (the semiconductor laser and optical amplifiers with injection modulation essential) shown in Figure 2.6, TE mode is assumed [19] and the electric field component is [26, 29, 30] expressed as follow:

$$E_x(x, y, z) = E_x(x, y)\, exp\,[j(\omega t - \beta z)] \tag{2.50}$$

where β is the propagation constant and $E_x(x, y)$ is the optical field distribution. The field distribution $E_x(x, y)$ and propagation constant β can be determined from a solution of the Helmholtz wave equation [27~31]:

$$\nabla_T^2 E_x + (k^2{}_0 n^2(x, y) - \beta^2) E_x = 0 \tag{2.51}$$

where ∇_T^2 is the transverse operator, $\left(\partial^2/\partial x^2 + \partial^2/\partial y^2 \right)$, β is the phase constant, $n(x,y)$ is the local refractive index, $\varepsilon(x,y)=n^2(x,y)$, which exhibits a complex profile in the active region, and $k_0=2\pi/\lambda_0$ with λ_0 the free space wavelength. In the implementation of the complex finite difference method, we consider that E_x, $\partial E_x/\partial x$ and $\partial E_x/\partial y$ are continuous throughout the solution domain. Usually, wave equation Eq.(2.51) can be written in a five-point finite difference form to produce an expression for the electric field at each mesh point in terms of its four nearest neighbors. Each mesh point lies at the center

of a cell of constant refractive index, and changes in refractive index occur only at the cell boundaries. Eq. (2.51) can be converted into the algebraic eigenvalue problem [31]

$$A_m E_m = \beta_m^2 E_m \tag{2.52}$$

where A_m is a symmetric band matrix, β_m^2 is the scalar mode propagation eigenvalue, and E_m is the corresponding normalized eigenvector representing the field profile $E_x(x, y)$.

The finite difference method is used to solve the scalar wave equation Eq.(2.51). In this approach the field values $E_x(x, y)$ and the phase constant β are found from the Rayleigh variational principle. From that principle the eigenvalue equation can be presented in variational form as [28, 29]:

$$\beta^2 = \frac{\iint [E\nabla_T^2 E + k_0^2 n^2(x, y) E^2] \, dxdy}{\iint E^2 dxdy} \tag{2.53}$$

To determine β, Eq. (2.51) and Eq. (2.53) are applied alternately until the solutions of the field values at the mesh point and the phase constant converge. Whether the semiconductor optical waveguide structure provides optical gain or loss depends on the complex refractive index values across the waveguide. Therefore, in the calculation to Eq. (2.51) and Eq. (2.53), complex refractive indices are used directly, producing a complex phase constant, $\beta=\beta_m+j\alpha_m$, and complex electric field values, $E_x(x, y)$, where the phasor term, $e^{-j\beta \cdot z}$, for the Eq. (2.50) can be written as

$$e^{-j\beta \cdot z} = e^{-j(j\alpha_m + \beta_m) \cdot z} = e^{\alpha_m \cdot z} \cdot e^{-j\beta_m \cdot z} \tag{2.54}$$

The real part β_m represents the propagation constant of the propagating mode, and the imaginary part α_m is either the optical gain if α_m is positive, or the optical loss (electric field attenuation) if α_m is negative for the wave propagating in +z direction.

By using the ECFD discretization scheme, the electric field is taken as a matrix of discrete values throughout a box large enough to contain the waveguide and the adjacent regions where the field strength is significant. Figure 2.7 gives the finite difference mesh

diagram. The scalar Helmholtz wave equation and the phase constant, β, become a difference equation with the partial derivatives approximated by the differences between adjacent field points, which are expressed as

$$\frac{E_x(i-1,j)+E_x(i+1,j)-2E_x(i,j)}{b^2}+\frac{E_x(i,j-1)+E_x(i,j+1)-2E_x(i,j)}{h^2}$$

$$+\left[k_0^2 n^2(i,j)-\beta^2\right]E_x(i,j)=0 \tag{2.55}$$

and

$$\beta^2=\frac{A}{b^2\sum_{i,j}E_x^2(i,j)} \tag{2.56}$$

where

$$A=\sum_{i,h}E_x(i,j)\left\{\left[E_x(i-1,j)+E_x(i+1,j)\right]\right.$$

$$\left.+\frac{b^2}{h^2}\left[E_x(i,j-1)+E_x(i,j+1)\right]+\left[b^2k_0^2n^2-q_1\right]E_x(i,j)\right\} \tag{2.57}$$

where

$$q_1=2\left(1+\frac{b^2}{h^2}\right) \tag{2.58}$$

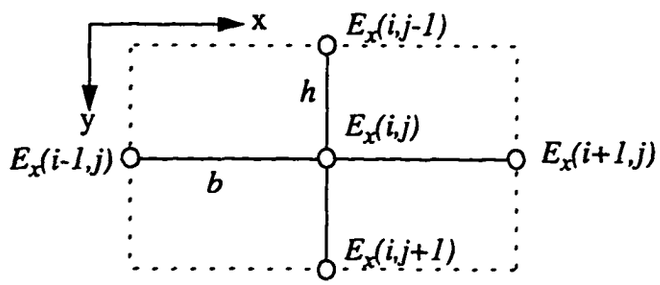

Figure 2.7 The mesh for the finite difference approach.

In the over-relaxation process, the electric field components can be written as:

$$E_x^{k+1}(i,j) =$$

$$E_x^k(i,j) + R\left[\frac{1}{\left[2\left(h^2+b^2\right)-h^2b^2\left(k_0^2n^2(i,j)-\beta^2\right)\right]}\{h^2\left[E_x^k(i-1,j)+\right.\right.$$

$$\left.\left.E_x^k(i+1,j)\right]+b^2\left[E_x^k(i,j-1)+E_x^k(i,j+1)\right]\}-E_x^k(i,j)\right] \qquad (2.59)$$

In this ECFD approach an initial guess is made for the complex phase constant, β, and for the electric field value at each mesh point within the box. Eqs. (2.55)~(2.59) are applied alternately until the solution for the mesh point electric field values and eigenvalue, β, converge to a given criterion for the sufficient accuracy. In order to improve the ECFD approach, the relaxation parameter, *R*, is selected between 1 and 2, such as the values of *R* near 1.5. This leads to a better rate of convergence and thus a computationally more efficient algorithm.

2.4.2 Testing the ECFD Method

The accuracy of the ECFD method can be validated by applying it to the slab waveguide shown in Figure 2.8. An exact solution of Maxwell's equations can be found analytically from the governing transcendental equation:

$$\tan(\kappa h) = \kappa(\Upsilon+\delta)/\left(\kappa^2-\Upsilon\delta\right) \qquad (2.60)$$

where:

$$\kappa = \sqrt{n_1^2k_0^2-\beta^2}\,, \quad \Upsilon = \sqrt{\beta^2-n_2^2k_0^2}\,, \quad \delta = \sqrt{\beta^2-n_3^2k_0^2}$$

Table 2.2. presents the real and imaginary parts of the modal index ($n_{mode}=\beta/k_0$) computed using the ECFD method as a function of the mesh size. The operating wavelength is λ_0=1.5μm. The exact solution is $n_{mode}=3.2858937+j7.825\text{x}10^{-4}$. The results from the ECFD method compares well with the analytical result for a sufficiently fine mesh size.

Table 2.2. The modal index n_{mode} using ECFD method

Mesh Size (μm)	Δx/λ	Real n_{mode} [28]	Error* (%)	Real n_{mode}	Error* (%)	Imag n_{mode} [28] ($x10^{-4}$)	Error* (%)	Imag n_{mode} ($x10^{-4}$)	Error* (%)
0.01	0.0067	3.2859	0.0009	3.2858	0.0003	7.826	0.0127	7.825	0.005
0.05	0.075	3.2864	0.014	3.2864	0.014	7.863	0.485	7.863	0.485
0.1	0.067	3.2879	0.060	3.2878	0.059	7.973	1.892	7.970	1.853

* Error is compared with the analytic solution.

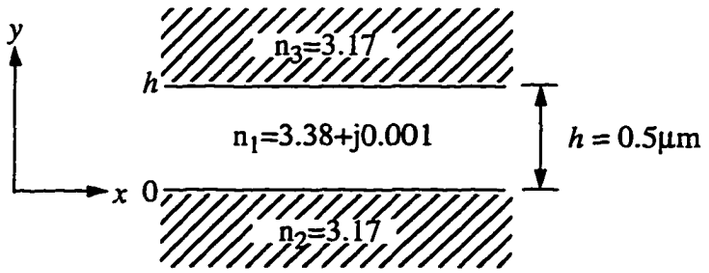

Figure 2.8 The semiconductor slab optical waveguide.

2.4.3 Application to Multilayer Semiconductor Active Optical Waveguides

To further demonstrate the accuracy and flexibility of the algorithm semiconductor gain-guided laser with a slab waveguide structure is analyzed. For the fundamental mode the 2D electric field profile is shown in Figure 2.9 for single-strip slab waveguide and in Figure 2.10 for twin-strip slab waveguide, respectively, where W = 3 μm, H = 1 μm and G= 3 μm (for twin-strip). For the optical wave propagation, the structures are considered as three layer slab waveguide. The refractive indices are n_0=1, n_p=n_n=3.40 at an operating wavelength of 1.50 μm. The refractive index in the active region is a function of the

injected current. For the area far from the electrode strip, the influence of the injected current is minimum. Thus, the refractive index in this area is normally a real value of n_a=3.44. Inside the electrode area the injected current flows and n_a is complex. The value of the real and imaginary parts change in lateral direction. The mesh sizes used to discretize the structure are 0.05 and 0.2 μm in the x- and y-directions, respectively. A total of 10500 mesh cells is used. Figure 2.11 clearly shows that under biased condition the electric field is concentrated in the active waveguiding region under the strip. For an asymmetrically pumped twin-strip laser (two different biasing voltages applied), the gain-guiding region will shift towards the strip with the larger biasing voltage. This is shown in Figure 2.12 and illustrates the beam steering capability of this semiconductor laser structure.

The algorithm developed in this section provides the complex phase constant and electric field profile, $E_x(x, y)$, for the fundamental and first order modes. Both are functions of the injected current into the active layer. With a biasing voltage Vs=1.6V, the single-strip laser structure in Figure 2.9 has a normalized complex phase constant of $(\beta/k_0)=3.40255+j3.61193\times10^{-4}$, and the laser structure in Figure 2.10 $(\beta/k_0)=3.40452+j9.42884\times10^{-4}$ (the biasing voltages are Vs1=1.65V and Vs2=1.6V). As seen in Eq. (2.54), the real part of (β/k_0) represents the propagation constant. The positive imaginary part indicates optical gain for the wave propagating in the semiconductor medium. A negative imaginary part indicates loss and occurs only outside the gain medium region or below the threshold voltage. Comparing the two structures, the twin-strip laser requires larger bias and shows a higher imaginary (β/k_0) value than that of the single-strip laser. Therefore, higher optical gain occurs in the twin-strip laser.

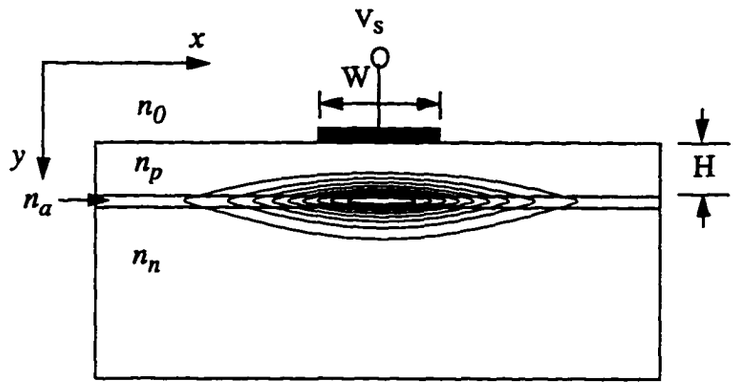

Figure 2.9 Two-dimensional electric field profile, E_x, for the fundamental mode within the single-strip semiconductor laser diode with V_{s1}=1.6 V. Contour levels are at 10% intervals of the maximum field.

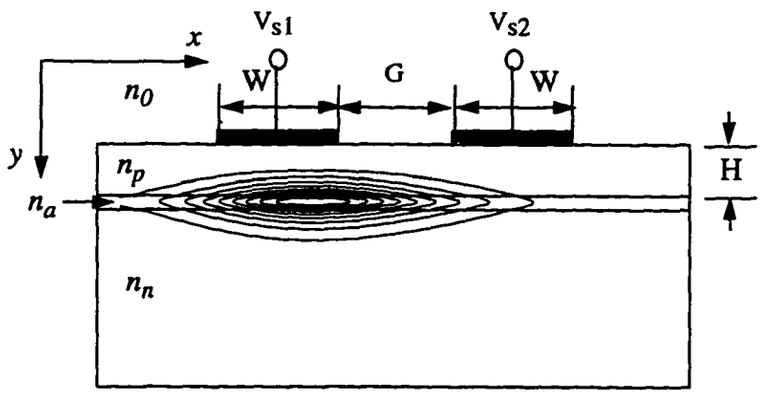

Figure 2.10 Two-dimensional electric field profile E_x, for the fundamental mode within the twin-strip semiconductor laser diode with V_{s1}=1.65V, V_{s2}=1.6V. The effect of beam steering is clearly visible. Contour levels are at 10% intervals of the maximum field.

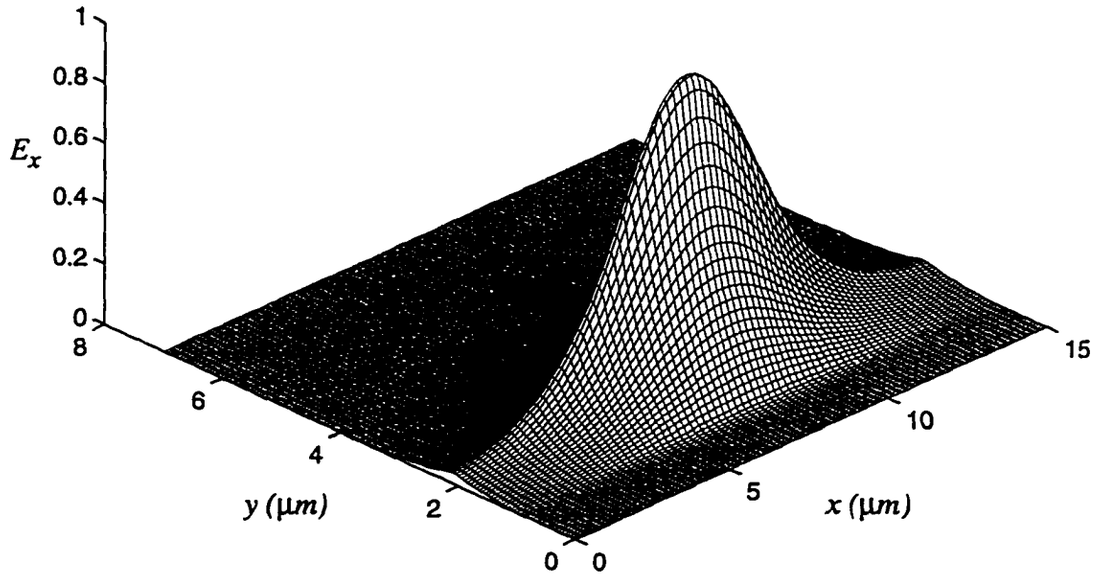

Figure 2.11 Fundamental mode electrical field distribution, E_x, within single-strip slab waveguide semiconductor laser with V_{s1}=1.60V (λ=1.5μm).

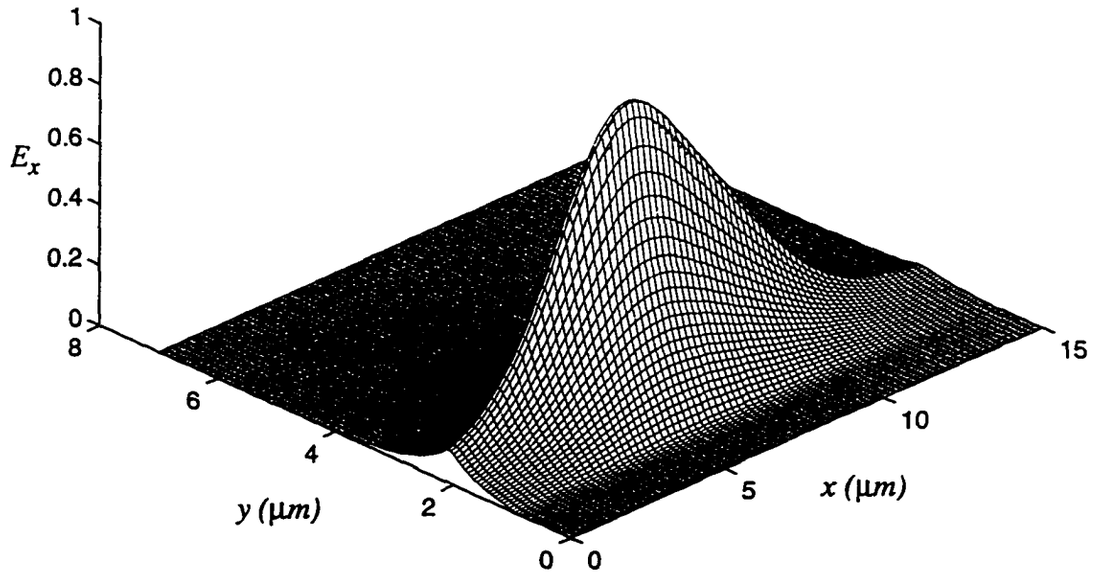

Figure 2.12 Fundamental mode electrical field distribution, E_x, within the twin-strip slab waveguide semiconductor laser with V_{s1}=1.65V, V_{s2}=1.6V (λ=1.5μm).

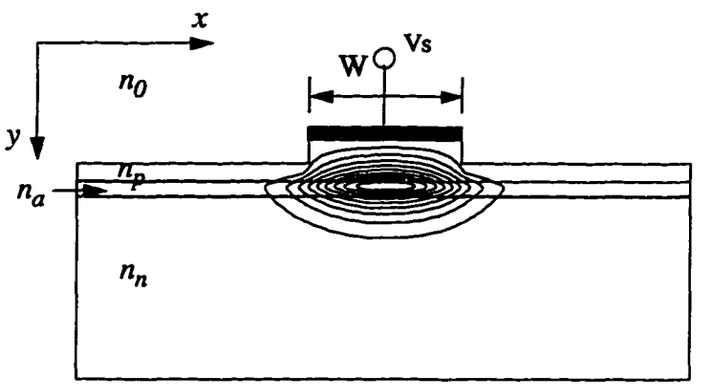

Figure 2.13 (a) Two-dimensional electric field profile for the fundamental mode within a ridge waveguide semiconductor laser. Contour levels are at 10% intervals of the maximum field amplitude.

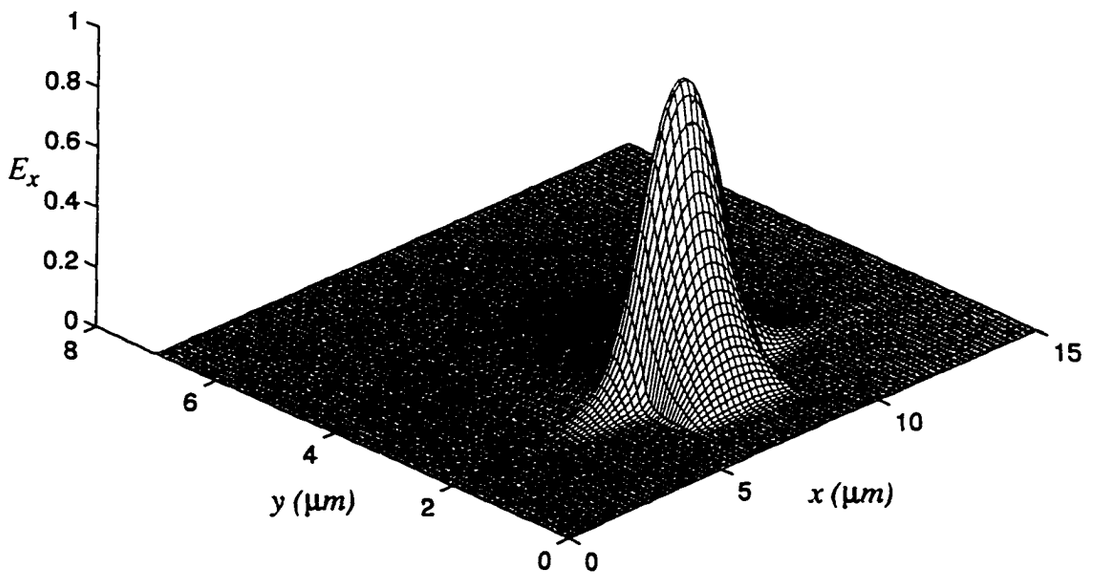

Figure 2.13 (b)The fundamental mode electric field distribution, E_x, within the ridge waveguide structure semiconductor laser. (λ=1.50μm)

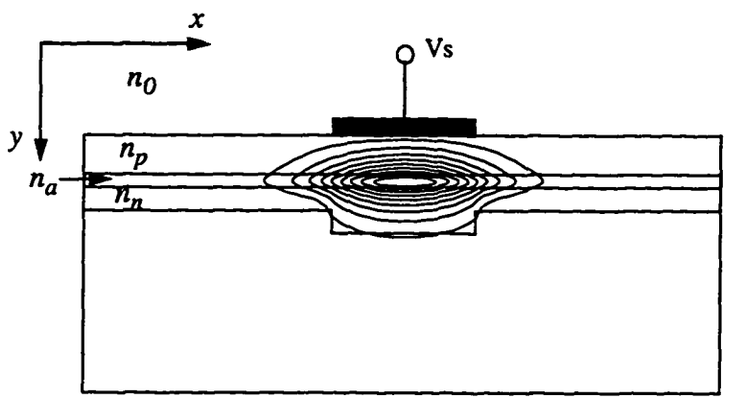

Figure 2.14 (a) Two-dimensional electric field profile for the fundamental mode within the rib waveguide semiconductor laser. Contour levels are at 10% i

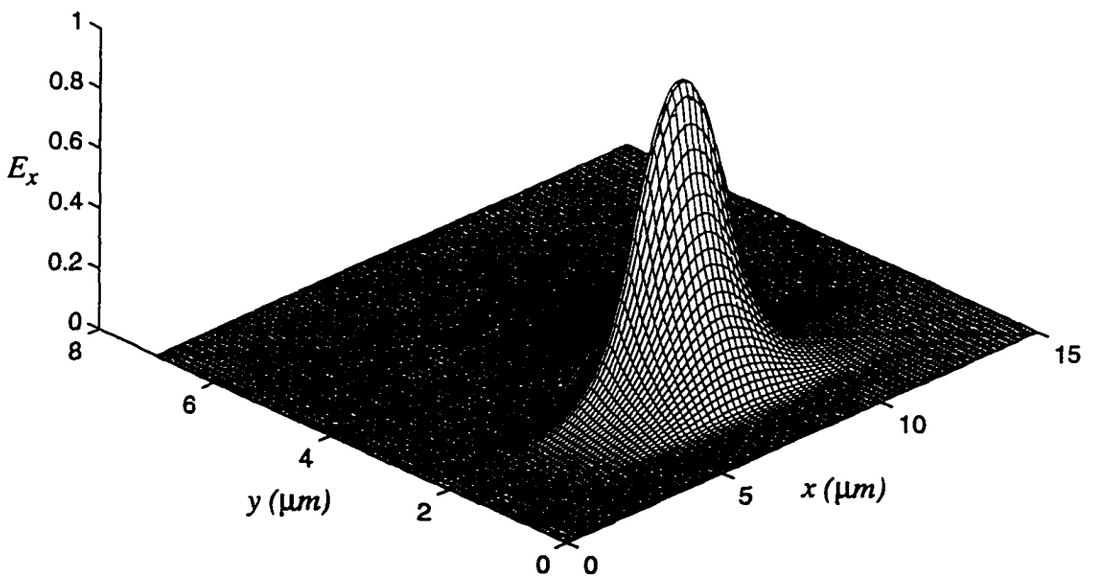

Figure 2.14 (b) The fundamental mode electric field distribution, E_x, within the back-rib waveguide structure semiconductor laser. (λ=1.50μm)

Semiconductor lasers with dielectric ridge and rib waveguide structures can also be analyzed with the algorithm developed here. First, we consider the ridge waveguide lasers. The 2D field profile of the fundamental scalar mode is shown in Figure 2.13 for the operating wavelength 1.50μm, where $n_p = n_n = 3.17$ and $n_a = 3.34$. At the biasing voltage of Vs=1.60V, we have $(\beta/k_0)=3.1952+j9.5242\times10^{-4}$. The 2D field profile of the rib waveguide laser is shown in Figure 2.14 for the fundamental TE mode operating at 1.50μm, where $n_p = n_n = 3.17$ and $n_a = 3.34$. At a biasing voltage of Vs=1.60V, we have $(\beta/k_0)=3.1967+j1.0538\times10^{-3}$. It is obvious that for these two index-guiding configurations the optical field is more confined in the wave guiding region compared to the gain-guided laser. At the same time, they have also higher values of the imaginary part of (β/k_0) compared to the gain-guided laser, which means the optical gain is higher.

2.5 Discussion and Conclusion

In this chapter a self-consistent algorithm for the finite difference method and the extended complex finite difference (ECFD) method have been introduced for modeling semiconductor lasers and active waveguide devices. The semiconductor device equations (Poisson's equation, carrier continuity equations), Helmholtz wave equation and the rate equation are solved self-consistently. The algorithm is then applied to analyze lasers with uniform and non-uniform strip geometry. The approach for calculating the current spreading and carrier density distribution in the active layer is based on simplifying assumptions. However, it should be stressed that these assumptions are not fundamental limitations of the physical model, but rather good approximations. Based on the these assumptions it has been shown that different strip geometry and sudden steps in the strip dimensions with varying bias conditions have a direct effect on the local gain profile of the structures. In other words, electrode strip discontinuities can significantly change the complex refractive index in the active layer when the injected current and carrier density change. In turn, it may change the fundamental lasing mode profile. This phenomenon can also be used in beam steering of laser arrays made from these structures. The approach can be applied to a large variety of laser and semiconductor optical waveguide device

geometries. The optical behavior of the device including the propagation constant and mode profiles are obtained from the ECFD algorithm.

As it was shown, biasing conditions change the carrier density in the active layer. This causes the conductivity profile to change as well, and therefore also the propagation parameters of the laser when it is viewed as a lossy slow-wave transmission line structure. The conductivity profile will be used to model the laser's microwave behavior in the following chapter, in which the analysis of transitions and interconnection between the active and passive transmission lines will be investigated. The investigation presented in this chapter is only the first step in the full-wave electromagnetic field analysis of scattering at transitions between passive transmission lines and active devices, which follows in the next chapters.

Chapter 3

Characteristics of the FDTLM Symmetrical Condensed Nodes

3.1 Introduction

To characterize the microwave properties of semiconductor lasers and semiconductor based transmission lines, numerical techniques for full-wave electromagnetic field simulation are essential. The frequency-domain transmission line matrix (FDTLM) method is such a technique and will be used in the investigation to follow. The FDTLM method operates entirely in the frequency-domain and thus presents a complementary tool to the traditional time-domain TLM (TDTLM) (i.e. [3, 4]) approach. It expands the framework of the TLM technique from the time-domain to the frequency-domain utilizing the same space discretization network. In this technique, the space is modelled by a set of TLM nodes. The TLM nodes have evolved from the earlier expanded [32] and asymmetrical nodes [33] to the symmetrical condensed node (SCN) [34] most frequently used today.

Although frequency-domain data can also be obtained from time-domain TLM modeling of electromagnetic fields by means of a Fourier transform, this may not always be a computationally efficient approach, in particular if a guided wave structure needs to be characterized at only a few frequencies or over a small frequency range. Then the computation of the entire transient response - as required in the TDTLM method - appears to be an unnecessary computational expense. To avoid this problem, a first attempt of formulating the TLM algorithm directly in the frequency-domain was described in 1980

[5]. However, it was not until 1992 that this approach had been revisited (i.e. [6, 7, 8]) and a more complete algorithm has been developed (i.e. [35, 36, 37, 38, 39]) which is now known as the FDTLM. The frequency-domain TLM approach has the following features that distinguishes it from the time-domain TLM method: First, no impulse excitation is required, the transmission line matrix network is considered to be in steady-state; second, to discretize the computational domain the same transmission line matrix network used in the TDTLM method can be utilized; third, in order to maintain time synchronism when modeling an inhomogeneous structure the necessity of conditions in the time-domain TLM nodes has been eliminated.

All these features lead to a number of computational advantages of the FDTLM that can be summarized as follows: Since time-harmonic variations are assumed, only the space is discretized and no time iterations are necessary; time synchronism is eliminated and, thus, graded mesh layouts with large grading ratios can be easily utilized (the grading ratio is only limited by the acceptable numerical dispersion error), which is important for the simulation of semiconductor based guided wave structures; for isotropic substrate the node scattering matrix is always a 12x12 matrix, no matter whether homogeneous or inhomogeneous structures are involved; the network theory can be applied to greatly enhance the numerical efficiency of the frequency-domain computations.

The FDTLM algorithm is based on a variety of possible frequency-domain nodes. The nodes are characterized at the point at which the transmission lines, or link lines, intersect each other. The symmetrical condensed node (SCN) in the frequency-domain is the core of the algorithm, which was introduced by Jin, Vahldieck and Huang (i.e. [6, 7, 35]) and the formulation was based on the symmetrical condensed node in the time-domain (SCN) introduced by P.B. Johns [34]. To construct the SCN in the frequency domain, the 12-port scattering matrix is determined at the center of the node which can be derived either directly in the frequency-domain or from any of the existing time-domain nodes. Then, the scattering matrix at the ports of the node is obtained by shifting the reference planes from the center of the node to the ports of the twelve link transmission lines. To do so, the propagation characteristics of the link lines must be determined. There

are several approaches to accomplish this and each of the approaches leads to a different port scattering matrix.

In this chapter we investigate the possibility of developing the SCN and characterizing the FDTLM SCN by shunt and series equivalent circuit decomposition. We have also implemented the node notation proposed by Krumpholz and Russer [36] which has led to a symmetric matrix in a compact form. In case of lossless media, this matrix becomes Hermitian. It is noted that in the frequency-domain SCN the electric and magnetic losses are included in the various characteristic impedances and propagation constants of the link lines which become now complex quantities. Thus, the size of the SCN scattering matrix remains 12x12.

3.2 General Formulation of FDTLM Parameters

3.2.1 Basic Notation

Figure 3.1 sketches the FDTLM symmetrical condensed node (SCN) for a cell of arbitrary aspect ratios. This is a unit cell of the generalized three-dimensional transmission line network with 12 ports. The node is the intersection of the 12 link lines. The nodal center can be represented either by a set of three separate equivalent shunt or series transmission lines which merge into a single structure. This nodal structure forms a scattering center. After the structure of the node (shunt or series) and the characteristic impedances of the link lines are chosen, the voltages and currents determine the electric and magnetic field at each port of the space. The voltage waves incident on the node from each of the link lines are scattered at this scattering center to generate a set of scattered voltage waves. This is represented by the scattering matrix, $[S]$.

In the frequency-domain TLM, time-harmonic variations are assumed and hence only discretization in space is required. Incident voltage waves on each port are scattered to couple into other ports. By following the equivalences of the voltages and currents to the electric and magnetic fields, respectively, the differential equations that describe the behavior of voltages and currents at a FDTLM symmetrical condensed node are given in

the form as shown below.

$$
\begin{aligned}
v\frac{\partial I_z}{\partial y} - w\frac{\partial I_y}{\partial z} &= j\omega C_x V_x \quad ; \quad v\frac{\partial V_z}{\partial y} - w\frac{\partial V_y}{\partial z} = -j\omega L_x I_x \\
w\frac{\partial I_x}{\partial z} - u\frac{\partial I_z}{\partial x} &= j\omega C_y V_y \quad ; \quad w\frac{\partial V_x}{\partial z} - u\frac{\partial V_z}{\partial x} = -j\omega L_y I_y \\
u\frac{\partial I_y}{\partial x} - v\frac{\partial I_x}{\partial y} &= j\omega C_z V_z \quad ; \quad u\frac{\partial V_y}{\partial x} - v\frac{\partial V_x}{\partial y} = -j\omega L_z I_z
\end{aligned}
\tag{3.1}
$$

where u, v and w are the dimensions of the node in x, y, and z directions, respectively. The difference to reference [6, 7, 35] and this thesis is that we introduce a new scheme where the node numbering to each of the twelve ports have been assigned according [36]. This results in a novel symmetric scattering matrix, which is Hermitian in the case of lossless media. In this approach, the nodal inductances and capacitances of the TLM branches can be calculated from the relationship for the distributed inductances and capacitances of the link lines in all twelve polarized directions. The basic notation of the voltage pulse and other physical quantities attributed to a SCN is described as follows.

The total voltage V on a link transmission line consists of the sum of incident voltage, V^i, and reflected voltage V^r: $V = V^i + V^r$. Similarly the total current on a link line is $I = (V^i - V^r) / Z$, where Z is the characteristic impedance of the link line. By assuming the origin of the coordinates at the nodal center, a voltage pulse can be expressed in compact form as V_{+ij} or V_{-ij}, where dummy indices i ($i \in x, y, z$) represent the principal axis direction, and j ($j \in x, y, z$) denotes the polarization of the appropriate link transmission line. The port can be either on the positive (+) side or the negative (-) side of the nodal center. Furthermore, the parameters for each link line are introduced in terms of the distributed capacitance, C_{ij}, and inductance, L_{ij}, respectively. Similarly, the characteristic impedance and admittance of the link line are referred to as Z_{ij} and Y_{ij}, which are defined as:

$$
Y_{ij} = \frac{1}{Z_{ij}} = \sqrt{\frac{C_{ij}}{L_{ij}}} \tag{3.2}
$$

and the corresponding propagation constant of the related link line can be written as:

$$\Upsilon_{ij} = \omega\sqrt{L_{ij} \cdot C_{ij}} \tag{3.3}$$

where $i, j \in \{x, y, z\}$ and $i \neq j$; ω is the radian frequency ($= 2\pi f$).

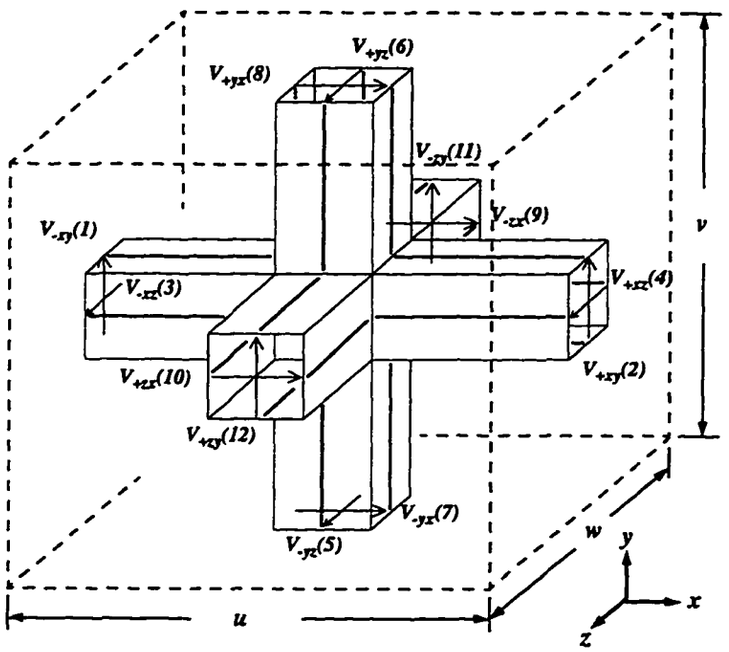

Figure 3.1 The FDTLM symmetrical condensed node (SCN).

3.2.2 Constitutive Relationships for the General FDTLM SCN

The general constitutive relations used to derive the frequency-domain TLM nodes correspond to the parameters that determine the nodal cell space and the link lines. The nodal cell can be a graded mesh with arbitrary node dimensions u, v, w, or Δx, Δy, Δz in the x, y and z directions, respectively. The total capacitance of the cell block can be calculated from the general definition of the capacitance:

$$C = \frac{Q}{V} = \frac{\int_S \varepsilon \boldsymbol{E} \cdot d\boldsymbol{S}}{\int_+ \boldsymbol{E} \cdot d\boldsymbol{l}} \tag{3.4}$$

Therefore, the capacitance along the three axis can be expressed as [40]:

$$C_x = \varepsilon \frac{vw}{u} = \varepsilon \frac{\Delta y \Delta z}{\Delta x} \tag{3.5a}$$

$$C_y = \varepsilon \frac{uw}{v} = \varepsilon \frac{\Delta x \Delta z}{\Delta y} \tag{3.5b}$$

$$C_z = \varepsilon \frac{uv}{w} = \varepsilon \frac{\Delta x \Delta y}{\Delta z} \tag{3.5c}$$

Similarly, according to the total inductance of the cell block the inductance along the three principal axis direction can be written as [40]:

$$L_x = \mu \frac{vw}{u} = \mu \frac{\Delta y \Delta z}{\Delta x} \tag{3.6a}$$

$$L_y = \mu \frac{uw}{v} = \mu \frac{\Delta x \Delta z}{\Delta y} \tag{3.6b}$$

$$L_z = \mu \frac{uv}{w} = \mu \frac{\Delta x \Delta y}{\Delta z} \tag{3.6c}$$

where ε and μ is the permittivity ($= \varepsilon_0 \varepsilon_r$) and permeability ($= \mu_0 \mu_r$) of the modelled medium. For anisotropic media ε and μ become tensors.

The components C_i and L_i ($i \in \{x, y, z\}$) represent the total capacitance and inductance of the cell in the medium which is related to the distributed capacitance and inductance of the link transmission lines of a SCN. In other words, the equations represented in (3.5a) - (3.6c) must hold for any FDTLM nodes constructed by an arbitrary combination of the distributed capacitances and inductances of the link lines. Therefore, Eqs. (3.5a) - (3.6c) are called the general FDTLM SCN constitutive relationships. For example, the total capacitance in the x-direction modeled by the SCN is illustrated in Figure 3.2. It is evident that the total capacitance of the cell block is related to the two distributed capacitance in the x-polarizated direction of the link lines (equivalent shunt

circuit in x-direction). The length of the related transmission lines are v and w, respectively. Thus the total capacitance can be expressed as:

$$C_x = C_{yx}v + C_{zx}w = \varepsilon \frac{vw}{u} \tag{3.7a}$$

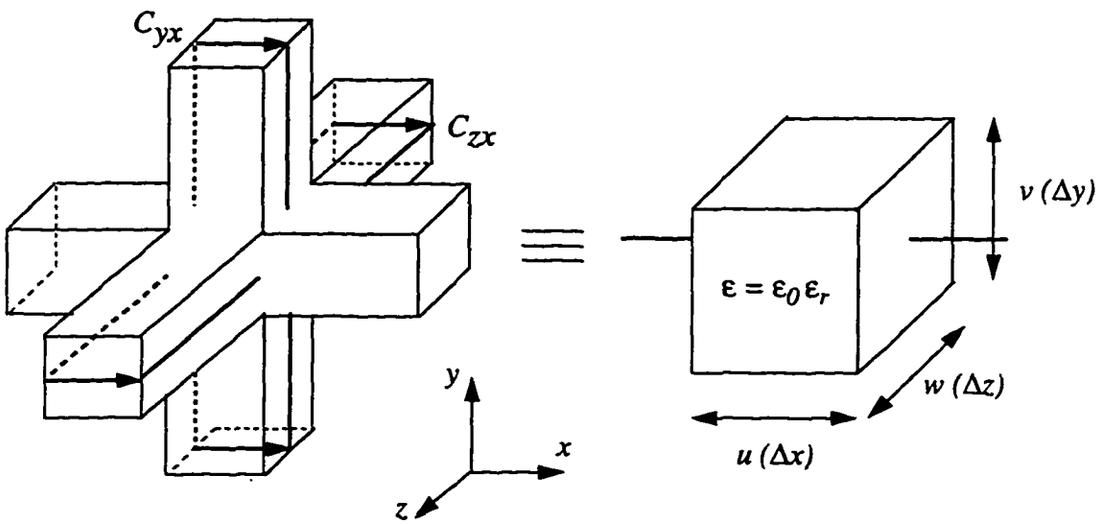

Figure 3.2 Modeling the total capacitance in the x-direction.

Considering the other two possible polarization direction yields the following constitutive relations for the capacitance:

$$C_y = C_{xy}u + C_{zy}w = \varepsilon \frac{uw}{v} \tag{3.7b}$$

$$C_z = C_{xz}u + C_{yz}v = \varepsilon \frac{uv}{w} \tag{3.7c}$$

Similarly, the constitutive relations for the inductance is obtained. For example, the total inductance in the x-direction modeled by the SCN is illustrated in Figure 3.2. The total inductance of the cell block is represented by the two distributed inductances in the y- and z-polarizated direction of the link lines, which form an equivalent series circuit corresponding to the x-direction of the magnetic field. The length of the related transmission lines are v and w, respectively. Thus the total inductance in the x-direction

can be expressed as:

$$L_x = L_{yz}v + L_{zy}w = \mu \frac{vw}{u} \tag{3.8a}$$

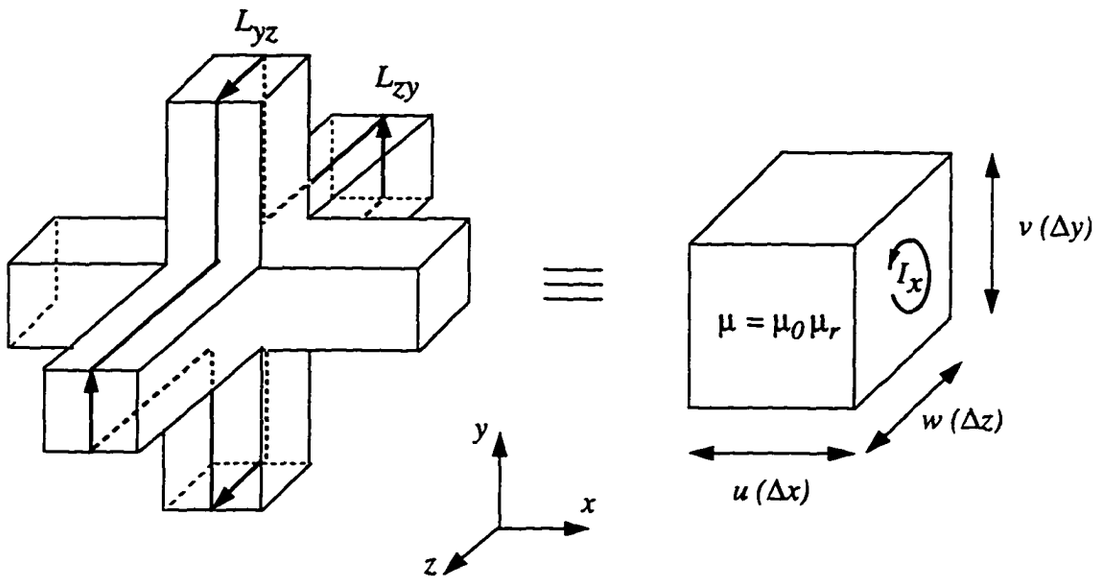

Figure 3.3 Modeling the total inductance in the x-direction.

Considering the other two possible polarization directions, the total inductances in the y and z-direction are represented as the following SCN constitutive relations:

$$L_y = L_{xz}u + L_{zx}w = \mu \frac{uw}{v} \tag{3.8b}$$

$$L_z = L_{xy}u + L_{yx}v = \mu \frac{uv}{w} \tag{3.8c}$$

The SCN constitutive relations represented by Eqs. (3.7a) - (3.8c) can be written in compact form by using the dummy indices i, j, k as:

$$C_i = C_{ji}\Delta j + C_{ki}\Delta k = \varepsilon \frac{\Delta j \Delta k}{\Delta i} \tag{3.9}$$

$$L_i = L_{jk}\Delta j + L_{kj}\Delta k = \mu \frac{\Delta j \Delta k}{\Delta i} \tag{3.10}$$

where $i, j, k \in \{x, y, z\}$ and $i \neq j \neq k$. This means that there are a total of six equations which represent the general constitutive relations of the FDTLM SCN. These relations can be applied to the derivation of the FDTLM nodes. It is also shown that these equations contain 12 link line parameters which are the six distributed capacitances and the six distributed inductances of the link transmission lines. Hence, there exists six degrees of freedom for determining the link line parameters in a FDTLM node.

3.3 Scattering in Symmetrical Condensed Nodes

3.3.1 Generalized Scattering Equations of the SCN

In order to determine the scattering matrix of the frequency-domain hybrid node with the new port notation [36] (in Figure 3.1), we can consider the node as a composition of three sets of shunt and series nodes (in Figure 3.4) coupled at the nodal center. The scattering matrix for the SCN can be found from either Maxwell's equations using the concept of charge and energy conservation which depends on the solution of a set of nonlinear simultaneous equations [37, 40], as it is done conventionally, or by following a very simple and elegant method empirically proposed by Naylor and Ait-Sadi [41] for any time-domain TLM node. The former method is unwieldy as it depends on the solution of non-linear simultaneous equations and it is not easy to enforce the physical conditions. The procedure becomes very complex and tedious for deriving the algorithms of the general FDTLM nodes in practical use. We follow the latter and apply this method to frequency-domain TLM nodes. In this approach a FDTLM node can be represented by three pairs of shunt and series nodes [38, 39, 41] as shown in Figure 3.1 For a set of shunt and series nodes, there is always one pair of voltages that is common to the shunt and series circuits. For the example in Figure 3.4 these are voltages V_1 and V_2. Averaging the appropriate voltages and currents at the center of the node yields a pair of equations which interrelate reflected and incident voltages [41], such as:

$$V_L^r = V_n + I_n Z_L - V_R^i \tag{3.11}$$

$$V_R^r = V_n - I_n Z_R - V_L^i \tag{3.12}$$

where V_n and I_n are nodal voltage and loop current, respectively. Z_L and Z_R are the characteristic impedances of the corresponding link lines on the left hand side and right hand side. The method is extremely simple and it satisfies the scattering properties of any symmetrical condensed node.

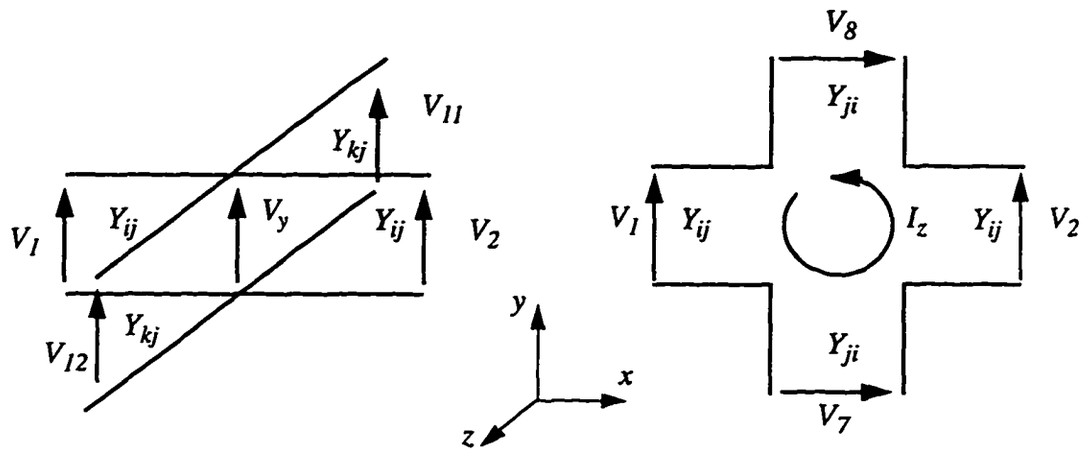

(a) equivalent shunt node *(b) equivalent series node*

Figure 3.4 One set of the equivalent shunt and series representations for the symmetrical condensed FDTLM node.

The characteristic admittances of the node depend on the link lines and are different. The general scattering equations for the voltages in the example of Figure 3.4 are written as:

$$V_1^r = V_y + I_z \cdot \frac{1}{Y_{ij}} - V_2^i \tag{3.13}$$

$$V_2^r = V_y - I_z \cdot \frac{1}{Y_{ij}} - V_1^i \tag{3.14}$$

From transmission line theory and the parallel generator theorem, the Thevenin equivalent [42, 43] can be used to determine the nodal voltage:

$$V_y = \frac{2Y_{ij}\left(V_1^i + V_2^i\right) + 2Y_{kj}\left(V_{11}^i + V_{12}^i\right)}{2\left(Y_{ij} + Y_{kj}\right)} \tag{3.15}$$

In the same way, the loop current for the equivalent series circuit can also be determined.

$$I_z = \frac{1}{Z_{ij} + Z_{ji}}\left(-V_1^i + V_2^i + V_7^i - V_8^i\right) \tag{3.16a}$$

or

$$I_z = \frac{Y_{ij} \cdot Y_{ji}}{Y_{ij} + Y_{ji}}\left(-V_1^i + V_2^i + V_7^i - V_8^i\right) \tag{3.16b}$$

This procedure can be repeated for all other pairs of link lines within the SCN by applying Eqs. (3.11) and (3.12). Inserting Eqs. (3.15) and (3.16b) into Eqs. (3.11) and (3.12) the elements of the scattering matrix can be determined at the node's center.

3.3.2 Derivation of the Generalized Scattering Equations

Considering the nodal center as a scattering center, the incident and reflected voltage waves travel forward and backward along the link transmission lines with certain polarization. The total voltage on an individual link line at the nodal center is the sum of both voltages, $V_L=V_L^i+V_L^r$, on the left hand side and the voltages, $V_R=V_R^i+V_R^r$, on the right hand side where V_L is not equal to V_R. This is illustrated in Figure 3.4(a) and Figure 3.4(b). In Figure 3.4(a) an equivalent total voltage, V_n, at the nodal center of the node can be described by an average voltage of V_R and V_L:

$$V_n = \frac{Y_L}{Y_L + Y_R} \cdot V_L + \frac{Y_R}{Y_L + Y_R} \cdot V_R \tag{3.17}$$

Similarly, the total current on the either side of the individual link line at the center of the node can be represented by:

$$I_L = \frac{1}{Z_L}\left(V_L^i - V_L^r\right) \tag{3.18a}$$

$$I_R = \frac{1}{Z_R}\left(V_R^i - V_R^r\right) \tag{3.18b}$$

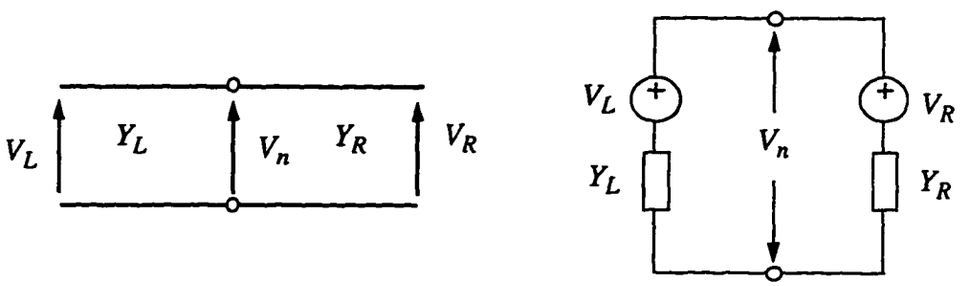

(a) equivalent total voltage *(b) equivalent circuit*

Figure 3.5 Circuit for calculating the total voltage of the scattering property.

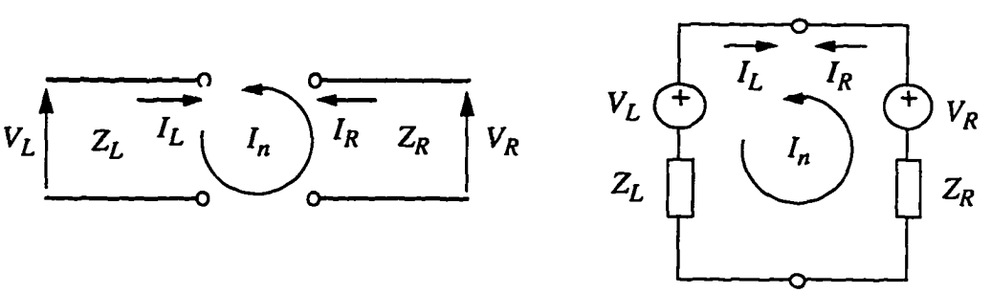

(a) equivalent total current *(b) equivalent circuit*

Figure 3.6 Circuit for calculating the total current of the scattering property.

In Figure 3.4(b) the equivalent total current can be defined by averaging the total current, I_L and I_R, at the nodal center:

$$I_n = \frac{Z_R}{Z_L + Z_R} \cdot I_R - \frac{Z_L}{Z_L + Z_R} \cdot I_L \tag{3.19}$$

where $Z_{L,R} = 1/Y_{L,R}$ is the characteristic impedance of the transmission lines. Eqs. (3.17)

and (3.19) can be rewritten as:

$$V_n = \frac{Z_R}{Z_L+Z_R}\left(V_L^i + V_L^r\right) + \frac{Z_L}{Z_L+Z_R}\left(V_R^i + V_R^r\right) \tag{3.20}$$

$$I_n = \frac{1}{Z_L+Z_R}\left(V_R^i - V_R^r\right) - \frac{1}{Z_L+Z_R}\left(V_L^i - V_L^r\right) \tag{3.21}$$

Solving Eqs. (3.20) and (3.21) for $V_L{}^r$ and $V_L{}^i$ yields

$$V_L^r = V_n + I_n Z_L - \frac{2Z_L}{Z_L+Z_R}\cdot V_R^i + \frac{Z_L-Z_R}{Z_L+Z_R}\cdot V_L^i \tag{3.22}$$

$$V_R^r = V_n - I_n Z_R - \frac{2Z_R}{Z_L+Z_R}\cdot V_L^i + \frac{Z_R-Z_L}{Z_L+Z_R}\cdot V_R^i \tag{3.23}$$

These two equations can be rewritten as follow by introducing the factor $\pm[Z_R/(Z_L+Z_R)]$ on the right hand side of Eq. (3.22) and the factor $\pm[Z_L/(Z_L+Z_R)]$ on the right hand side of Eq. (3.23):

$$V_L^r = V_n + I_n Z_L - V_R^i + h_{LR} \tag{3.24}$$

$$V_R^r = V_n - I_n Z_R - V_L^i + h_{LR} \tag{3.25}$$

where h_{LR} is defined as:

$$h_{LR} = \frac{Z_L-Z_R}{Z_L+Z_R}\left(V_L^i - V_R^i\right) \tag{3.26}$$

Eqs. (3.24) and (3.25) represent the general case of the scattering process. In the case of $Z_L = Z_R$, Eqs. (3.24) and (3.25) become the scattering equations as expressed in Eqs. (3.11) and (3.12) which was empirically introduced by Naylor and Ait-Saidi [41]. In order to derive the scattering matrix of the SCN, the nodal voltage and loop current must be expressed in terms of the incident voltages, such as Eqs. (3.15) and (3.16a) for the x-direction with y-polarization, by using Thevenin equivalent circuit or by applying charge and magnetic flux conservation law. Similar procedures can also be carried out for the

other link lines. In this way a complete set of the scattering equations can be obtained. This will be discussed in the following section.

3.4 Derivation of a Class of the FDTLM SCNs

3.4.1 Scattering Matrix of the SCN

The SCN is the "workhorse" of the FDTLM and represented an intersection of the twelve link lines with certain characteristic impedances (or admittances) and propagation constants. The voltage waves are incident upon the SCN from each of the link lines. These waves are then scattered to produce a set of scattered voltage waves, which become incident on the adjacent SCN. The scattering matrix is the representative of the SCN in terms of the incident and scattered voltage waves. The process of scattering can be written as:

$$[V^r] = [S][V^i] \tag{3.27}$$

where $[S]$ is the scattering matrix at the center of the node, which may be a twelve by twelve matrix corresponding to a twelve-port network. To represent the SCN in the frequency domain, the scattering matrix is first derived at the center of the node. Then, by shifting the reference planes from the node's center to the ports of the twelve link lines the scattering matrix of the frequency-domain SCN is obtained. Instead of the scattering process to occur at the nodal point, the scattering in the frequency-domain node is referred to the ports of the SCN. This is one of the major differences between the time-domain and frequency-domain TLM scheme. To transfer the scattering process to the ports, the link line parameters and their propagation constants must be determined. There are different possibilities to achieve this leading to different scattering matrix representations in frequency-domain TLM.

The derivation begins with the scattering equation. Using the procedures given in the previous section, the scattering equations of an SCN corresponding to the voltage wave scattering on the other link line can be found from the following complete set of equations:

$$V_1^r = V_{-xy}^r = V_y + I_z Z_{-xy} - V_{xy}^i + h_{xy} = V_y + I_z Z_{-xy} - V_2^i + h_{xy} \tag{3.28a}$$

$$V_2^r = V_{xy}^r = V_y - I_z Z_{xy} - V_{-xy}^i + h_{xy} = V_y - I_z Z_{xy} - V_1^i + h_{xy} \tag{3.28b}$$

$$V_3^r = V_{-xz}^r = V_z - I_y Z_{-xz} - V_{xz}^i + h_{xz} = V_z - I_y Z_{-xz} - V_4^i + h_{xz} \tag{3.28c}$$

$$V_4^r = V_{xz}^r = V_z + I_y Z_{xz} - V_{-xz}^i + h_{xz} = V_z + I_y Z_{xz} - V_3^i + h_{xz} \tag{3.28d}$$

$$V_5^r = V_{-yz}^r = V_z + I_x Z_{-yz} - V_{yz}^i + h_{yz} = V_z + I_x Z_{-yz} - V_6^i + h_{yz} \tag{3.28e}$$

$$V_6^r = V_{yz}^r = V_z - I_x Z_{yz} - V_{-yz}^i + h_{yz} = V_z - I_x Z_{yz} - V_5^i + h_{yz} \tag{3.28f}$$

$$V_7^r = V_{-yx}^r = V_x - I_z Z_{-yx} - V_{yx}^i + h_{yx} = V_x - I_z Z_{-yx} - V_8^i + h_{yx} \tag{3.28g}$$

$$V_8^r = V_{yx}^r = V_x + I_z Z_{yx} - V_{-yx}^i + h_{yx} = V_x + I_z Z_{yx} - V_7^i + h_{yx} \tag{3.28h}$$

$$V_9^r = V_{-zx}^r = V_x + I_y Z_{-zx} - V_{zx}^i + h_{zx} = V_x + I_y Z_{-zx} - V_{10}^i + h_{zx} \tag{3.28i}$$

$$V_{10}^r = V_{zx}^r = V_x - I_y Z_{zx} - V_{-zx}^i + h_{zx} = V_x - I_y Z_{zx} - V_9^i + h_{zx} \tag{3.28j}$$

$$V_{11}^r = V_{-zy}^r = V_y - I_x Z_{-zy} - V_{zy}^i + h_{zy} = V_y - I_x Z_{-zy} - V_{12}^i + h_{zy} \tag{3.28k}$$

$$V_{12}^r = V_{zy}^r = V_y + I_x Z_{zy} - V_{-zy}^i + h_{zy} = (V_y + I_x Z_{zy}) - V_{11}^i + h_{zy} \tag{3.28l}$$

The nodal voltage (V_x, V_y, V_z) and the loop current (I_x, I_y, I_z) can be found either by using Thevenin's theorem as proposed by Naylor and Ait-Sadi [41] or by the conservation of charge and magnetic flux [43, 44] because the center of the node is treated as an undefined region in which the link lines from adjacent nodes converge. For example, the nodal voltage in the y-direction in terms of the incident voltages and the admittances of the corresponding link lines can be expressed as:

$$V_y = 2\frac{Y_{-xy}V_{-xy}^i + Y_{xy}V_{xy}^i + Y_{-zy}V_{-zy}^i + Y_{zy}V_{zy}^i}{Y_{-xy} + Y_{xy} + Y_{-zy} + Y_{zy}} \tag{3.29}$$

whereas the loop current contributing to the magnetic field in the z-direction is found as:

$$I_z = 2\frac{-V^i_{-xy} + V^i_{xy} - V^i_{yx} + V^i_{-yx}}{Z_{-xy} + Z_{xy} + Z_{-yx} + Z_{yx}} \tag{3.30}$$

In order to formulate the scattering matrix for the symmetrical condensed node the impedances (or admittances) of the link line must be set as:

$$Y_{-xy} = Y_{xy} = 1/Z_{-xy} = 1/Z_{xy} \tag{3.31a}$$

$$Y_{-yx} = Y_{yx} = 1/Z_{-yx} = 1/Z_{yx} \tag{3.31b}$$

$$Y_{-zy} = Y_{zy} = 1/Z_{-zy} = 1/Z_{zy} \tag{3.31c}$$

The nodal voltage in the y-direction and the loop current in the z-direction can be rewritten in the form of Eqs. (3.15) and (3.16b). Substituting Eqs. (3.29) and (3.30) into Eqs. (3.28a) and (3.28b), the reflected voltages on the link lines 1 and 2 with the incident voltages on the other link line are found directly as follows:

$$V^r_1 = \frac{Y_{xy} - Y_{zy}}{2(Y_{xy} + Y_{zy})}\left(V^i_1 + V^i_2\right) + \frac{Y_{xy} - Y_{yx}}{2(Y_{xy} + Y_{yx})}\left(V^i_1 - V^i_2\right)$$

$$+ \frac{Y_{yx}}{Y_{xy} + Y_{yx}}\left(V^i_7 - V^i_8\right) + \frac{Y_{zy}}{Y_{xy} + Y_{zy}}\left(V^i_{11} + V^i_{12}\right) \tag{3.32}$$

$$V^r_2 = \frac{Y_{xy} - Y_{zy}}{2(Y_{xy} + Y_{zy})}\left(V^i_1 + V^i_2\right) - \frac{Y_{xy} - Y_{yx}}{2(Y_{xy} + Y_{yx})}\left(V^i_1 - V^i_2\right)$$

$$- \frac{Y_{yx}}{Y_{xy} + Y_{yx}}\left(V^i_7 - V^i_8\right) + \frac{Y_{zy}}{Y_{xy} + Y_{zy}}\left(V^i_{11} + V^i_{12}\right) \tag{3.33}$$

with the assignment of

$$a_{xy} = \frac{Y_{xy} - Y_{zy}}{2(Y_{xy} + Y_{zy})} + \frac{Y_{xy} - Y_{yx}}{2(Y_{xy} + Y_{yx})} \tag{3.34a}$$

$$b_{xy} = \frac{Y_{zy}}{Y_{xy} + Y_{zy}} \tag{3.34b}$$

$$c_{xy} = \frac{Y_{yx}}{Y_{xy} + Y_{yx}} \tag{3.34c}$$

$$d_{xy} = \frac{Y_{xy} - Y_{zy}}{2\,(Y_{xy} + Y_{zy})} - \frac{Y_{xy} - Y_{yx}}{2\,(Y_{xy} + Y_{yx})} \tag{3.34d}$$

This procedure can be repeated for all other pairs of the link lines within the SCN to find all the scattering matrix elements. By using dummy indices the scattering matrix, S, for the symmetrical condensed node can be present in the following compact form:

$$S = \begin{bmatrix}
a_{ij} & d_{ij} & 0 & 0 & 0 & 0 & c_{ij} & -c_{ij} & 0 & 0 & b_{ij} & b_{ij} \\
d_{ij} & a_{ij} & 0 & 0 & 0 & 0 & -c_{ij} & c_{ij} & 0 & 0 & b_{ij} & b_{ij} \\
0 & 0 & a_{ik} & d_{ik} & b_{ik} & b_{ik} & 0 & 0 & c_{ik} & -c_{ik} & 0 & 0 \\
0 & 0 & d_{ik} & a_{ik} & b_{ik} & b_{ik} & 0 & 0 & -c_{ik} & c_{ik} & 0 & 0 \\
0 & 0 & b_{jk} & b_{jk} & a_{jk} & d_{jk} & 0 & 0 & 0 & 0 & c_{jk} & -c_{jk} \\
0 & 0 & b_{jk} & b_{jk} & d_{jk} & a_{jk} & 0 & 0 & 0 & 0 & -c_{jk} & c_{jk} \\
c_{ji} & -c_{ji} & 0 & 0 & 0 & 0 & a_{ji} & d_{ji} & b_{ji} & b_{ji} & 0 & 0 \\
-c_{ji} & c_{ji} & 0 & 0 & 0 & 0 & d_{ji} & a_{ji} & b_{ji} & b_{ji} & 0 & 0 \\
0 & 0 & c_{ki} & -c_{ki} & 0 & 0 & b_{ki} & b_{ki} & a_{ki} & d_{ki} & 0 & 0 \\
0 & 0 & -c_{ki} & c_{ki} & 0 & 0 & b_{ki} & b_{ki} & d_{ki} & a_{ki} & 0 & 0 \\
b_{kj} & b_{kj} & 0 & 0 & c_{kj} & -c_{kj} & 0 & 0 & 0 & 0 & a_{kj} & d_{kj} \\
b_{kj} & b_{kj} & 0 & 0 & -c_{kj} & c_{kj} & 0 & 0 & 0 & 0 & d_{kj} & a_{kj}
\end{bmatrix} \tag{3.35}$$

where

$$a_{ij} = \frac{Y_{ij} - Y_{kj}}{2\,(Y_{ij} + Y_{kj})} + \frac{Y_{ij} - Y_{ji}}{2\,(Y_{ij} + Y_{ji})} \tag{3.36a}$$

$$b_{ij} = \frac{Y_{kj}}{Y_{ij} + Y_{kj}} \tag{3.36b}$$

$$c_{ij} = \frac{Y_{ji}}{Y_{ij} + Y_{ji}} \tag{3.36c}$$

$$d_{ij} = \frac{Y_{ij} - Y_{kj}}{2\,(Y_{ij} + Y_{kj})} - \frac{Y_{ij} - Y_{ji}}{2\,(Y_{ij} + Y_{ji})} \tag{3.36d}$$

The indices $i, j, k \in \{x, y, z\}$ can have all possible combinations except $i = j = k$. The normalized characteristic impedances (or admittances) of the link lines are according to the field polarization and are defined as follows:

$$\begin{aligned} Y_{\pm xy} &= 1/Z_{\pm xy} = Y_{ij} \;;\; Y_{\pm yx} = 1/Z_{\pm yx} = Y_{ji} \\ Y_{\pm xz} &= 1/Z_{\pm xz} = Y_{ik} \;;\; Y_{\pm yz} = 1/Z_{\pm yz} = Y_{jk} \\ Y_{\pm zx} &= 1/Z_{\pm zx} = Y_{ki} \;;\; Y_{\pm zy} = 1/Z_{\pm zy} = Y_{kj} \end{aligned} \tag{3.37}$$

The scattering matrix (3.35) is symmetric and, generally, the elements are complex because the characteristic impedances (or admittances) of the link lines take the electric conductivity and magnetic conductivity into account. In case of a lossless medium, the matrix becomes Hermitian.

3.4.2 The Different FDTLM Schemes Based on the SCN

The next step in the development is to shift the symbolic scattering matrix from the center of the node to the ports. This is possible only after the characteristic impedances and the propagation constants of the link lines are determined [37, 38, 39]. There are several approaches to accomplish this and each of the approaches leads to a different port scattering matrix. Huang has investigated the following three possibilities [37]: The propagation constant is the same on all link lines and the characteristic admittances are calculated accordingly (*Propagation Constant Node*); the characteristic impedance is the same on all link lines and the propagation constant is calculated accordingly (*Characteristic Admittance Node*); the SCN is considered as three series and shunt nodes coupled at the center of the node, whereby the link lines may be considered as either equivalent series or shunt link lines. In [37] the link lines were only considered as series lines. By defining the characteristic impedances on the three sets of the series link lines, the propagation constants can be calculated (*Hybrid Node with Series Decomposition*). To complete this investigation, the hybrid SCN with shunt link lines is considered. We call

this node the *Hybrid Node with Shunt Decomposition* to distinguish it from the *Hybrid Node with Series Decomposition.* As it will be shown later the dispersion error of this node is considerably reduced.

It should be noted that both frequency-domain hybrid nodes are different from the hybrid nodes in the time-domain which were proposed by Scaramuzza and Lowery [45]. In the latter the characteristic impedances or admittances of the link lines are real quantities and are varied to account for a graded mesh as well as to model the property of the medium. Furthermore, shunt-circuited open stubs are needed to maintain time synchronism throughout the mesh if an inhomogeneous propagation medium is modelled or if losses need to be accounted for. Although the resulting S-matrix in the time-domain hybrid node contains only real elements its size can vary from 12x12 (lossless homogeneous case) to 18x18 (lossy electric and magnetic material).

In the frequency-domain hybrid node (as in all FDTLM nodes) stubs are eliminated. The electric and magnetic losses are included in the various characteristic impedances and propagation constants of the link lines which become now complex quantities. The size of the S-matrix is maintained 12 x 12.

1) ***The Characteristic Admittance Node***: This FDTLM node assumes that the characteristic admittance of each link transmission line is the same and equals the intrinsic admittance, Y_0, of the medium. The normalized propagation constants in each direction of the SCN can then be obtained from the node's dimensions as

$$\tilde{\gamma}_x = \frac{\gamma_x}{k_0} = \frac{1}{2}\left(\frac{v^2+w^2}{vw} - \frac{vw}{u^2}\right) \tag{3.38a}$$

$$\tilde{\gamma}_y = \frac{\gamma_y}{k_0} = \frac{1}{2}\left(\frac{u^2+w^2}{uw} - \frac{uw}{v^2}\right) \tag{3.38b}$$

$$\tilde{\gamma}_z = \frac{\gamma_x}{k_0} = \frac{1}{2}\left(\frac{u^2+v^2}{uv} - \frac{uv}{w^2}\right) \tag{3.38c}$$

In general, these propagation constants are complex when modeling permittivity and

permeability in lossy media.

2) ***The Propagation Constant Node***: In contrast to the previous approach, the characteristic admittances of the link lines are different and have been selected as follows:

$$Y_{\pm xy} = \frac{w}{v}Y_0 \;;\; Y_{\pm yx} = \frac{w}{u}Y_0$$

$$Y_{\pm xz} = \frac{v}{w}Y_0 \;;\; Y_{\pm yz} = \frac{u}{w}Y_0 \tag{3.39}$$

$$Y_{\pm zx} = \frac{v}{u}Y_0 \;;\; Y_{\pm zy} = \frac{u}{v}Y_0$$

According to the FDTLM basic notation and the SCN's constitutive relations Eqs. (3.9) and (3.10), the following two groups of linear equations for the normalized propagation constants on the link lines can be obtained in terms of the total capacitances and inductances along the three axis directions:

$$\tilde{\gamma}_{yx} + \tilde{\gamma}_{xz} = 1 \tag{3.40a}$$

$$\tilde{\gamma}_{xy} + \tilde{\gamma}_{zy} = 1 \tag{3.40b}$$

$$\tilde{\gamma}_{xz} + \tilde{\gamma}_{yz} = 1 \tag{3.40c}$$

$$\tilde{\gamma}_{yz} + \tilde{\gamma}_{zy} = 1 \tag{3.41a}$$

$$\tilde{\gamma}_{xz} + \tilde{\gamma}_{zx} = 1 \tag{3.41b}$$

$$\tilde{\gamma}_{xy} + \tilde{\gamma}_{yx} = 1 \tag{3.41c}$$

where the normalized propagation constants can be expressed by:

$$\tilde{\gamma}_{ij} = \frac{\gamma_{ij}}{k_0} = \frac{\omega(C_{ij}/Y_{ij})}{\omega(\varepsilon/Y_0)} \tag{3.42}$$

or

$$\tilde{\gamma}_{ij} = \frac{\gamma_{ij}}{k_0} = \frac{\omega(L_{ij}Y_{ij})}{\omega(\mu Y_0)} \tag{3.43}$$

γ_{ij} is the propagation constant on the link line and k_0 the propagation constant in the medium. ω is the radian frequency ($= 2\pi f$). Further, the normalized propagation constant in the x, y and z directions are selected the same for both polarized components along each space direction. The solutions of Eqs. (3.40a)-(3.41c) gives:

$$\tilde{\gamma}_x = \tilde{\gamma}_{xy} = \tilde{\gamma}_{xz} = \frac{1}{2} \tag{3.44a}$$

$$\tilde{\gamma}_y = \tilde{\gamma}_{yx} = \tilde{\gamma}_{yz} = \frac{1}{2} \tag{3.44b}$$

$$\tilde{\gamma}_z = \tilde{\gamma}_{zx} = \tilde{\gamma}_{zy} = \frac{1}{2} \tag{3.44c}$$

Therefore, it can be seen that if the characteristic admittances are so selected, the propagation constants along all 12 link lines are the same and equal to 1/2 of the intrinsic propagation constant k_o of the medium. The disadvantage of this node is that due to the same propagation constants a graded mesh cannot be utilized.

3) ***The Hybrid Node***: In this case the SCN is considered as three shunt nodes and three series nodes coupled at the center of the node as illustrated in Figure 3.7. In the hybrid node with *series decomposition* three characteristic admittances are chosen which are related to the inductances of the series link lines, *i.e.*,

$$Y_{ij} = Y_{ji} = \frac{sw}{uv}\sqrt{\frac{\varepsilon}{\mu}} \tag{3.45a}$$

$$Y_{ik} = Y_{ki} = \frac{sv}{uw}\sqrt{\frac{\varepsilon}{\mu}} \tag{3.45b}$$

$$Y_{ji} = Y_{kj} = \frac{su}{vw}\sqrt{\frac{\varepsilon}{\mu}} \tag{3.45c}$$

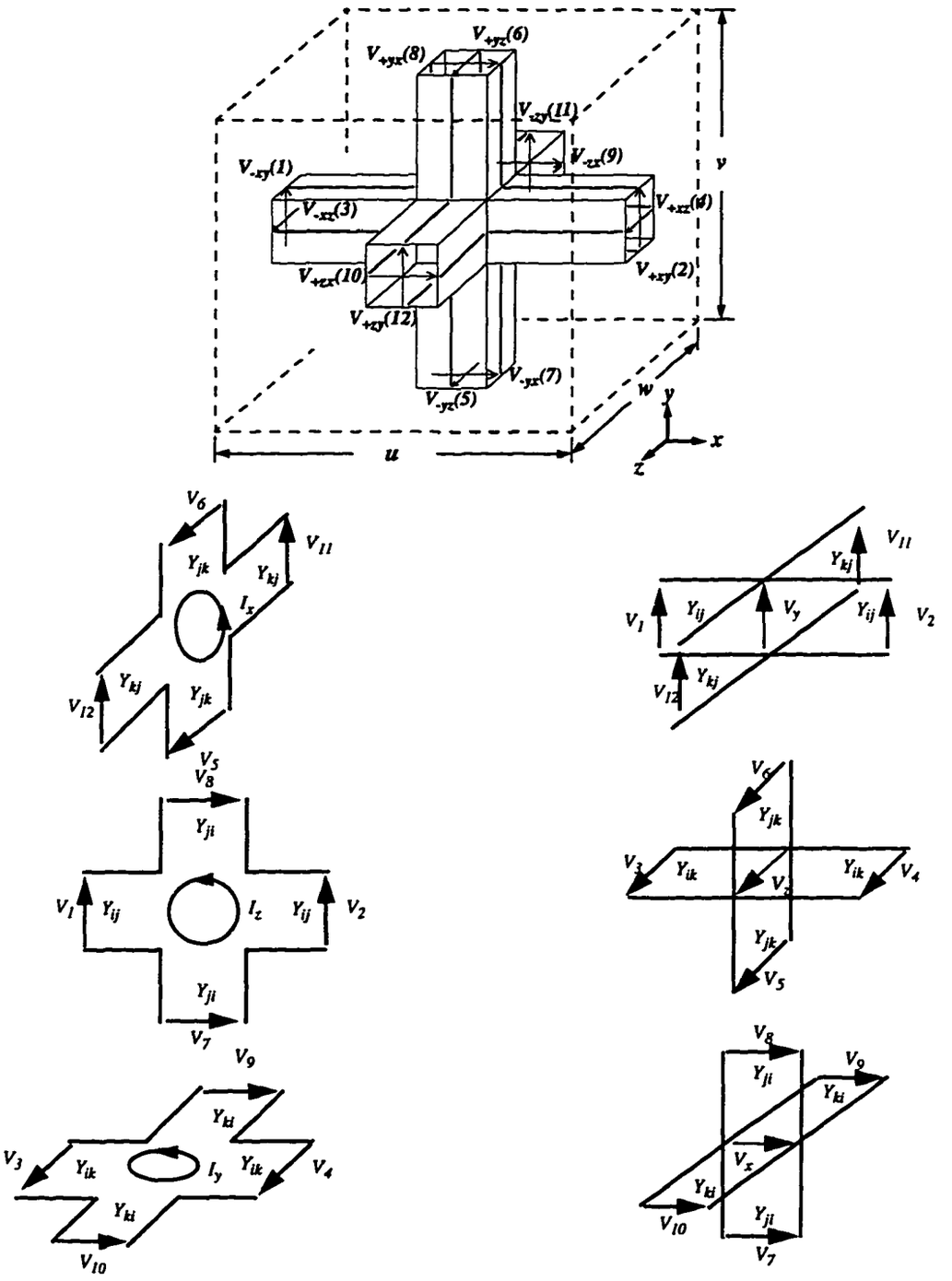

Figure 3.7 The FDTLM hybrid SCN with series and shunt decomposition.

The normalized propagation constants of all link lines are then given as

$$\tilde{\gamma}_{xy}=\frac{\gamma_{xy}}{k_0}=\frac{su}{u^2+v^2};\qquad \tilde{\gamma}_{yx}=\frac{\gamma_{yx}}{k_0}=\frac{sv}{u^2+v^2}$$

$$\tilde{\gamma}_{xz}=\frac{\gamma_{xz}}{k_0}=\frac{uv^2}{s\left(u^2+v^2\right)};\qquad \tilde{\gamma}_{yz}=\frac{\gamma_{yz}}{k_0}=\frac{vu^2}{s\left(u^2+v^2\right)} \tag{3.46}$$

$$\tilde{\gamma}_{zx}=\frac{\gamma_{zx}}{k_0}=\frac{w\left(u^2+v^2-s^2\right)}{s\left(u^2+v^2\right)};\quad \tilde{\gamma}_{zy}=\frac{\gamma_{zy}}{k_0}=\tilde{\gamma}_{zx}$$

On the other hand, in the hybrid node with *shunt decomposition*, shown in Figure 3.7, three characteristic admittances of the corresponding shunt transmission lines are chosen, which are related to the capacitances of the link lines, *i.e.*,

$$Y_{ij}=Y_{kj}=\frac{uw}{sv}\sqrt{\frac{\varepsilon}{\mu}} \tag{3.47a}$$

$$Y_{ik}=Y_{jk}=\frac{uv}{sw}\sqrt{\frac{\varepsilon}{\mu}} \tag{3.47b}$$

$$Y_{ji}=Y_{ki}=\frac{vw}{su}\sqrt{\frac{\varepsilon}{\mu}} \tag{3.47c}$$

where $s=\sqrt{\left(u^2w^2+u^2v^2+v^2w^2\right)/\left(u^2+v^2+w^2\right)}$; u, v and w are the dimensions of the node in x, y, and z directions, respectively. From the SCN's constitutive relations, the normalized propagation constants of the corresponding link transmission lines can be directly derived as:

$$\tilde{\gamma}_{xy}=\frac{\gamma_{xy}}{k_0}=\frac{uv^2}{s\left(u^2+v^2\right)};\qquad \tilde{\gamma}_{yx}=\frac{\gamma_{yx}}{k_0}=\frac{u^2v}{s\left(u^2+v^2\right)}$$

$$\tilde{\gamma}_{xz}=\frac{\gamma_{xz}}{k_0}=\frac{su}{u^2+v^2};\qquad \tilde{\gamma}_{yz}=\frac{\gamma_{yz}}{k_0}=\frac{sv}{u^2+v^2} \tag{3.48}$$

$$\tilde{\gamma}_{zx}=\frac{\gamma_{zx}}{k_0}=\frac{w\left(u^2+v^2-s^2\right)}{s\left(u^2+v^2\right)};\qquad \tilde{\gamma}_{zy}=\frac{\gamma_{zy}}{k_0}=\tilde{\gamma}_{zx}$$

The procedure is now complete and the node scattering matrix (3.35) can be shifted to the ports of the SCN. The scattering process occurs at the ports of the node which is

given as:

$$V_p^r = S_p V_p^i \tag{3.49}$$

where S_p is a port scattering matrix of the frequency-domain hybrid node:

$$S_p = \begin{bmatrix}
\lambda_{11}a_{ij} & \lambda_{11}d_{ij} & 0 & 0 & 0 & 0 & \lambda_{14}c_{ij} & -\lambda_{14}c_{ij} & 0 & 0 & \lambda_{16}b_{ij} & \lambda_{16}b_{ij} \\
\lambda_{11}d_{ij} & \lambda_{11}a_{ij} & 0 & 0 & 0 & 0 & -\lambda_{14}c_{ij} & \lambda_{14}c_{ij} & 0 & 0 & \lambda_{16}b_{ij} & \lambda_{16}b_{ij} \\
0 & 0 & \lambda_{22}a_{ik} & \lambda_{22}d_{ik} & \lambda_{23}b_{ik} & \lambda_{23}b_{ik} & 0 & 0 & \lambda_{25}c_{ik} & -\lambda_{25}c_{ik} & 0 & 0 \\
0 & 0 & \lambda_{22}d_{ik} & \lambda_{22}a_{ik} & \lambda_{23}b_{ik} & \lambda_{23}b_{ik} & 0 & 0 & -\lambda_{25}c_{ik} & \lambda_{25}c_{ik} & 0 & 0 \\
0 & 0 & \lambda_{23}b_{jk} & \lambda_{23}b_{jk} & \lambda_{33}a_{jk} & \lambda_{33}d_{jk} & 0 & 0 & 0 & 0 & \lambda_{36}c_{jk} & -\lambda_{36}c_{jk} \\
0 & 0 & \lambda_{23}b_{jk} & \lambda_{23}b_{jk} & \lambda_{33}d_{jk} & \lambda_{33}a_{jk} & 0 & 0 & 0 & 0 & -\lambda_{36}c_{jk} & \lambda_{36}c_{jk} \\
\lambda_{14}c_{ji} & -\lambda_{14}c_{ji} & 0 & 0 & 0 & 0 & \lambda_{44}a_{ji} & \lambda_{44}d_{ji} & \lambda_{45}b_{ji} & \lambda_{45}b_{ji} & 0 & 0 \\
-\lambda_{14}c_{ji} & \lambda_{14}c_{ji} & 0 & 0 & 0 & 0 & \lambda_{44}d_{ji} & \lambda_{44}a_{ji} & \lambda_{45}b_{ji} & \lambda_{45}b_{ji} & 0 & 0 \\
0 & 0 & \lambda_{25}c_{ki} & -\lambda_{25}c_{ki} & 0 & 0 & \lambda_{45}b_{ki} & \lambda_{45}b_{ki} & \lambda_{55}a_{ki} & \lambda_{55}d_{ki} & 0 & 0 \\
0 & 0 & -\lambda_{25}c_{ki} & \lambda_{25}c_{ki} & 0 & 0 & \lambda_{45}b & \lambda_{45}b_{ki} & \lambda_{55}d_{ki} & \lambda_{55}a_{ki} & 0 & 0 \\
\lambda_{16}b_{kj} & \lambda_{16}b_{kj} & 0 & 0 & \lambda_{36}c_{kj} & -\lambda_{36}c_{kj} & 0 & 0 & 0 & 0 & \lambda_{66}a_{kj} & \lambda_{66}d_{kj} \\
\lambda_{16}b_{kj} & \lambda_{16}b_{kj} & 0 & 0 & -\lambda_{36}c_{kj} & \lambda_{36}c_{kj} & 0 & 0 & 0 & 0 & \lambda_{66}d_{kj} & \lambda_{66}a_{kj}
\end{bmatrix} \tag{3.50}$$

where

$$\lambda_{11} = e^{-j\gamma_{xy}\cdot u} \; ; \quad \lambda_{14} = e^{-\frac{j}{2}(\gamma_{xy}\cdot u + \gamma_{yx}\cdot v)} \; ; \quad \lambda_{16} = e^{-\frac{j}{2}(\gamma_{xy}\cdot u + \gamma_{zy}\cdot w)} \; ;$$

$$\lambda_{22} = e^{-j\gamma_{xz}\cdot u} \; ; \quad \lambda_{23} = e^{-\frac{j}{2}(\gamma_{xz}\cdot u + \gamma_{yz}\cdot v)} \; ; \quad \lambda_{25} = e^{-\frac{j}{2}(\gamma_{xz}\cdot u + \gamma_{zx}\cdot w)} \; ;$$

$$\lambda_{33} = e^{-j\gamma_{yz}\cdot v} \; ; \quad \lambda_{36} = e^{-\frac{j}{2}(\gamma_{yz}\cdot v + \gamma_{zy}\cdot w)} \; ; \quad \lambda_{44} = e^{-j\gamma_{yx}\cdot v} \; ;$$

$$\lambda_{45} = e^{-\frac{j}{2}(\gamma_{yx}\cdot v + \gamma_{zx}\cdot w)} \; ; \quad \lambda_{55} = e^{-j\gamma_{zx}\cdot w} \; ; \quad \lambda_{66} = e^{-j\gamma_{zy}\cdot w} \; ;$$

and

$$a_{ij} = \frac{Y_{ij} - Y_{ji}}{2(Y_{ij} + Y_{ji})} = -d_{ij}$$

$$b_{ij} = \frac{1}{2}$$

$$c_{ij} = \frac{Y_{ji}}{Y_{ij} + Y_{ji}}$$

with $i, j, k \in \{x, y, z\}$ and $i \neq j \neq k$.

3.5 Discussion and Conclusion

In this chapter a theoretical development of a class of FDTLM symmetrical condensed nodes has been presented. The scattering matrix of the SCN is derived by using the simple and elegant empirical method proposed by Naylor and Ait-Sadi [41]. By applying the equivalent network model this empirical method has been successfully proved and a set of scattering equations of the SCN has been obtained. On the other hand, these scattering equations can also be obtained by applying the charge and magnetic flux conservation laws, which was suggested by Herring [44] and Trenkic [46, 47]. Unlike Johns [34] original derivation, the approach in [41] avoids solving a set of the non-linear simultaneous equations. By introducing a new port numbering of the SCN, the scattering matrix of the SCN can be expressed concisely in symmetrical matrix form. According to the FDTLM basic notation and the SCN constitutive relations, the characteristic impedances and the propagation constants of the link lines have been determined. Subsequently, the scattering matrix has been transferred from the nodal center to the ports leading to the different representations of the SCN in the frequency domain. The port scattering matrix describes the scattering properties of the FDTLM symmetrical condensed nodes. Dispersion is an inherent problem of all TLM nodes. The scattering matrix presented in this chapter will be used for the dispersion analysis in Chapter 5 of this thesis. It should be pointed out that the approach presented here is not the only way to derive the scattering matrix of the SCN. The FDTLM SCN can be directly derived from Maxwell's equations by using centered differencing and averaging, through which the direct correspondence between the FDTLM and the finite difference method can be established. The next chapter will focus on this topic.

Chapter 4

Development of Frequency-Domain SCN from Maxwell's Equations

4.1 Introduction

In the previous chapter, the scattering properties of the symmetrical condensed nodes in the frequency domain were described in terms of the TLM equivalent network. Another alternative is to directly relate the scattering properties of the SCN to the electromagnetic field governed by Maxwell's equations, without resorting to any equivalent circuit concepts. This chapter will present a frequency-domain TLM symmetrical condensed node derived directly from Maxwell's equations by using centered differencing and averaging [9, 48, 49]. Based on this derivation, a direct correspondence between the general FDTLM condensed node and the finite difference discretization can be established. So far, a similar equivalence has been introduced for the case of a uniform mesh 12-port SCN for modeling free space in the time domain [50]. A field theoretical derivation of the TLM method from the method of moments for the SCN was reported in the literature [36, 51, 52, 53] as well.

In this derivation, the scattering matrix of the SCN and the field expressions are given for the general case with graded mesh and anisotropic materials including both electric and magnetic losses. It will be demonstrated that the FDTLM condensed node always has 2nd-order accuracy for uniform or graded mesh discretization. Using different nodes for different media, the FDTLM method can be applied to virtually any structure with complex geometry.

4.2 Derivation of the SCN from Maxwell's Equations

4.2.1 Central Differencing of Maxwell's Equations

In the rectangular coordinate system, the time-harmonic Maxwell's equations can be written as:

$$j\omega\varepsilon_0\varepsilon_{rx}\cdot\mathcal{E}_x=\frac{\partial\mathcal{H}_z}{\partial y}-\frac{\partial\mathcal{H}_y}{\partial z}-\sigma_{ex}\mathcal{E}_x \tag{4.1a}$$

$$j\omega\varepsilon_0\varepsilon_{ry}\cdot\mathcal{E}_y=\frac{\partial\mathcal{H}_x}{\partial z}-\frac{\partial\mathcal{H}_z}{\partial x}-\sigma_{ey}\mathcal{E}_y \tag{4.1b}$$

$$j\omega\varepsilon_0\varepsilon_{rz}\cdot\mathcal{E}_z=\frac{\partial\mathcal{H}_y}{\partial x}-\frac{\partial\mathcal{H}_x}{\partial y}-\sigma_{ez}\mathcal{E}_z \tag{4.1c}$$

$$j\omega\mu_0\mu_{rx}\cdot\mathcal{H}_x=\frac{\partial\mathcal{E}_y}{\partial z}-\frac{\partial\mathcal{E}_z}{\partial y}-\sigma_{mx}\mathcal{H}_x \tag{4.1d}$$

$$j\omega\mu_0\mu_{ry}\cdot\mathcal{H}_y=\frac{\partial\mathcal{E}_z}{\partial x}-\frac{\partial\mathcal{E}_x}{\partial z}-\sigma_{my}\mathcal{H}_y \tag{4.1e}$$

$$j\omega\mu_0\mu_{rz}\cdot\mathcal{H}_z=\frac{\partial\mathcal{E}_x}{\partial y}-\frac{\partial\mathcal{E}_y}{\partial x}-\sigma_{mz}\mathcal{H}_z \tag{4.1f}$$

where ω is the radian frequency. ε_{ri} and μ_{ri} are the relative permittivity and permeability, and σ_{ei} and σ_{mi} the equivalent electric and magnetic conductivities in the i-direction, respectively.

Space is discretized and the grid points in the space are denoted by indices *(i, j, k)*, respectively, and the *x, y, z* directions, as shown in Figure 4.1. An arbitrary function of space at point *(i, j, k)* is expressed as *F(i, j, k)*. The cell sizes are denoted by *u, v, w*, respectively, along the *x, y, z* directions.

Eqs. (4.1a)-(4.1f) can be simplified by using the following transformation:

$$x = u\cdot X\,;\qquad y = v\cdot Y\,;\qquad z = w\cdot Z \tag{4.2}$$

and

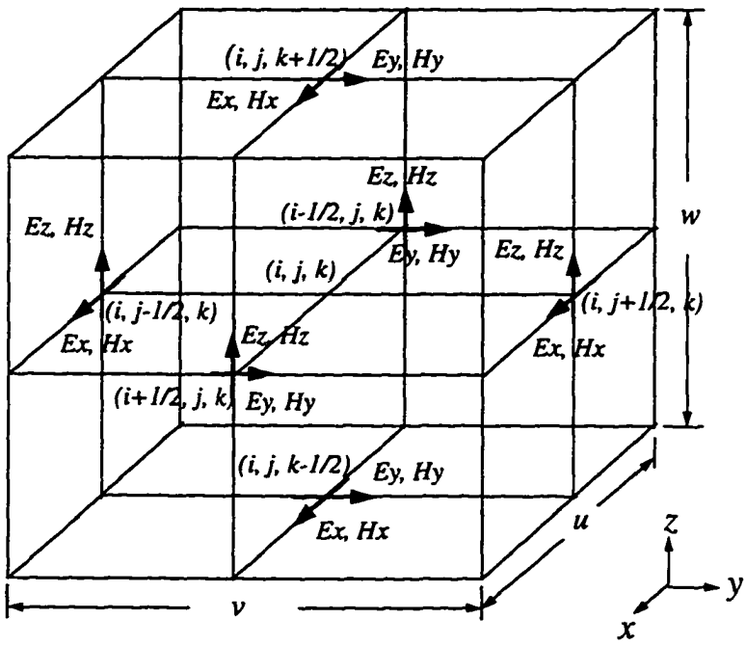

Figure 4.1 A center differencing unit cell and field sampling points.

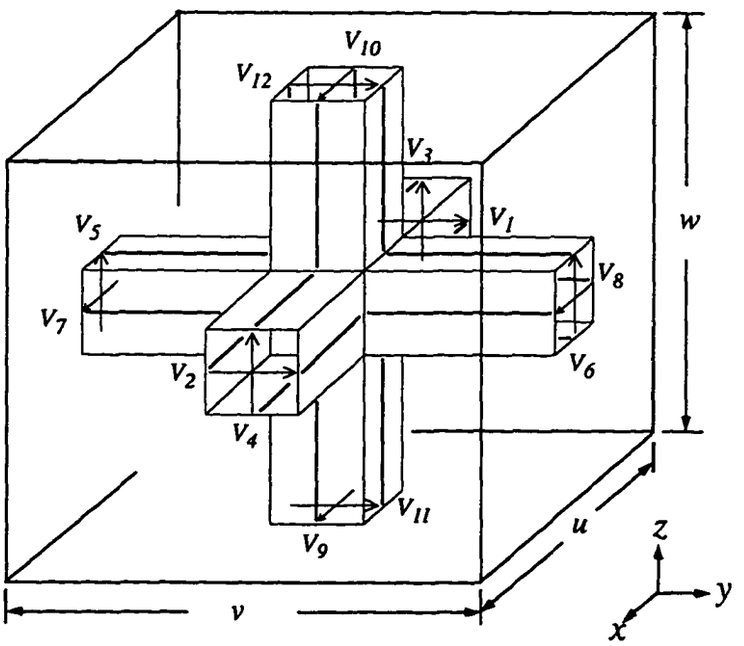

Figure 4.2 The equivalent FDTLM symmetrical condensed node.

$$\mathcal{E}_x = E_x/u \; ; \quad \mathcal{E}_y = E_y/v \; ; \quad \mathcal{E}_z = E_z/w \tag{4.3a}$$

$$\mathcal{H}_x = H_x/uZ_0 \; ; \quad \mathcal{H}_y = H_y/vZ_0 \; ; \quad \mathcal{H}_z = H_z/wZ_0 \tag{4.3b}$$

For example, Eq. (4.1a) can be written as follows:

$$\frac{\partial H_z}{\partial Y} - \frac{\partial H_y}{\partial Z} - (\sigma_{ex} \cdot Z_0 + j\omega Z_0 \varepsilon_0 \varepsilon_{rx}) \frac{v \cdot w}{u} \cdot E_x = 0$$

Eqs. (4.1a)-(4.1f)) are then rewritten as:

$$\frac{\partial H_z}{\partial Y} - \frac{\partial H_y}{\partial Z} - Y_{ex} \cdot E_x = 0 \tag{4.4a}$$

$$\frac{\partial H_x}{\partial Z} - \frac{\partial H_z}{\partial X} - Y_{ey} \cdot E_y = 0 \tag{4.4b}$$

$$\frac{\partial H_y}{\partial X} - \frac{\partial H_x}{\partial Y} - Y_{ez} \cdot E_z = 0 \tag{4.4c}$$

$$\frac{\partial E_y}{\partial Z} - \frac{\partial E_z}{\partial Y} - Z_{mx} \cdot H_x = 0 \tag{4.4d}$$

$$\frac{\partial E_z}{\partial X} - \frac{\partial E_x}{\partial Z} - Z_{my} \cdot H_y = 0 \tag{4.4e}$$

$$\frac{\partial E_x}{\partial Y} - \frac{\partial E_y}{\partial X} - Z_{mz} \cdot H_z = 0 \tag{4.4f}$$

where the normalized admittances represent the electric losses in the *x, y, z* directions defined as:

$$Y_{ex} = (\sigma_{ex} \cdot Z_0 + j\varepsilon_{rx} \cdot k_0) \cdot \frac{v \cdot w}{u} \tag{4.5a}$$

$$Y_{ey} = (\sigma_{ey} \cdot Z_0 + j\varepsilon_{ry} \cdot k_0) \cdot \frac{u \cdot w}{v} \tag{4.5b}$$

$$Y_{ez} = (\sigma_{ez} \cdot Z_0 + j\varepsilon_{rz} \cdot k_0) \cdot \frac{u \cdot v}{w} \tag{4.5c}$$

The normalized impedances for the magnetic losses in the *x, y, z* directions are defined as:

$$Z_{mx} = (\sigma_{mx} Y_0 + j\mu_{rx} \cdot k_0) \cdot \frac{v \cdot w}{u} \tag{4.6a}$$

$$Z_{my} = (\sigma_{my} Y_0 + j\mu_{ry} \cdot k_0) \cdot \frac{u \cdot w}{v} \tag{4.6b}$$

$$Z_{mz} = (\sigma_{mz} Y_0 + j\mu_{rz} \cdot k_0) \cdot \frac{u \cdot v}{w} \tag{4.6c}$$

$Z_0(=\sqrt{\mu_0/\varepsilon_0})$ is the intrinsic characteristic impedance and Y_0 is the intrinsic characteristic admittance of the propagation medium, respectively. $k_0(=\omega\sqrt{\mu_0\varepsilon_0})$ is the wave propagation constant in the same medium.

By using centered differencing at point *(i, j, k)*, a set of the finite difference equations for Maxwell's equations can be obtained from Eqs. (4.4a)-(4.4f). For example, for Eq. (4.4a), we have:

$$\left[H_z\left(i, j+\frac{1}{2}, k\right) - H_z\left(i, j-\frac{1}{2}, k\right)\right]$$

$$-\left[H_y\left(i, j, k+\frac{1}{2}\right) - H_y\left(i, j, k-\frac{1}{2}\right)\right] - Y_{ex} E_x(i, j, k) = 0 \tag{4.7}$$

Similarly for the remaining equations (4.4b)-(4.4f).

In comparison with the finite difference unit cell in Figure 4.1 and the TLM SCN in Figure 4.2, the incident and reflected voltage waves and the sampled electric and magnetic field components can be established. Subsequently, the following variable relations are introduced:

$$E_y\left(i-\frac{1}{2}, j, k\right) \pm H_z\left(i-\frac{1}{2}, j, k\right) = 2 \cdot V_1^{i,r} \tag{4.8a}$$

$$E_y\left(i+\frac{1}{2}, j, k\right) \mp H_z\left(i+\frac{1}{2}, j, k\right) = 2 \cdot V_2^{i,r} \tag{4.8b}$$

$$E_z\left(i-\frac{1}{2}, j, k\right) \mp H_y\left(i-\frac{1}{2}, j, k\right) = 2 \cdot V_3^{i,r} \tag{4.8c}$$

$$E_z\left(i+\frac{1}{2}, j, k\right) \pm H_y\left(i+\frac{1}{2}, j, k\right) = 2 \cdot V_4^{i,r} \tag{4.8d}$$

$$E_z\left(i,j-\frac{1}{2},k\right)\pm H_x\left(i,j-\frac{1}{2},k\right) = 2\cdot V_5^{i,r} \tag{4.8e}$$

$$E_z\left(i,j+\frac{1}{2},k\right)\mp H_x\left(i,j+\frac{1}{2},k\right) = 2\cdot V_6^{i,r} \tag{4.8f}$$

$$E_x\left(i,j-\frac{1}{2},k\right)\mp H_z\left(i,j-\frac{1}{2},k\right) = 2\cdot V_7^{i,r} \tag{4.8g}$$

$$E_x\left(i,j+\frac{1}{2},k\right)\pm H_z\left(i,j+\frac{1}{2},k\right) = 2\cdot V_8^{i,r} \tag{4.8h}$$

$$E_x\left(i,j,k-\frac{1}{2}\right)\pm H_y\left(i,j,k-\frac{1}{2}\right) = 2\cdot V_9^{i,r} \tag{4.8i}$$

$$E_x\left(i,j,k+\frac{1}{2}\right)\mp H_y\left(i,j,k+\frac{1}{2}\right) = 2\cdot V_{10}^{i,r} \tag{4.8j}$$

$$E_y\left(i,j,k-\frac{1}{2}\right)\mp H_x\left(i,j,k-\frac{1}{2}\right) = 2\cdot V_{11}^{i,r} \tag{4.8k}$$

$$E_y\left(i,j,k+\frac{1}{2}\right)\pm H_x\left(i,j,k+\frac{1}{2}\right) = 2\cdot V_{12}^{i,r} \tag{4.8l}$$

where the factor 2 is introduced to satisfy the finite difference equations for Eqs. (4.4a)-(4.4f) by using centered differencing. $V_m{}^i$ and $V_m{}^r$ correspond to the incident and reflected waves of the m-th link line on the right hand side of the equations, respectively. The relations (4.8a)-(4.8l) transform the normalized field components to the incident and reflected voltage waves on the link lines of the node, and establish a direct correspondence between the mathematical model of the finite difference scheme and the physical model of the frequency-domain TLM method.

By substituting Eqs. (4.8a)-(4.8l), for example, into Eq. (4.7) yields

$$V_7^r + V_8^r + V_9^r + V_{10}^r + Y_{ex}\cdot E_x(i,j,k) - V_7^i - V_8^i - V_9^i - V_{10}^i = 0 \tag{4.9}$$

4.2.2 Averaging the Field Components

The next step in the derivation is to express the field components at the central point (i, j, k) in terms of the incident voltages on the link lines of the node. This is accomplished

by averaging the electric and magnetic field components at the central point (i, j, k) along the appropriate coordinate axis. For example, for (E_y+H_z), the associated coordinate is x since the x-axis is orthogonal to both E_y and H_z. For (E_y+H_z) with respect to the x-direction, the centered average at the central point (i, j, k) can be written as:

$$\left[E_y\left(i+\frac{1}{2},j,k\right)+H_z\left(i+\frac{1}{2},j,k\right)\right]+\left[E_y\left(i-\frac{1}{2},j,k\right)+H_z\left(i-\frac{1}{2},j,k\right)\right]$$

$$-2\cdot\left[E_y\left(i,j,k\right)+H_z\left(i,j,k\right)\right]=0 \tag{4.10}$$

Substituting Eqs. (4.8a) and (4.8b) into Eq. (4.10), we have:

$$V_2^r+V_1^i-[E_y(i,j,k)+H_z(i,j,k)]=0 \tag{4.11a}$$

Similarly, the equations for the other field components at the central point can be obtained:

$$V_4^r+V_3^i-[E_z(i,j,k)-H_y(i,j,k)]=0 \tag{4.11b}$$

$$V_6^r+V_5^i-[E_z(i,j,k)+H_x(i,j,k)]=0 \tag{4.11c}$$

$$V_8^r+V_7^i-[E_x(i,j,k)-H_z(i,j,k)]=0 \tag{4.11d}$$

$$V_{10}^r+V_9^i-[E_x(i,j,k)+H_y(i,j,k)]=0 \tag{4.11e}$$

$$V_{12}^r+V_{11}^i-[E_y(i,j,k)-H_x(i,j,k)]=0 \tag{4.11f}$$

$$V_1^r+V_2^i-[E_y(i,j,k)-H_z(i,j,k)]=0 \tag{4.11g}$$

$$V_3^r+V_4^i-[E_z(i,j,k)+H_y(i,j,k)]=0 \tag{4.11h}$$

$$V_5^r+V_6^i-[E_z(i,j,k)-H_x(i,j,k)]=0 \tag{4.11i}$$

$$V_7^r+V_8^i-[E_x(i,j,k)+H_z(i,j,k)]=0 \tag{4.11j}$$

$$V_9^r+V_{10}^i-[E_x(i,j,k)-H_y(i,j,k)]=0 \tag{4.11k}$$

$$V_{11}^r+V_{12}^i-[E_y(i,j,k)+H_x(i,j,k)]=0 \tag{4.11l}$$

From Eqs. (4.9) and (4.11a)-(4.11l), the expression of the field components at the central point (i, j, k) in terms of the incident voltages, V^i_m, can be easily found. For example, adding Eq. (4.11d) to Eq. (4.11j) and Eq. (4.11e) to Eq. (4.11k), respectively, gives:

$$V^r_7 + V^r_8 = E_x(i,j,k) - \left(V^i_7 + V^i_8 \right) \tag{4.12a}$$

$$V^r_9 + V^r_{10} = E_x(i,j,k) - \left(V^i_9 + V^i_{10} \right) \tag{4.12b}$$

Then the electric field component in the x-direction, $E_x(i, j, k)$, is given by:

$$E_x(i,j,k) = \frac{2\left(V^i_7 + V^i_8 + V^i_9 + V^i_{10} \right)}{(Y_{ex} + 4)} \tag{4.13a}$$

Similarly, the expressions for the other electric and magnetic field components in terms of the incident voltages of the link lines can be readily obtained:

$$E_y(i,j,k) = \frac{2\left(V^i_1 + V^i_2 + V^i_{11} + V^i_{12} \right)}{(Y_{ey} + 4)} \tag{4.13b}$$

$$E_z(i,j,k) = \frac{2\left(V^i_3 + V^i_4 + V^i_5 + V^i_6 \right)}{(Y_{ez} + 4)} \tag{4.13c}$$

$$H_x(i,j,k) = \frac{2\left(V^i_5 - V^i_6 - V^i_{11} + V^i_{12} \right)}{(Z_{mx} + 4)} \tag{4.13d}$$

$$H_y(i,j,k) = \frac{2\left(-V^i_3 + V^i_4 + V^i_9 - V^i_{10} \right)}{(Z_{my} + 4)} \tag{4.13e}$$

$$H_z(i,j,k) = \frac{2\left(V^i_1 - V^i_2 - V^i_7 + V^i_8 \right)}{(Z_{mz} + 4)} \tag{4.13f}$$

Finally, by substituting Eqs. (4.13a)-(4.13f) into Eqs. (4.11a)-(4.11l), the scattering matrix can then be obtained in symmetrical and compact form. The same as matrix (3.25) in the previous chapter. The 12x12 scattering matrix of the SCN is shown as follows:

$$S = \begin{bmatrix}
a_{ij} & d_{ij} & 0 & 0 & 0 & 0 & c_{ij} & -c_{ij} & 0 & 0 & b_{ij} & b_{ij} \\
d_{ij} & a_{ij} & 0 & 0 & 0 & 0 & -c_{ij} & c_{ij} & 0 & 0 & b_{ij} & b_{ij} \\
0 & 0 & a_{ik} & d_{ik} & b_{ik} & b_{ik} & 0 & 0 & c_{ik} & -c_{ik} & 0 & 0 \\
0 & 0 & d_{ik} & a_{ik} & b_{ik} & b_{ik} & 0 & 0 & -c_{ik} & c_{ik} & 0 & 0 \\
0 & 0 & b_{jk} & b_{jk} & a_{jk} & d_{jk} & 0 & 0 & 0 & 0 & c_{jk} & -c_{jk} \\
0 & 0 & b_{jk} & b_{jk} & d_{jk} & a_{jk} & 0 & 0 & 0 & 0 & -c_{jk} & c_{jk} \\
c_{ji} & -c_{ji} & 0 & 0 & 0 & 0 & a_{ji} & d_{ji} & b_{ji} & b_{ji} & 0 & 0 \\
-c_{ji} & c_{ji} & 0 & 0 & 0 & 0 & d_{ji} & a_{ji} & b_{ji} & b_{ji} & 0 & 0 \\
0 & 0 & c_{ki} & -c_{ki} & 0 & 0 & b_{ki} & b_{ki} & a_{ki} & d_{ki} & 0 & 0 \\
0 & 0 & -c_{ki} & c_{ki} & 0 & 0 & b_{ki} & b_{ki} & d_{ki} & a_{ki} & 0 & 0 \\
b_{kj} & b_{kj} & 0 & 0 & c_{kj} & -c_{kj} & 0 & 0 & 0 & 0 & a_{kj} & d_{kj} \\
b_{kj} & b_{kj} & 0 & 0 & -c_{kj} & c_{kj} & 0 & 0 & 0 & 0 & d_{kj} & a_{kj}
\end{bmatrix} \tag{4.14}$$

where the matrix elements, in terms of the normalized electric and magnetic losses defined as (4.5a)-(4.5c) and (4.6a)-(4.6c), are given in the general form with the dummy indices, i, j, $k \in \{x, y, z\}$ with all possible combinations, except $i = j = k$.

$$a_{ij} = -\frac{Y_{ej}}{2(4 + Y_{ej})} + \frac{Z_{mk}}{2(4 + Z_{mk})} \tag{4.15a}$$

$$b_{ij} = \frac{2}{4 + Y_{ej}} \tag{4.15b}$$

$$c_{ij} = \frac{2}{4 + Z_{mk}} \tag{4.15c}$$

$$d_{ij} = -\frac{Y_{ej}}{2(4 + Y_{ej})} - \frac{Z_{mk}}{2(4 + Z_{mk})} \tag{4.15d}$$

4.3 Consistency with the SCN Equivalent Network Representations

4.3.1 Modeling of Electric and Magnetic Losses

Generally, in the frequency-domain TLM, the electric and magnetic losses are directly incorporated to the FDTLM constitutive relations by using complex permittivity and permeability defined as:

$$\varepsilon_i = \varepsilon'_i - j\varepsilon''_i = \varepsilon'_i - j\frac{\sigma_{ei}}{\omega} \tag{4.16}$$

$$\mu_i = \mu'_i - j\mu''_i = \mu'_i - j\frac{\sigma_{mi}}{\omega} \tag{4.17}$$

That means that the losses can be modeled directly by assuming lossy link lines. Hence, the capacitances and inductances of each link line are complex. The imaginary part of the capacitances and inductances represent the distributed shunt and series losses of the link line which are corresponding to the electric and magnetic losses of the medium. This is the case we developed for the frequency-domain SCN in Chapter 3.

On the other hand, in a frequency-domain TLM node the electric and magnetic losses can be considered by introducing shunt and series stubs into the scattering center. Both lossy stubs can be treated as either infinity long or terminated (matched) with their own impedance. The incident waves scattered into the stub are absorbed by the system and there are no waves reflected back. This kind of stub is known as matched stub in the TLM terms. In general, the matched stubs are used to model both electric and magnetic losses. The shunt conductance G_e models the electric conductivity σ_e and the series resistance R_m models the 'magnetic conductivity' σ_m. Physically, the lossy element in the network is to model of the energy dissipation. For example, the required normalized lossy shunt conductance for a stub in the y-direction is defined as [54, 55, 44, 47]:

$$G_{ey} = \sigma_{ey} Z_0 \frac{uw}{v} = \sigma_{ey} Z_0 \frac{\Delta x \Delta z}{\Delta y} \tag{4.18}$$

Similarly, in terms of the required normalized lossy series resistance, the magnetic loss for a stub in the y-direction is defined as:

$$R_{my} = \sigma_{my} Y_0 \frac{uw}{v} = \sigma_{my} Y_0 \frac{\Delta x \Delta z}{\Delta y} \tag{4.19}$$

where Z_0 is the intrinsic characteristic impedance and Y_0 is the intrinsic characteristic admittance of the propagation medium, respectively. An alternative definition, which includes the electric conductivity σ_e, the 'magnetic conductivity' σ_m, the permittivity and the permeability, has been given in the previous section. The normalized admittance and impedance for a Cartesian mesh is written as:

$$Y_{ei} = (\sigma_{ei} \cdot Z_0 + j\varepsilon_{ri} \cdot k_0) \cdot \frac{u \cdot w}{v} \tag{4.20}$$

$$Z_{mi} = (\sigma_{mi} Y_0 + j\mu_{ri} \cdot k_0) \cdot \frac{u \cdot w}{v} \tag{4.21}$$

where $i = x$, y, or z. From the TLM network perspective this definition incorporates all link lines parameters. Hence, the FDTLM constitutive equations used to determine the parameters of the link lines will be not affected by the introduction of the lossy matched stubs. At the same time, the SCN exhibits the same impedance on all its link lines, which is the intrinsic characteristic impedance or the intrinsic characteristic admittance of the background medium. This approach is consistent with the original TLM scheme [32, 34]. In addition, it gives us more freedom to model anisotropic materials with local electric and magnetic parameters and a graded mesh SCN with arbitrary aspect ratio.

4.3.2 Lossy Stub-load SCN

From the point of view of the equivalent network model presented in Chapter 3, the scattering properties derived in the previous section can also be considered as the incident voltage waves scattered from an SCN with lossy stub-load. Hence, the scattering process is not affected by these lossy stubs. This physical concept provide us a simple way to derive the scattering matrix (4.14) obtained in Section 4.2 by using equivalent network modeling. Figure 4.3 shows one set of the equivalent shunt and series nodes with

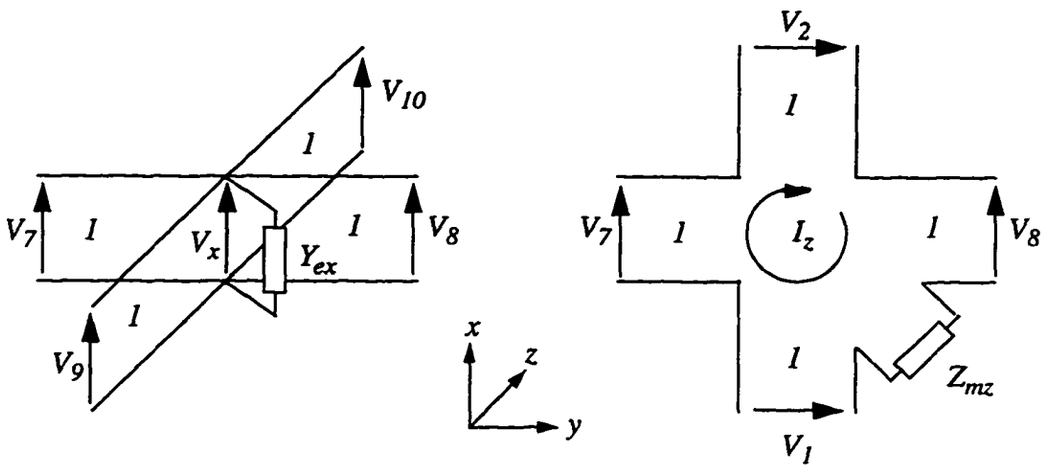

(a) shunt node with lossy admittance *(b) series node with lossy impedance*

Figure 4.3 Lossy stub-loaded symmetrical condensed node circuit representation with the same normalized characteristic impedance on each link line.

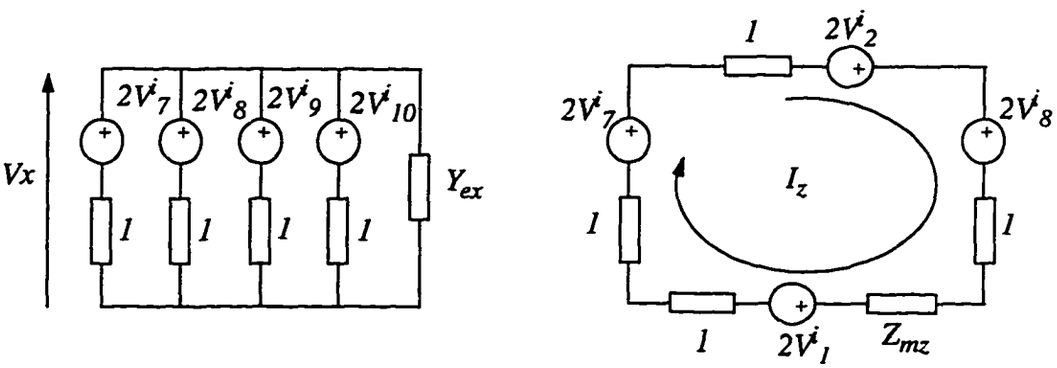

(a) Equivalent Thevenin shunt circuit *(b) Equivalent Thevenin series circuit*

Figure 4.4 Equivalent Thevenin circuit for the lossy stub-loaded symmetrical condensed node.

a lossy stub. According to Eqs. (3.11) and (3.12) in Chapter 3, the general scattering equations for the voltages V_7 and V_8 can be written as:

$$V_7^r = V_x + I_z - V_8^i \tag{4.22}$$

$$V_8^r = V_x - I_z - V_7^i \tag{4.23}$$

The nodal voltage and the loop current can be easily obtained by applying the Thevenin equivalent circuit to the shunt and series node representation, as shown in Figure 4.4, which are given as:

$$V_x = \frac{2\left(V_7^i + V_8^i + V_9^i + V_{10}^i\right)}{4 + Y_{ex}} \tag{4.24a}$$

$$I_z = \frac{2\left(V_7^i - V_8^i - V_1^i + V_2^i\right)}{4 + Z_{mz}} \tag{4.24b}$$

Comparing the above two equations with Eqs. (4.13a) and (4.13f), which have been derived directly from Maxwell's equation, it can be seen that both expressions are identical. The equivalency between the electric and magnetic fields and the voltages and currents on each pair of link lines yields

$$E_x = V_x = \mathcal{E}_x \cdot u \tag{4.25a}$$

$$H_z = -I_z = \mathcal{H}_z \cdot w \tag{4.25b}$$

By substituting the expressions for V_x (Eq. (4.24a)) and I_z (Eq. (4.24b)) into the general scattering equations (4.22) and (4.23) and then grouping terms, the elements of the scattering matrix on rows 7 and 8 are obtained readily. The matrix elements for the other rows can also be found by adopting a similar procedure. In this way the complete scattering matrix is found the same format as the matrix in Eq. (4.14). The associated matrix elements are given as the expressions of Eqs. (4.15a)-(4.15d) in Section 4.2.2.

For more general cases, the concept of the normalized shunt conductance and series resistance is applied to model only the electric and magnetic lossy properties of the

medium, which are given in Eqs. (4.18) and (4.19). In this way, the characteristic impedances or admittances of the link lines can be chosen freely, which are associated with the permittivity and permeability of the propagation medium and graded mesh parameters. The scattering properties for the lossy stub-loaded node can be easily derived from the general scattering equations (3.24) and (3.25) in Chapter 3. By assuming $Z_{-ij} = Z_{ij}$, one set of the equivalent shunt node with lossy conductance and series nodes with lossy conductance and resistance is sketched in Figure 4.3. In this case the general equations can be found as:

$$V^r_{-xy} = V_y + I_z Z_{xy} - V^i_{+xy} \tag{4.26a}$$

$$V^r_{+xy} = V_y - I_z Z_{xy} - V^i_{-xy} \tag{4.26b}$$

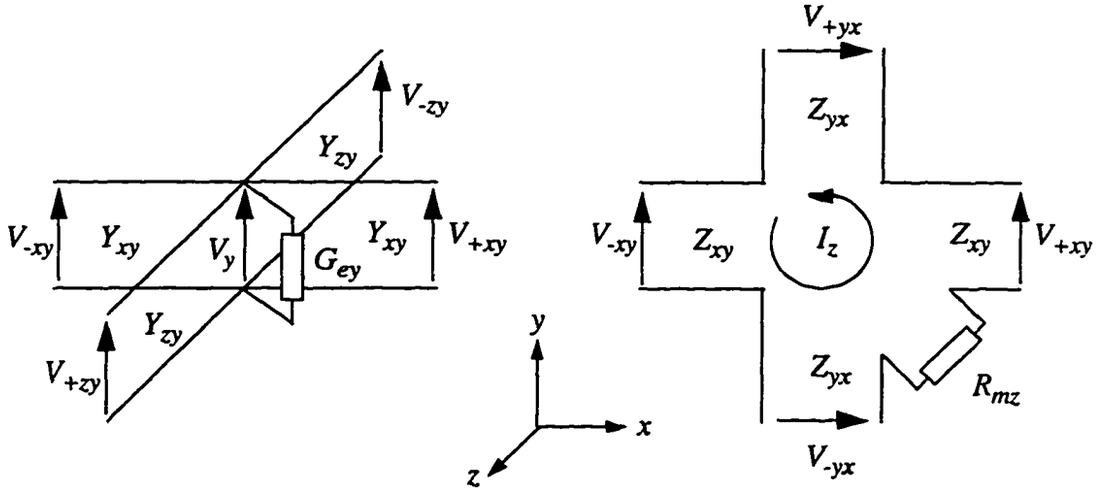

(a) shunt node with lossy conductance *(b) series node with lossy resistance*

Figure 4.5 The lossy stub-loaded symmetrical condensed node circuit representation with different characteristic impedances (or admittances) on each pair of link lines.

Then, by applying the Thevenin equivalent circuit to the lossy stub-loaded shunt and series node representation in Figure 4.3, the nodal voltage in the *y*-direction can be expressed in terms of the incident voltages and the admittances of the corresponding link lines:

$$V_y = 2\frac{Y_{xy}\cdot\left(V^i_{-xy}+V^i_{+xy}\right)+Y_{zy}\cdot\left(V^i_{-zy}+V^i_{+zy}\right)}{2Y_{xy}+2Y_{zy}+G_{ey}} \tag{4.27}$$

whereas the loop current contributing to the magnetic field in the *z*-direction is found as:

$$I_z = 2\frac{-V^i_{-xy}+V^i_{+xy}-V^i_{+yx}+V^i_{-yx}}{2Z_{xy}+2Z_{yx}+R_{mz}} \tag{4.28}$$

Therefore, for the general lossy stub-loaded (GLSL) symmetrical condensed node with the different characteristic impedances on each link line, we can easily derive the scattering equation for the reflected voltage V^r_{-xy} which is common to both circuit representations in Figure 4.3:

$$\begin{aligned} V^r_{-xy} = &-\frac{2Y_{zy}+G_{ey}}{2\left(2Y_{xy}+2Y_{zy}+G_{ey}\right)}\left(V^i_{-xy}+V^i_{+xy}\right) \\ &+\frac{2Z_{yx}+R_{mz}}{2\left(2Z_{xy}+2Z_{yx}+R_{mz}\right)}\left(V^i_{-xy}-V^i_{+xy}\right) \\ &+\frac{2Z_{xy}}{2Z_{xy}+2Z_{yx}+R_{mz}}\left(V^i_{-yx}-V^i_{+yx}\right)+\frac{2Y_{zy}}{2Y_{xy}+2Y_{zy}+G_{ey}}\left(V^i_{-zy}-V^i_{+zy}\right) \end{aligned} \tag{4.29}$$

By introducing the dummy indices *i, j, k*, the nodal voltages and the loop currents can be rewritten with respect to the *x, y, z* directions, respectively:

$$V_j = 2\frac{Y_{ij}\left(V^i_{-ij}+V^i_{+ij}\right)+Y_{kj}\left(V^i_{-kj}+V^i_{+kj}\right)}{2Y_{ij}+2Y_{kj}+G_{ej}} \tag{4.30}$$

$$I_k = 2\frac{V^i_{+ij}-V^i_{-ij}+V^i_{-ji}-V^i_{+ji}}{2Z_{ij}+2Z_{ji}+R_{mk}} \tag{4.31}$$

Further, by adopting a similar procedure, the other sets of voltages and currents the for the GLSL SCN are then completely described by the scattering equations from Eqs. (3.24) and (3.25) in Chapter 3. The voltages and currents are corresponding to their shunt and series circuits, respectively. Finally, the complete scattering matrix for the GLSL symmetrical condensed node is represented with the same matrix form shown as (4.14). The corresponding elements of the scattering matrix S are readily given as:

$$a_{ij} = -\frac{2Y_{kj} + G_{ej}}{2(2Y_{ij} + 2Y_{kj} + G_{ej})} + \frac{2Z_{ji} + R_{mk}}{2(2Z_{ij} + 2Z_{ji} + R_{mk})} \tag{4.32a}$$

$$b_{ij} = \frac{2Y_{kj}}{2Y_{ij} + 2Y_{kj} + G_{ej}} \tag{4.32b}$$

$$c_{ij} = \frac{2Z_{ij}}{2Z_{ij} + 2Z_{ji} + R_{mk}} \tag{4.32c}$$

$$d_{ij} = -\frac{2Y_{kj} + G_{ej}}{2(2Y_{ij} + 2Y_{kj} + G_{ej})} - \frac{2Z_{ji} + R_{mk}}{2(2Z_{ij} + 2Z_{ji} + R_{mk})} \tag{4.32d}$$

where the dummy indices $i, j, k \in \{x, y, z\}$ with all possible combinations, except $i = j = k$. This 12x12 scattering matrix (4.14) represent the scattering center, *i.e.* the node's center. As mentioned in Chapter 3, the scattering matrix at the ports of the node can be obtained by shifting the reference planes from the node's center to the ports of the twelve link lines.

4.4 Discussion and Conclusion

Historically, Huygens principle [56] forms the basis for the TLM method while finite difference-based methods are based on Maxwell's equations. Huygens principle and Maxwell's equations represent two distinct modeling philosophies. However, as shown this assumption is not justified since both principles describe the same phenomenon in nature despite the use of different concepts. A full equivalence between the TLM method and the symmetrical condensed node as well as the finite difference

method based on Maxwell's equations has been established through the derivation presented in this chapter. By comparing the derivation in Section 4.2 and Section 4.3, it is obvious that the TLM method, both in time and frequency domain, can be considered as either a physical model of the transmission line network (based on Huygens principle) or a mathematical model of the finite difference method (based on Maxwells equations), depending on which concept one feels more comfortable with [9, 48].

Based on the derivation presented in this chapter, the accuracy of the FDTLM method can be easily assessed. The errors introduced during the derivation of the field expressions (4.13) and the node scattering matrix S given in Eq. (4.14) are only associated with the centered differencing (Eq. (4.10)) and averaging which is consistent with Eqs. (4.24) based on the equivalent network modeling. Both of them have the 2nd-order accuracy. Since the derivation was carried out for a general graded mesh, it can be concluded that the 2nd-order accuracy of the FDTLM method is preserved even in the case of a graded mesh SCN.

On the other hand, from the equivalent network modeling perspective, the lossy stub-loaded (LSL) SCN is a transmission line model for the central differencing and averaging of the time-harmonic Maxwell's equations. The physical concepts of the normalized admittances and impedances, *i.e.* Eqs. (4.20) and (4.21), were introduced to represent not only the electric and magnetic losses but also the permittivity and permeability of the medium. Naturally, this brings us to the general lossy stub-loaded (GLSL) symmetrical condensed node in the frequency domain by means of the general definition of the normalized lossy shunt conductances and lossy series resistances in the circuit representation of the node. It should be noted that this idea was proposed for the first time in this thesis. The full equivalence between the FDTLM SCN and Maxwell's equations provides a rigorous theoretical foundation to all the nodes contained in the formulation of the SCN. Furthermore, it provides a way to develope new SCNs in both the frequency and time domain TLM, which has not been explored yet. These new nodes could potentially improve the efficiency and the propagation errors of the TLM method.

The propagation characteristics of the various FDTLM nodes will be a main topic in the following chapter.

Chapter 5

Propagation Characteristics of the Frequency-Domain SCNs

5.1 Introduction

In the previous chapters, it has been demonstrated that the FDTLM scheme can be described as scattering procedure of the symmetrical condensed node (SCN) directly in frequency domain. The main characteristics of the frequency-domain SCNs is that it can model inhomogeneous media with an arbitrarily graded mesh by modifying the propagation constants of the link lines of the node without using stubs. The dispersion errors of the frequency-domain nodes are also lower than those of the time-domain nodes. It is well known that the dispersion errors are present if a spatial discretization scheme is used to model electromagnetic field problems. In order to quantify the dispersion error of the FDTLM scheme and at the same time evaluate the accuracy of the method, the dispersion relation of the SCN mesh must be known. In addition to the dispersion errors, there are also error due to the spurious modes of the symmetrical condensed node, because this mode does not model the electromagnetic fields in a physical manner. This phenomenon can be explained by the fact that the symmetrical condensed node describes the electromagnetic field at the same nodal point. It is not the natural behavior of the electromagnetic field because the electric field and magnetic field can be generated alternatively in space.

The original analysis of the dispersion characteristics of the TLM SCN can be found in a series of publications beginning with Nielsen and Hoefer [57, 58, 59]. The dispersion

analysis of a TLM mesh is based on the application of Floquet's theorem [60] to an infinite three-dimensional SCN mesh. The general dispersion relation of the frequency-domain and time-domain TLM was formulated for the 12-port symmetrical condensed node. This relation is presented by an implicit eigen-matrix equation, which characterizes the desired dispersion relationship. The solution of this eigen-matrix equation for the associated eigenvectors present the field structure of each supporting eigenmode in the TLM mesh [59, 61].

The previous discussion made clear that the dispersion relation of the discretized TLM mesh plays an important role to evaluate the accuracy and efficiency of the available FDTLM SCN schemes applied to a particular guiding wave problem such as a semiconductor laser or a semiconductor-based inhomogeneously doped coplanar MIS slow-wave structures, which will be analyzed in the next chapter. In this chapter, we present the complete dispersion characteristics of a class of frequency-domain symmetrical condensed TLM nodes, as well as the lossy stub-loaded (LSL) nodes, based on the numerical solution of the eigenvalue equation. This equation is actually an implicit function of the propagation constant, k_0, of the travelling wave in the network and the mesh propagation constant, k_x, k_y and k_z, along the x, y and z directions.

5.2 General Dispersion Relation for Frequency-Domain TLM Nodes

By considering the total port voltages of an SCN in an infinite 3D mesh and the voltages of its six surrounding adjacent nodes, a general dispersion relation for the FDTLM SCN can be expressed in the form [57, 61, 62]:

$$det(I - TPS) = 0 \tag{5.1}$$

which corresponds to the eigenvector equation based on the incident voltage vector V_c^i, given as:

$$(I - TPS)\, V_c^i = 0 \tag{5.2}$$

By using the relation between the total voltage vector V_c and the incident voltage vector V_c^i which is given as [62]

$$V_c = (I+S)\,V_c^i \tag{5.3}$$

The total voltage eigenvector V_c can be determined, which is necessary for determining the field distribution of each supporting eigenmode in the TLM mesh. Where, I is a 12×12 identity matrix; S is the scattering matrix of the SCN at the center of the node either for the frequency-domain or the time-domain; and P is a matrix which contains the mesh propagation constants. For the symmetrical condensed FDTLM node shown in Figure 3.1, the elements of matrix P are zero except for:

$$P_{1,2} = P_{3,4} = e^{jk_x\Delta x} = e^{jk_x u} \tag{5.4a}$$

$$P_{5,6} = P_{7,8} = e^{jk_y\Delta y} = e^{jk_y v} \tag{5.4b}$$

$$P_{9,10} = P_{11,12} = e^{jk_z\Delta z} = e^{jk_z w} \tag{5.4c}$$

$$P_{4,3} = P_{2,1} = e^{-jk_x\Delta x} = e^{-jk_x u} \tag{5.4d}$$

$$P_{8,7} = P_{6,5} = e^{-jk_y\Delta y} = e^{-jk_y v} \tag{5.4e}$$

$$P_{10,9} = P_{12,11} = e^{-jk_z\Delta z} = e^{-jk_z w} \tag{5.4f}$$

T is a diagonal matrix which contains the propagation constants along the link lines of the SCN:

$$T_{1,1} = T_{2,2} = e^{-j\gamma_{xy}\Delta x} = e^{-j\gamma_{xy}u} \tag{5.5a}$$

$$T_{3,3} = T_{4,4} = e^{-j\gamma_{xz}\Delta x} = e^{-j\gamma_{xz}u} \tag{5.5b}$$

$$T_{5,5} = T_{6,6} = e^{-j\gamma_{yz}\Delta y} = e^{-j\gamma_{yz}v} \tag{5.5c}$$

$$T_{7,7} = T_{8,8} = e^{-j\gamma_{yx}\Delta y} = e^{-jxv} \tag{5.5d}$$

$$T_{9,9} = T_{10,10} = e^{-j\gamma_{zx}\Delta z} = e^{-j\gamma_{zx}w} \tag{5.5e}$$

$$T_{11,11} = T_{12,12} = e^{-j\gamma_{zy}\Delta z} = e^{-j\gamma_{zy}w} \tag{5.5f}$$

where the propagation constant of the link lines of the node, γ_{ij}, are calculated using the expressions given in Section 3.4.2 For example, for the hybrid node with series and shunt decomposition, the propagation constants of the corresponding link lines are derived as Eqs. (3.46) and (3.48).

An alternative general dispersion relation for the FDTLM scheme in terms of the port scattering matrix, S_p, can be expressed as [38, 39]:

$$det\,(I - PS_p) = 0 \tag{5.6}$$

where S_p is the scattering matrix of the frequency-domain TLM nodes related to the ports of the twelve link lines. In this expression the link line propagation matrix T no longer exists because the matrix elements are absorbed into the scattering matrix to give S_p at the ports of the node. This relation can be directly derived from the eigenvector equation (5.2) by multiplying the T matrix which is a diagonal matrix containing the propagation constant of the link lines with matrix S to yield S_p. This is achieved by introducing matrix $T_{1/2}$ as $T=T_{1/2}T_{1/2}$. Then, equation (5.2) can be rewritten by multiplying both side of this equation with $T^{-1}_{1/2}$ on the left sid and $T_{1/2}$ on the right side, which gives:

$$\left(T^{-1}_{1/2}T_{1/2} - T^{-1}_{1/2}T_{1/2}T_{1/2}PT^{-1}_{1/2}T_{1/2}ST_{1/2}\right)V^i_c = 0$$

Since $T_{1/2}$ is also a diagonal matrix, the following relations are satisfied:

$$I = T^{-1}_{1/2}T_{1/2}$$

$$P = T_{1/2}PT^{-1}_{1/2}$$

$$S_p = T_{1/2}ST_{1/2} \tag{5.7}$$

where the physical meaning of Eq. (5.7) is that of shifting the reference planes for the

nodal center to the ports of the 12 link lines of the SCN. The phase of the diagonal element of the S_p matrix is shifted by twice the electrical length of the shift at the port's planes of the link lines, because the voltage wave travels over this length upon incidence and reflection. Finally, combining all the above equations yields

$$(I - PS_p)\, V_c^i = 0 \tag{5.8}$$

from which the required eigenvalue equation Eq. (5.6) is therefore derived. The eigenvalue equation is also an implicit function of k_x, k_y, k_z and k_0 which results in the desired general dispersion equation. In addition, the relation (5.6) is also a function of the mesh grading and material properties. Therefore, nodes with different scattering matrices will have different dispersion characteristics and hence different numerical properties. Furthermore, to obtain the dispersion relation, a MATLAB program is developed to generate the numerical solution for the dispersion characteristics of the various frequency domain SCNs presented in this thesis.

5.3 Dispersion Analysis of the Condensed FDTLM Node

5.3.1 Accuracy Assessment of a Class of Frequency Domain Nodes

To verify the validity and accuracy of a class of FDTLM nodes, the propagation characteristics of a suspended stripline are investigated and the results are shown in Figure 5.1. for the different FDTLM nodes. This is a typical two-dimensional (2D) problem. Due the structure with sharp conner of metallic strip, the second order accuracy of the FDTLM node is degraded into the first order accuracy. However, the 2D eigenvalue results of this suspended stripline structure still illustrate the accuracy assessment of the different FDTLM nodes. The number of nodes along the x-axis is chosen as 8 and along the y-axis as 7. A graded mesh arrangement is used. Compared with the characteristic admittance node and the propagation constant node, it can be seen that the results from the frequency-domain hybrid node converge better to the results of the spectral domain approach (SDA) [37]. This is due to the fact that the coarseness error clearly appears in the case of all the nodes. For the hybrid node the coarseness error is minimum. The coarseness error can be

further reduced by refining the mesh discretization, especially in the sharp metallic strip conner, where the field changes rapidly. For example, Figure 5.1 also shows results from a refined mesh discretization, *i. e.* a 10 by 10 graded mesh. It is evident that the results are close to the SDA results.

5.3.2 Dispersion in a Class of Frequency Domain Nodes

The dispersion relations of the FDTLM nodes can be obtained from the general dispersion equation (5.6). Figure 5.2 illustrates the relative dispersion errors of the propagation constant node and characteristic admittance node compared with those of the hybrid node for a plane wave propagating in the *y*-*z* plane. The horizontal axis in Figure 5.2 represents the angle between the propagation vector and the *z*-direction as $\theta = arctan(k_y/k_z)$. The vertical axis represents the relative propagation error given as

$$\delta k = \frac{(|k| - k_m)}{k_m} \times 100 \tag{5.9}$$

where $|k|$ is as $|k| = (k_y^2 + k_z^2)^{1/2}$ and k_m is the propagation constant of the medium, and $k_m = k_0(\varepsilon_r\mu_r)^{1/2}$. The factor $k_m d$ is directly proportional to the node spacing per wavelength d/λ as:

$$k_m d = 2\pi\frac{d}{\lambda} \tag{5.10}$$

For the benchmark test of the TLM meshes we operate at the frequencies for which the wavelength falls into 10 TLM nodes, hence for cases where $d/\lambda \leq 0.1$ and therefore $k_m d \leq 0.2\pi$. The results are given for a graded mesh where $k_m u = k_m v = 0.1\pi$, $k_m w = 0.2\pi$ and $\varepsilon_r = \mu_r = 1$. It can be clearly seen from Figure 5.2 that the relative dispersion error for the frequency-domain hybrid node is always positive and much less than those of the other nodes. This result clearly suggests that the wave propagation error of the FDTLM nodes can be reduced to minimum if the mesh size is kept less than 1/10 of the wavelength in the propagation medium.

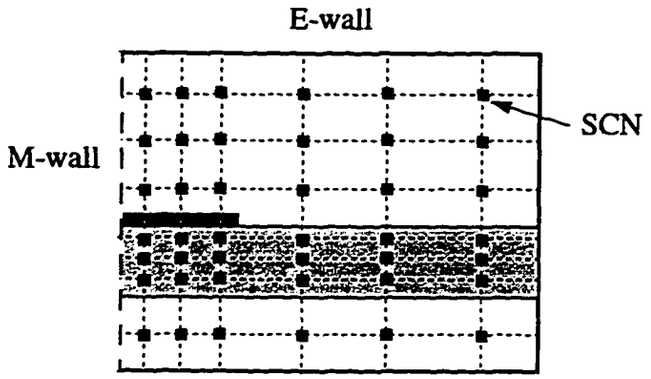

(a)

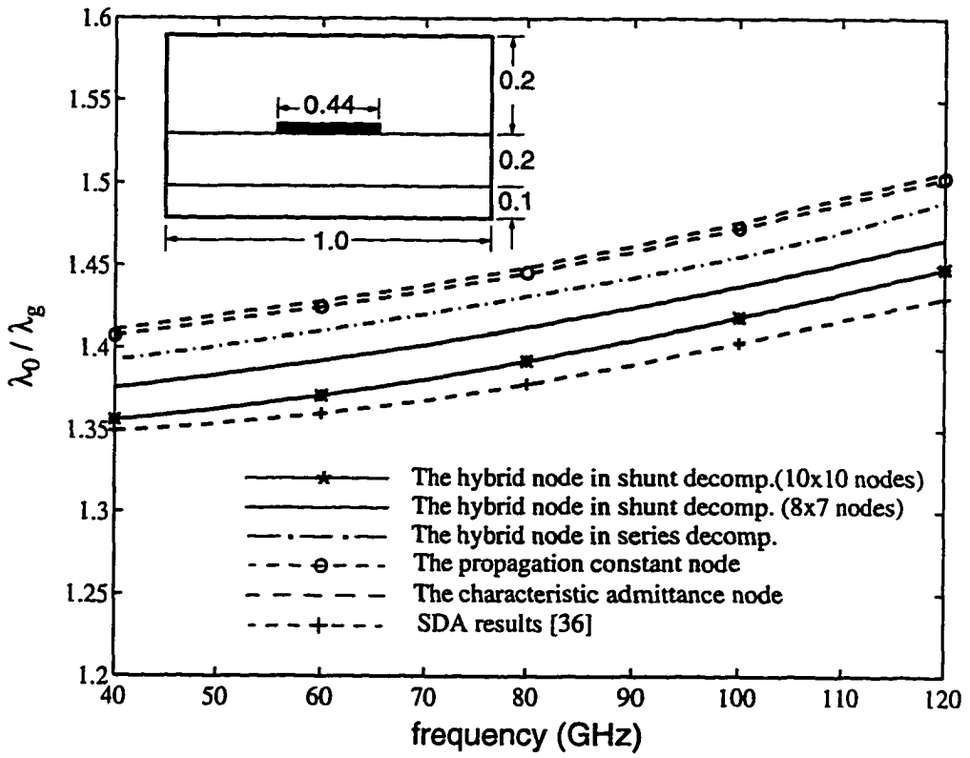

(b)

Figure 5.1 (a) The nodes arrangement of the TLM symmetrical condensed node with graded mesh. (b) Comparison of the propagation characteristics of a suspended stripline obtained with different frequency-domain SCNs.

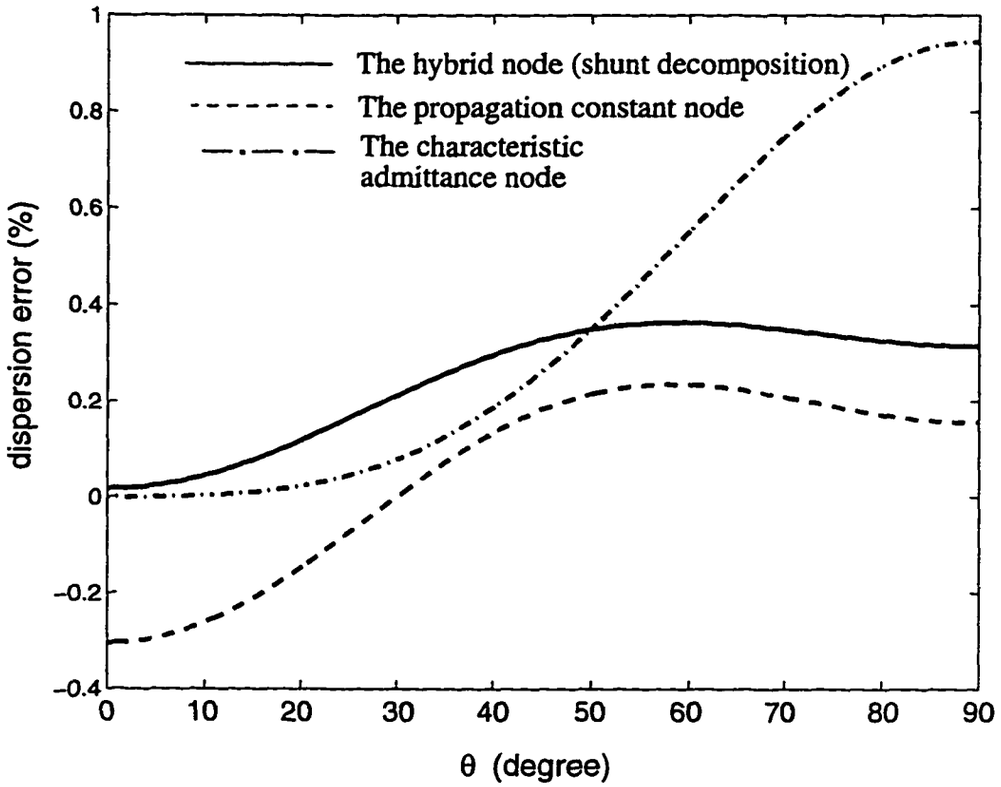

Figure 5.2 Comparison the relative dispersion errors of the different graded FDTLM nodes in y-z propagation plane (free space). $k_m u = k_m v = 0.1\pi$, $k_m w = 0.2\pi$ and $\varepsilon_r = \mu_r = 1$, where k_m is the free space propagation constant.

In the next example, we investigate the dispersion effect in a dielectric medium, also utilizing a graded mesh. Figure 5.3 illustrates a family of curves representing plane wave propagating in the y-z propagation plane. The permittivity of the dielectric medium is chosen as $\varepsilon_r = 12$. The locus of the normalized propagation vector is plotted in a polar representation for the propagation constant node and the characteristic admittance node (Figure 5.3 (a)). The shunt and series decomposition nodes are not shown, because their dispersion is very close to the unit circle. The vector k_m describes the unit circle for the infinitesimal mesh case, indicating no dispersion occurs for the FDTLM nodes at the frequencies, even for a graded mesh. When a coarse discretization is selected, for example $k_m u = k_m v = 0.05\pi$, $k_m w = 0.1\pi$, the wavelength can not be considered very large compared

to the graded cell, and the phase velocity becomes frequency dispersive, depending on the propagation direction. The maximum dispersion occurs in the axial direction for the characteristic admittance node. In this example the parameter w is larger than v and the dispersion depends on the node's dimension along the propagation directions. Thus, the dispersion is higher in the z-direction. A comparison of the relative dispersion errors in the different graded FDTLM nodes in the y-z propagation plane is shown in Figure 5.3 (b). Comparing with the different FDTLM nodes, it is found that the highest dispersion occurs in the characteristic admittance node. The dispersion error is smaller for the hybrid node than for both the propagation constant node and the characteristic admittance node, for all angles of propagation in the y-z plane. This better accuracy and low propagation error in a dielectric medium for the hybrid node compared to the other nodes may be due to the fact that the choice of three characteristic admittances of the link lines takes into account the corresponding capacitance of the link line for hybrid shunt node and the corresponding inductances of the link line for hybrid series node. The dispersion analysis is also consistent with the results shown in Figure 5.1.

5.3.3 Dispersion in the Lossy Stub-Loaded Frequency Domain Node

Figure 5.4 (a) shows the locus of the normalized propagation vector in the y-z plane and Figure 5.4 (b) illustrates the relative dispersion errors for a plane wave propagating in the y-z plane on a regular FDTLM lossy stub-loaded (LSL) node with different mesh sizes. The $k_o d = 0$ curve is identical to the exact solution of the plane wave in free space (a unit circle in the y-z plane), indicating there is no dispersion for the LSL node when the computation domain is discretized with an infinitely fine mesh. With the mesh size increased ($k_o d$ =0.2, 0.35, 0.5), the TLM mesh appears dispersive (Figure 5.4 (a)). This is contrary to the results of the time-domain TLM nodes and the other frequency-domain nodes for which the dispersion curves tend to expand outward from the origin with increasing frequencies. In the case of $k_o d = 0.5$, which corresponds to about 12 nodes per wavelength, the maximum deviation of the dispersion curve from an ideal circle is less than 2% in Figure 5.4 (b). This clearly suggests that the dispersion effect of the LSL FDTLM node may be neglected keeping the ratio of the mesh size to the wavelength under 10%.

In the next dispersion analysis, we investigate the effect of the graded mesh on the dispersion of the LSL FDTLM node. Figure 5.5 (a) shows the locus of the normalized propagation vector in the y-z plane and Figure 5.5 (b) illustrates the relative dispersion errors for a plane wave propagating in the y-z plane on a graded FDTLM mesh. The ratio of the maximum to minimum node dimensions is 5. Again here the ideal unit circle represents the curve of $k_o d = 0$, indicating there is no dispersion for the LSL node for an infinitely fine mesh. The curve corresponding to $k_0u = k_0w = 0.2, 0.35, 0.5, k_0v = 0.2$ appears elliptical with a maximum deviation at the k_z axis and a minimum at the k_y axis. This is because the points at the k_z and k_y axes correspond to waves propagating along the z- and y-axes, respectively, and their dispersions solely depend on the node dimensions along their propagation directions. Therefore, the waves propagating along the z- and y-axes experience, respectively, maximum and minimum dispersions as the node has the maximum and minimum dimensions along those axes. For waves propagating along the other directions in the y-z plane, the dispersion depends on the node dimensions along both the y- and z-axes. The maximum deviation which occurs at the k_z-axis in Figure 5.5 (b) is the same (~2%) as that in Figure 5.4, and is solely determined by the node dimensions along the z-axis. This is one of the advantages of this FDTLM node compared to other nodes in the previous section in which dispersion usually deteriorates with the mesh grading.

Figure 5.6 (a) and (b) illustrate the locus of the normalized propagation vector and its relative dispersion errors for a regular FDTLM mesh with $k_0u=k_0v=k_0w=0.2$, but with $\varepsilon_x=\varepsilon_y=\varepsilon_z=5$, 10 and 20, and $\mu_x=\mu_y=\mu_z=1$, respectively. k_m is now the propagation constant of the wave propagating in the medium. As expected, the curves in Figure 5.6 are different from the dispersion characteristics in Figure 5.4 due to the dielectric material involved. It is found in Figure 5.6 (b) that the relative dispersion errors are increasing as the dielectric constant increases since the guided wavelength decreases. This means a fine mesh must be applied in the dielectric region of the structure.

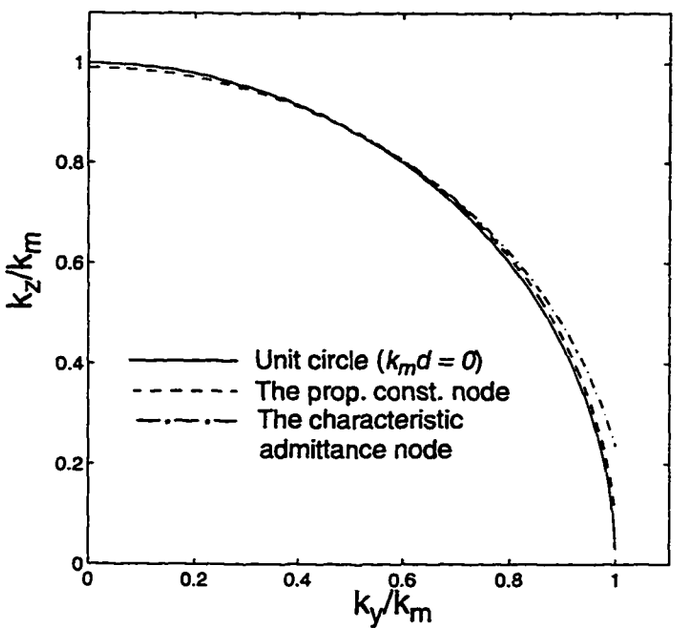

(a)

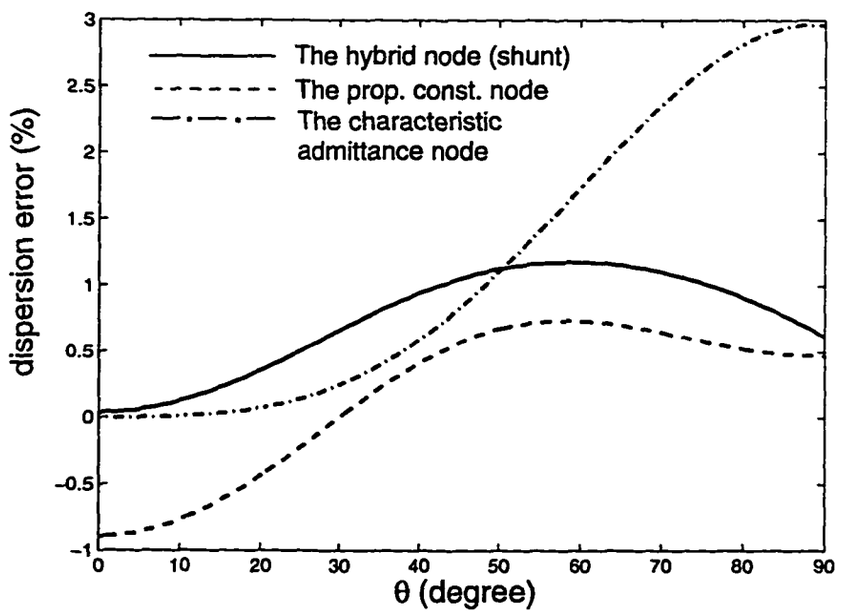

(b)

Figure 5.3 (a) Locus of the normalized propagation vector for the different FDTLM SCNs in the y-z propagation plane (dielectric). (b) Comparison the relative dispersion errors of the different graded FDTLM nodes in the same plane (dielectric). $k_m u = k_m v = 0.05\pi$, $k_m w = 0.1\pi$, $\varepsilon_r = 12$, and $\mu_r = 1$, where k_m is the medium propagation constant

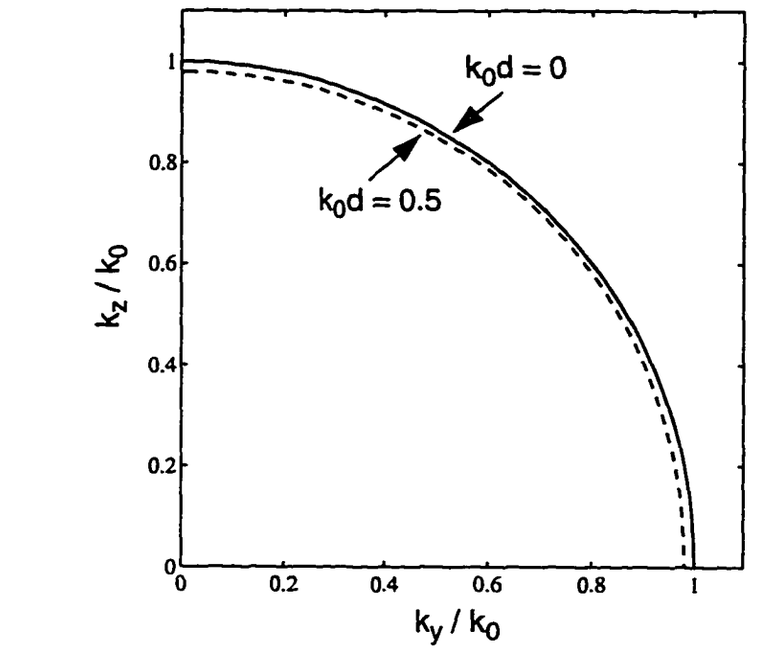

(a)

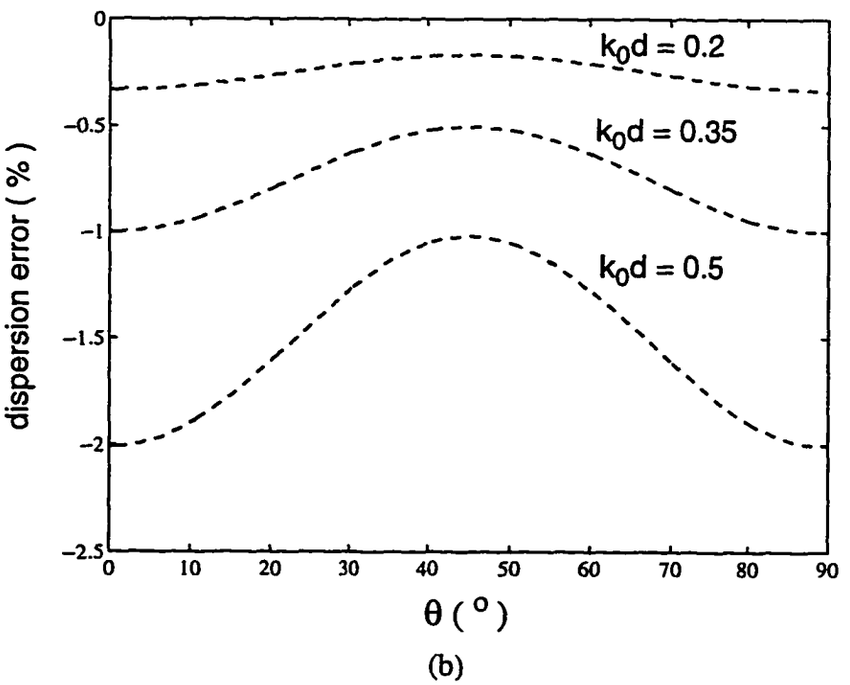

(b)

Figure 5.4 (a) Locus of the normalized propagation vector for a regular FDTLM mesh in the y-z plane ($u = v = w = d$, k_0 is the wave number in free space). (b) The relative dispersion errors for a regular FDTLM node in y-z plane. k_0d=0.2, 0.35 and 0.5

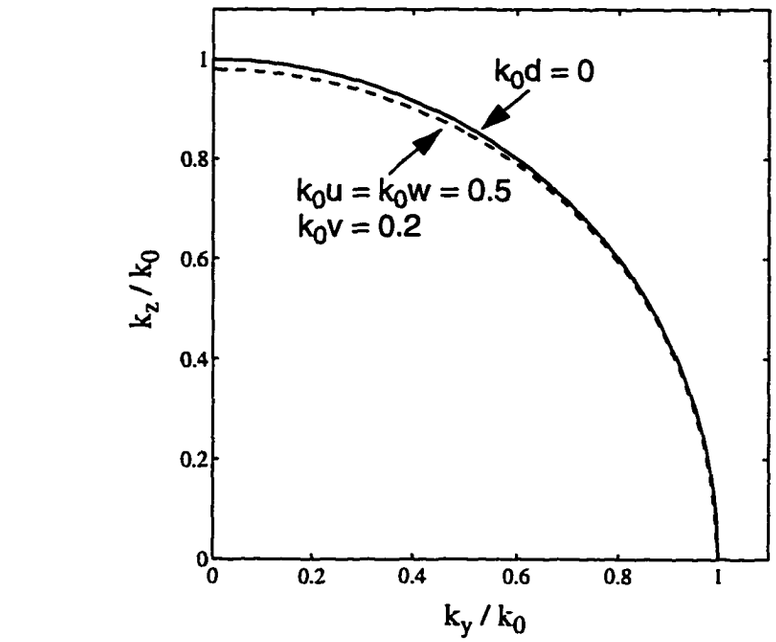

(a)

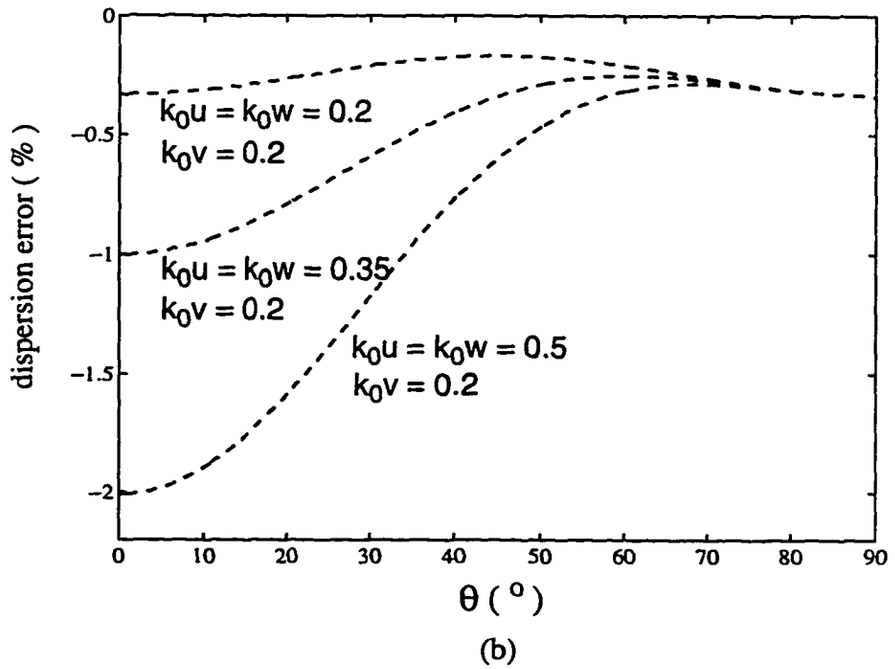

(b)

Figure 5.5 (a) Locus of the normalized propagation vector for a graded FDTLM mesh in the y-z plane. k_0u=k_0w=0.5, k_0v=0.2 (b) The relative dispersion errors of the graded FDTLM node for the different cell aspect ratio: k_0u=k_0w=0.2, 0.35 and 0.5, k_0v=0.2.

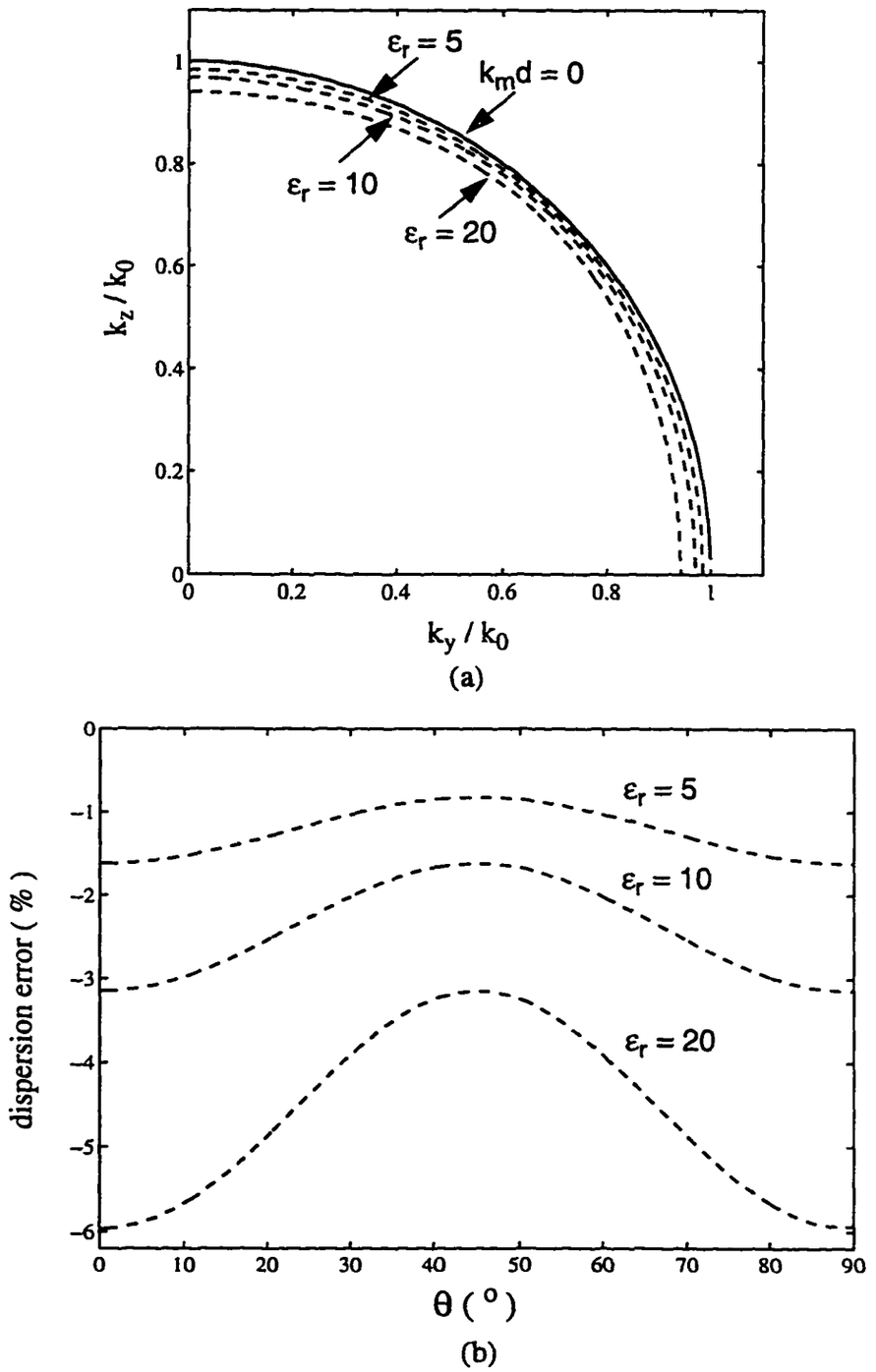

Figure 5.6 (a) Locus of the normalized propagation vector of a FDTLM mesh for the different dielectric constant in the *y*-*z* plane. (b) The relative dispersion errors of a FDTLM node for the different dielectric constant. ε_r= 5, 10 and 20, $k_m d$=0.2 ($u = v = w = d$, k_m is the medium propagation constant).

5.4 Conclusion

In this chapter a general dispersion equation has been proposed for the different frequency-domain SCNs with respect to the port scattering matrix, which is an efficient way to explore and evaluate the various TLM nodes. The dispersion analysis presented in this chapter is based on the numerical solution of an eigenvalue equation for the frequency-domain nodes in terms of the relative dispersion error. This eigenvalue equation is known as an implicit function of the propagation constant k_0 of the travelling wave in the network. By comparing the propagation characteristics of the various FDTLM it has been shown that the hybrid frequency-domain nodes have a better propagation characteristics than the other FDTLM nodes. This can be explained by the fact that the intrinsic parameters, *i.e.* the cell arbitrary aspect ratio, are associated with the capacitance or inductance of the link lines. The dispersion in the relative propagation direction can be minimized. The propagation constant of a suspended stripline has been calculated to illustrated the accuracy of the various nodes. A comparison with data obtained from a spectral domain analysis has also shown that among the different frequency-domain nodes the hybrid node based on the shunt decomposition approach of the SCN provides the best agreement. In the next chapter we will investigate applications of the FDTLM scheme to solve practical semiconductor-based planar transmission line problems including the microwave properties of semiconductor lasers and slow-wave factors in the metal-insulator-semiconductor (MIS) transmission lines.

Chapter 6

Application of FDTLM to Semiconductor-Based Guided Wave Problems

6.1 Introduction

In this chapter, a rigorous field theory analysis of the microwave effects in semiconductor-based guided wave structures will be presented and discussed. The applications are focused on semiconductor laser diode analysis, transition characteristics between passive microwave transmission lines and active devices by flip-chip and airbridge (or bond wire) techniques, as well as mode propagation and field scattering in semiconductor-based coplanar metal-insulator-semiconductor (MIS) slow-wave structures. These problems are solved by using a combination of a self-consistent complex finite different method with the frequency-domain TLM method.

Applying the FDTLM method to semiconductor-based guided wave problems follows a three step procedure. Firstly, we will discuss the frequency-domain TLM algorithm which includes the important concept of the intrinsic scattering matrix for two-dimensional discontinuities (eigenvalue problem) and then outline the FDTLM procedure for the analysis of three-dimensional discontinuities (S-parameter calculation). This is followed by various application examples which will illustrate the flexibility of the FDTLM algorithm. The flip-chip and airbridge/bond wire transition are two examples for alternative techniques to connect laser and photo diodes to the RF circuitry. A theoretical analysis of these transitions will be presented in the literature. In this analysis the semiconductor laser is treated as a lossy multilayer slow-wave microstrip transmission

line. The conductivity profile in the active layer is obtained by a self-consistent solution of the nonlinear semiconductor device equations. Further, a field theoretical analysis of slow-wave mode propagation in semiconductor-based coplanar (CPW) MIS transmission lines with laterally confined doping profile will be investigated. Two types of coplanar MIS transmission line structures are considered: Bulk silicon and semiconductor-on-insulator (SOI). In both cases a Gaussian profile of the doping depth is assumed. The abrupt transition between MIS structures and transmission lines on normal insulating substrate are investigated as well.

6.2 The Frequency-Domain TLM Algorithm

The FDTLM method is based on a variety of possible frequency-domain nodes as discussed in the previous chapter. The network of nodes which discretizes a particular structure is represented by an intrinsic scattering matrix. The concept of the intrinsic scattering matrix is important for guided wave structures with clearly defined propagation direction. For homogeneous structures, i.e. no discontinuity in propagation direction, the intrinsic scattering matrix defines the propagation constant, characteristic impedance and loss factor. For inhomogeneous structures, i.e. two different waveguides connected through a discontinuity junction, the combination of the intrinsic scattering matrices of the two waveguides provides the scattering matrix of that discontinuity. In the following we will first describe the importance of the intrinsic scattering matrix for two-dimensional (2D) discontinuities (eigenvalue problem). We will then outline the FDTLM procedure for the analysis of three-dimensional (3D) discontinuities. Finally, various application examples will illustrate the flexibility of the FDTLM method.

6.2.1 The Intrinsic Scattering Matrix

The computation of the intrinsic scattering matrix (ISM) consumes most of the CPU-time in the FDTLM method. To illustrate the basic idea of the ISM, we first consider a simple two dimensional problem. Extending the concept to three-dimensional problems is then straightforward. To begin with, we first classify the branches of the TLM network that discretizes the cross-section of the waveguide into exterior and interior branches.

Exterior branches are those that point into the propagation direction of the wave, while interior branches provide a connection between the TLM nodes in the transverse direction. In a two-dimensional problem the structure is homogeneous in propagation direction and thus only one space node is required [7]. In the transverse direction the number of space nodes depends on the accuracy with which the field is to be modeled.

In the formulation of the ISM, the incident and reflected voltages of the interior branches are expressed by the incident and reflected voltages of the branches pointing in propagation direction (exterior branches). The advantage if this approach becomes evident when, for example, two waveguides of different dimensions are connected through an abrupt transition. This case is modeled in the FDTLM by directly connecting the exterior branches of the ISM's of both waveguide sections. The S-parameters of this transition are then extracted by exciting the input waveguide with the corresponding fundamental mode. The voltage distribution of this mode can be found from the eigenvalues of the ISM of the respective waveguide section. Hence, irrespective of the type of problem to be solved (2D eigenvalues or 3D scattering), the ISM of the particular structure must always be established first.

In a Cartesian coordinate system the ISM is found as follows. If the z-axis is defined as the propagation direction of the wave, then the two classes of branches are (in Figure 3.1):

Exterior branches: +zx, +zy, -zx, -zy.

Interior branches: +xy, +xz, -xy, -xz;

+yz, +yx, -yz, -yx.

The interior branches between neighboring nodes are connected through the following relationship

$$V_x^i = C_x \cdot V_x^r$$

$$V_y^i = C_y \cdot V_y^r \qquad (6.1)$$

where C_x and C_y are the connection matrices and $V^i_{x,y}$, $V^r_{x,y}$ are the incident and reflected voltages between neighboring nodes. The scattering matrix of the TLM network is then defined as:

$$\begin{bmatrix} V^r_z \\ V^r_x \\ V^r_y \end{bmatrix} = \begin{bmatrix} S_{zz} & S_{zx} & S_{zy} \\ S_{xz} & S_{xx} & S_{xy} \\ S_{yz} & S_{yx} & S_{yy} \end{bmatrix} \cdot \begin{bmatrix} V^i_z \\ V^i_x \\ V^i_y \end{bmatrix} \tag{6.2}$$

Eliminating $V^i_{x,y}$, $V^r_{x,y}$ in Eq. (6.2) by using Eq. (6.1), yields the ISM of the structure which provides a relationship between incident and reflected voltages of the exterior branches [37]:

$$V^r_z = [S_{ISM}] \cdot V^i_z \tag{6.3}$$

where

$$\begin{aligned} S_{ISM} = {} & S_{zz} + S_{zx} \cdot C_x \cdot P \cdot (M \cdot S_{xz} + M \cdot S_{xy} \cdot C_y \cdot N \cdot S_{yz}) \\ & + S_{zy} \cdot C_y \cdot Q \cdot (N \cdot S_{yz} + N \cdot S_{yx} \cdot C_x \cdot M \cdot S_{xz}) \end{aligned} \tag{6.4}$$

and

$$M = (I - S_{xx} \cdot C_x)^{-1}$$

$$N = (I - S_{yy} \cdot C_y)^{-1}$$

$$P = (I - M \cdot S_{xy} \cdot C_y \cdot N \cdot S_{yx} \cdot C_x)^{-1}$$

$$Q = (I - N \cdot S_{yx} \cdot C_x \cdot M \cdot S_{xy} \cdot C_y)^{-1}$$

From the ISM (6.3), an eigenvalue equation can be formulated from which the mode field distribution over the cross-section of the guide can be determined. To do so we first rewrite Eq. (6.3) as

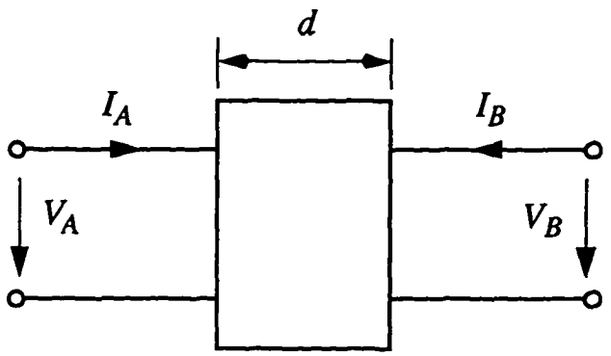

Figure 6.1 A slice of homogeneous waveguide structure.

$$\begin{bmatrix} V_A^r \\ V_B^r \end{bmatrix} = \begin{bmatrix} S_{AA} & S_{AB} \\ S_{AB} & S_{BB} \end{bmatrix} \cdot \begin{bmatrix} V_A^i \\ V_B^i \end{bmatrix} \tag{6.5}$$

where $V_{A,B}^i$ and $V_{A,B}^r$ are the incident and reflected voltage vectors, respectively, of the exterior branches. If the node dimension is d in the z-direction, then the voltages at plane A, as shown in Figure 6.1, are related to the voltages at plane B (the port voltages of the exterior branches) by $e^{\gamma d}$. This relationship is easily established by first converting the ISM of Eq. (6.5) into the transfer matrix

$$\begin{bmatrix} V_A \\ I_A \end{bmatrix} = A \cdot \begin{bmatrix} V_B \\ I_B \end{bmatrix} = \begin{bmatrix} SR^{-1} & SR^{-1}S - R \\ R^{-1} & R^{-1}S \end{bmatrix} \cdot \begin{bmatrix} V_B \\ I_B \end{bmatrix} \tag{6.6}$$

where

$$S = \left[(I - S_{AA}) - S_{AB}(I - S_{AA})^{-1} S_{AB} \right]^{-1} (I + S_{AA})$$
$$- \left[(I - S_{AA}) S_{AB}^{-1} (I - S_{AA}) - S_{AB} \right]^{-1} S_{AB}$$
$$R = \left[(I - S_{AA}) - S_{AB}(I - S_{AA})^{-1} S_{AB} \right]^{-1} S_{AB}$$
$$- \left[(I - S_{AA}) S_{AB}^{-1} (I - S_{AA}) - S_{AB} \right]^{-1} (I + S_{AA})$$

Let the propagation constant in the z-direction be γ, then Floquet's theorem implies that

$$\begin{bmatrix} V_B \\ I_B \end{bmatrix} = e^{\gamma d} \cdot \begin{bmatrix} V_A \\ I_A \end{bmatrix} \tag{6.7}$$

Thus, the transfer matrix of the TLM cell must satisfy the eigenvalue equation

$$A \cdot \begin{bmatrix} V \\ I \end{bmatrix} = e^{\gamma d} \cdot \begin{bmatrix} V \\ I \end{bmatrix} \tag{6.8}$$

The solution of Eq. (6.8) is simplified if we consider the analytical properties of the matrix A. We first observe that if Eq. (6.8) is satisfied, then the following eigenvalue equation is also satisfied.

$$\frac{1}{2}\left(A + A^{-1}\right) \cdot \begin{bmatrix} V \\ I \end{bmatrix} = \frac{1}{2}\left(e^{\gamma d} + e^{-\gamma d}\right) \cdot \begin{bmatrix} V \\ I \end{bmatrix} = \cosh(\gamma d) \cdot \begin{bmatrix} V \\ I \end{bmatrix} \tag{6.9}$$

From here a reduced eigenvalue equation can be established which must be solved for γ:

$$\left(SR^{-1}\right) \cdot V = \cosh(\gamma d) \cdot V \tag{6.10}$$

6.2.2 *S*-Parameter Algorithm

The S-parameters of a 3D discontinuity are found from a three step procedure [7, 37]: First, the eigenvalues of the input and output waveguides are determined from eigenvalue equation (6.10); second, the reflection matrices of both connected waveguides (Figure 6.2) with respect to the discontinuity plane are determined; third, the left port is excited with the fundamental wave form of the left waveguide. Then from the reflected and transmitted mode amplitudes the S-parameters can be found.

For example, the reflection matrices for the left and right waveguides in Figure 6.2 are found from the eigenvalues of Eq. (6.10) as

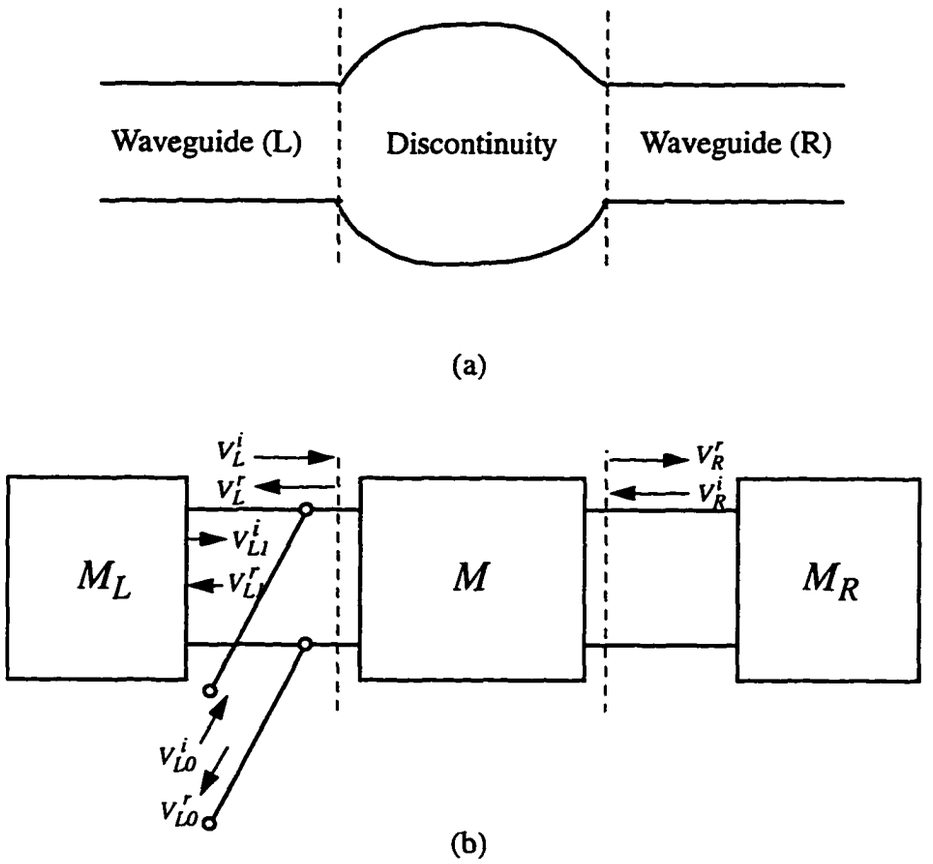

Figure 6.2 (a) Two-port waveguide discontinuity and (b) the equivalent network.

$$M_L = \left[V_{Ln}^r\right] \cdot \left[V_{Ln}^i\right]^{-1} \tag{6.11}$$

$$M_R = \left[V_{Rn}^r\right] \cdot \left[V_{Rn}^i\right]^{-1} \tag{6.12}$$

where each column in matrices $[V_{Ln}]$ and $[V_{Rn}]$ is associated with the incident and reflected voltages for each mode on the exterior branches. The incident and reflected modes in the discontinuity plane are related through

$$\begin{bmatrix} V_L^r \\ V_R^r \end{bmatrix} = M \cdot \begin{bmatrix} V_L^i \\ V_R^i \end{bmatrix} = \begin{bmatrix} M_{LL} & M_{LR} \\ M_{RL} & M_{RR} \end{bmatrix} \cdot \begin{bmatrix} V_L^i \\ V_R^i \end{bmatrix} \tag{6.13}$$

where $V_L^{i,r}$ are the vectors containing the incident and reflected modes on the left hand side of the discontinuity (Figure 6.2) and $V_R^{i,r}$ are those on the right hand side. V_R^i and V_R^r are related as

$$V_R^i = M_R \cdot V_R^r \tag{6.14}$$

Vectors V_L^r and V_L^i are a combination of the excitation V_{L0}^i and V_{L0}^r, and the resulting reflection from the left waveguide V_{L1}^i and the discontinuity V_{L1}^r:

$$V_L^i = V_{L0}^i + V_{L1}^i \tag{6.15}$$

$$V_L^r = V_{L0}^r + V_{L1}^r \tag{6.16}$$

From the relationships $V_{L0}^r = M_L \cdot V_{L0}^i$ and $V_{L1}^i = M_L \cdot V_{L1}^r$ as well as the above one can find

$$V_{L1}^r = (M_L \cdot T_r - I)^{-1} \cdot (M_L - T_r) \cdot V_{L0}^i \tag{6.17}$$

$$V_R^r = T_r \cdot \left(M_L \cdot V_{L1}^r + V_{L0}^i \right) \tag{6.18}$$

where

$$T_r = M_{LL} + M_{LR} \cdot M_R \cdot T_t$$

and

$$T_t = (I - M_{RR} \cdot M_R)^{-1} \cdot M_{RL}$$

After appropriated power normalization of the mode vectors [7], the above equations yield the *S*-parameters of the discontinuity.

6.2.3 Application Examples

The frequency-domain TLM scheme is first tested by calculating the scattering

parameters S_{11} and S_{12} of two microstrip discontinuity examples, an air-bridge (or bonding wire) interconnecting two microstrip transmission lines and a microstrip gap discontinuity. As it is well known, these two microwave structures are frequently used in MIC or MMIC planar circuits. Results obtained with the hybrid frequency-domain node are compared with those obtained by the spectral domain approach and the FDTLM method with propagation constant node. Experimental data is shown for comparison. The first example (Figure 6.3) shows the calculated S-parameters for an airbridge interconnection between two microstrip lines (d = w = g = 0.635 mm and h = a = w_b = 0.211 mm). The strip thickness is assumed to be zero and the dielectric constant is $\varepsilon_r = 9.8$ for alumina substrate. In the simulation with the hybrid frequency-domain node, half of the microstrip line is discretized with 9 nodes in the x-direction and 9 nodes in the y-direction utilizing a graded mesh. The cell aspect ratios are chosen freely according to the rule of placing coarse nodes in the air region and fine nodes in the metallic strip and air-bridge regions since the electric field changes fast at the edges and corners of that structure. It can be seen that the results obtained by the FDTLM are in good agreement with the SDA [63] especially at the lower frequencies. In the second example, a microstrip gap discontinuity has been analyzed, where the structure dimensions are $d = w = 0.635$ mm and $g = 0.35w$. The dielectric constant is $\varepsilon_r = 9.9$ for an alumina substrate. Figure 6.4 illustrates the simulation results from the hybrid frequency-domain node for this discontinuity. At the same time, the results from the frequency-domain propagation constant node calculated by Jin and Vahldieck [7] and experimental data measured by Drissi, et al. [64] are also displayed in the same figure. Compared to experimental data a good agrement is observed.

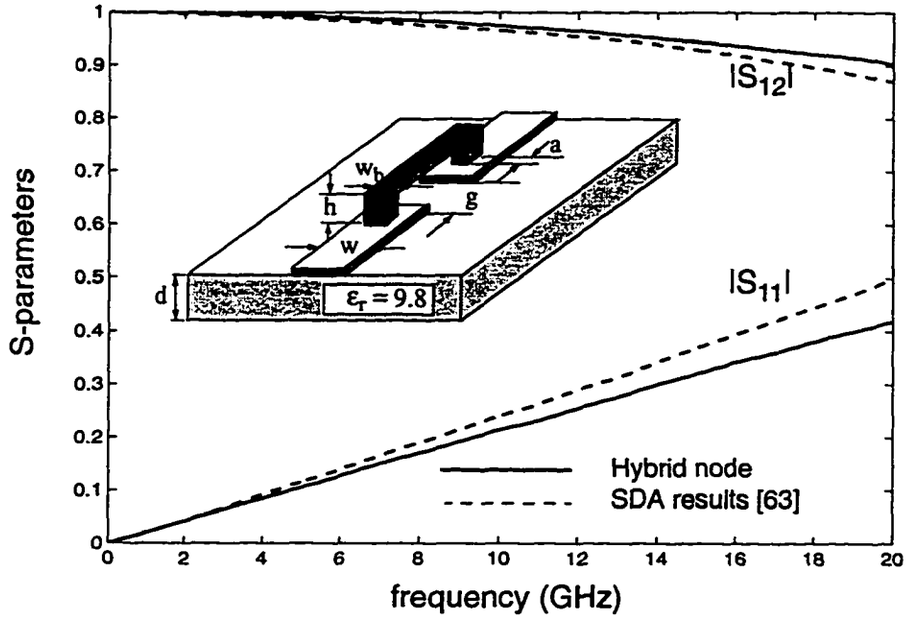

Figure 6.3 Frequency-dependent scattering parameters for an air-bridge interconnection between two microstrip transmission lines ($d = w = g = 0.635$ mm and $h = a = w_b = 0.21$ mm).

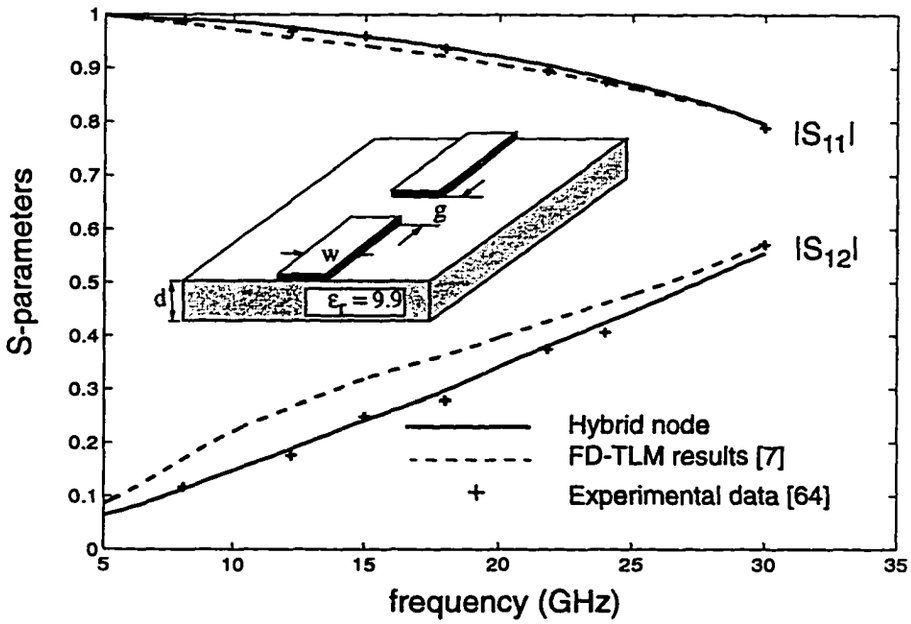

Figure 6.4 Frequency-dependent scattering parameters for a microstrip gap discontinuity ($d = w = 0.635$ mm and $g = 0.35w$).

6.3 Analysis of the Direct Transition Between Passive Microwave Transmission Lines and Laser Diodes

As mentioned in Chapter 2, wide bandwidth directly modulated laser chips are attractive sources for fiber optical links operating at microwave frequencies due to simplicity of operation and the absence of coupling losses associated with external modulations. This technique reduces the packaging parasitic reactances which is known as one of the main effects to restrain the laser diode in high frequency and broadband applications. In this section the numerical investigation will focus on this complex electromagnetic issue. According to the measurement by Tauber et.al. [12], a lossy and slow-wave transmission line model (Figure 2.1) for the accurate characterization of the laser diode has been proposed in this thesis. Based on the model of a laser diode in Chapter 2, in which a slow-wave microwave transmission line model is developed, the FDTLM method is utilized to analyze semiconductor laser diodes and their distributed microwave effects. The results are compared with experimental data from [12]. Furthermore, we investigate the electrical performance of airbridge and flip-chip interconnection between passive microwave transmission lines and the laser structure, such as schematically in Figure 6.5. Such an analysis has not been seen in the literature.

6.3.1 Lossy and Slow-Wave Transmission Line Model for Laser Diode

Figure 2.1 shows the semiconductor laser configuration with a separate confinement heterostructure, where an optical slab waveguide is formed by the active region sandwiched between two cladding layers. From the microwave perspective, the laser diode represents a lossy and dispersive slow-wave transmission line. The lossy and slow-wave laser model is suitable for most double heterojunction and quantum-well laser diodes. Figure 6.6 shows the microwave current flowing in the laser diode under high frequency modulation [12]. The vertical currents shunt across the active region and pump the laser diode. These current modulate the injected current and change the carrier distribution in the laser active region. Because the current flows through several layers of substrate with different properties, it is obvious that this transmission line is dispersive and

very lossy. The microwave losses and propagation are frequency dependent due to the skin effect associated with the longitudinal currents.

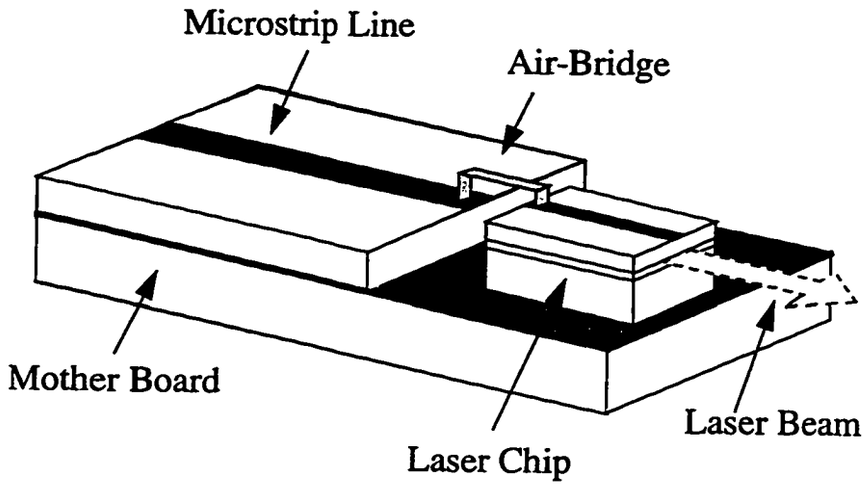

(a)

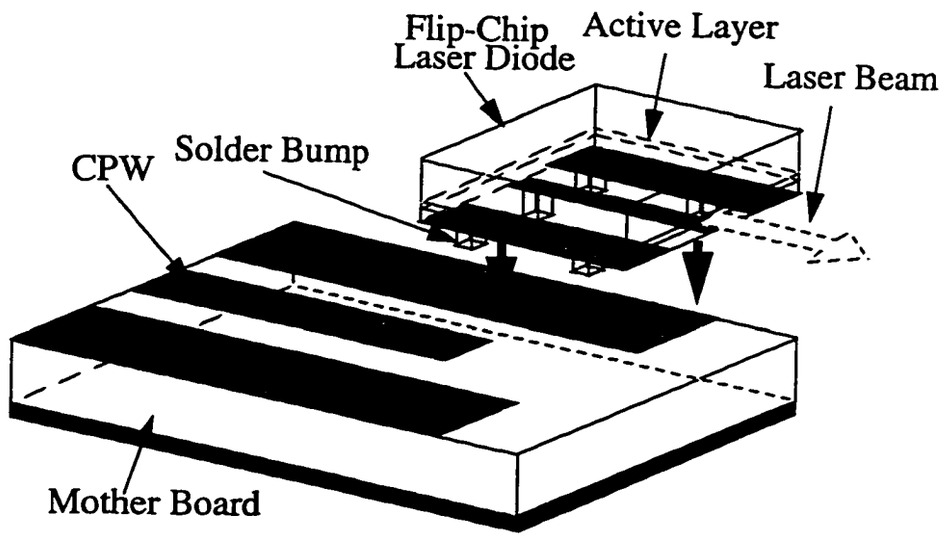

(b)

Figure 6.5 (a) The air-bridge and (b) flip-chip connection between semiconductor laser chip and microwave transmission line.

The skin depth δ_s for the substrate is defined as the depth at which the RF current density has decreased to 1/e of its maximum value as given by:

$$\delta_s = \sqrt{\frac{1}{\pi f \mu \sigma}} \tag{6.19}$$

where σ is the conductivity of the substrate. For the semiconductor substrates the skin depth depended on the doped level.

In the semiconductor laser the loss has several sources. First, the thick *n*-doped cladding and substrate form a lossy ground plane for the transmission line. For example, the skin depth in the semiconductor for the microwave frequency range is significantly less than 100 μm thickness in the n-cladding layer and *n*-side substrate. In this case, all of the longitudinal current on the *n*-side is carried in the doped regions, but not in the metallic ground plane. The poor conductivity of the *n*-side regions will cause significant microwave losses. In contrast, the 1~2μm thick p-cladding layer is thinner than the semiconductor skin depths and thus the longitudinal p-side currents will penetrate into the strip (gold) contact layer. The RF current should partially be carried in the strip conductor with high conductivity and partially carried in the *p*-cladding layer with poor conductivity. Therefore, the second loss source comes from the thin *p*-side contact. Because a laser diode is a bias dependant device, the third loss source is the forward biased junction, which is a dissipative shunt path. Since slow-wave effects are commonly observed in a lossy semiconductor substrates [65], the laser diode can be modeled as a lossy, slow-wave and dispersive microwave transmission line. An accurate characterization of the distributed microwave effects in laser diodes is very important for integration and interconnection with passive microwave feed networks. In the following we perform a field theoretical analysis of a class of semiconductor laser diodes and their distributed microwave effects using the FDTLM method in combination with the complex finite difference method.

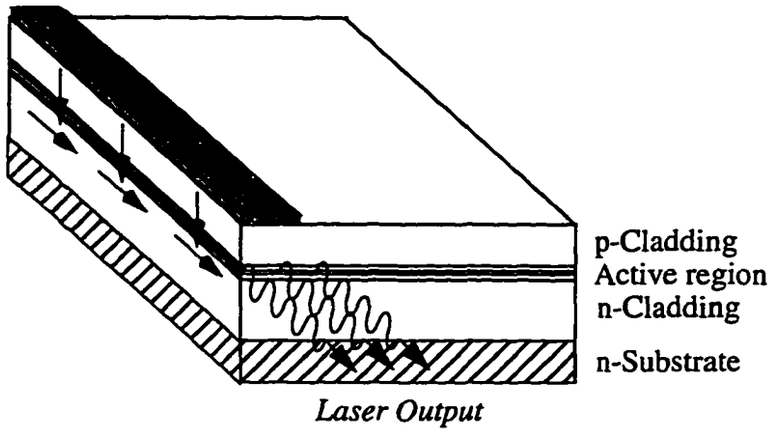

Figure 6.6 Microwave currents flowing in the semiconductor laser under high frequency modulation. The horizontal arrows represent the longitudinal currents and the vertical arrows represent signal injection current into the active region.

6.3.2 Distributed Microwave Effects: Analysis and Numerical Results

The transition of the semiconductor laser to either a microstrip or coplanar transmission line, as shown in Figure 6.5, presents a three dimensional circuit discontinuity. The modulating microwave signal and the DC biasing current are fed into the laser chip by either an airbridge or a flip-chip interconnection. Besides its broadband performance, the flip-chip transition is of significant interest, because it may also alleviate the mechanical alignment problems in focussing the laser beam into a single mode fiber. In view of the electrical performance, however, the low input impedance of the laser diode may be difficult to match, because the line dimensions may be impossible to realize in either CPW or microstrip and thus abrupt discontinuities between both transmission lines may lead to significant reflections. Before we investigate this problem in more detail we will first present results for the laser diode as an active transmission lines.

6.3.2.1 Propagation Parameters and Characteristics Impedance

As mentioned in the previous section because the current flows through several layers of substrate with different properties, the laser is certainly highly dispersive, very

lossy and exhibits a slow-wave behavior. The attenuation and phase velocity for the laser structure considered here is obtained from the FDTLM analysis. Figure 6.7 shows a schematic diagram of a FDTLM simulation of a laser diode. The conductivity profile, which is a function of the bias condition given in Chapter 2, is then used to represent the active layer as a lateral inhomogeneous doped substrate layer when we analyze the laser diode as a lossy and slow-wave microstrip structure. Results for the microwave attenuation of the structure are shown in Figure 6.8 (a). In comparison to the measured results for the unbiased and forward biased case, the model predicts the correct attenuation trend in which the loss of the laser diode increases monotonically with the modulation frequency. The difference to the theoretical results is relatively small. The same can be said about the phase velocity in Figure 6.8 (b). The curves for the biased and unbiased case are very close, which is also confirmed by measurements. Also here the tendency over the frequency is the same. Comparing both figures it is evident that the attenuation is much more affected by the bias current than the propagation constant. A possible explanation for this is that at forward bias, the conductivity in the undoped active layer increases significantly due to the high electron-hole pair injection, which is approximately $2 \sim 3 \times 10^{18}$ cm^{-3}. This will result in a significant increase in the attenuation. However, its effect on the phase constant must be small because this highly conductive layer is very thin compared to the cladding layers. At the same time, the simulation results predict the slow-wave nature of the laser diode as well. With respect to the results of Figure 6.8, it should be noted that we do not know the exact cross-section of the structure measured in [12]. Our theoretical model (Figure 6.7) may be too simple. However, we believe that although the absolute value for the attenuation and phase constant may change depending on the layers and their characteristics, the general tendency of the results will remain the same.

Measurement results for the characteristic impedance have so far not been available in the literature. However, according to our calculation the theoretical results are shown in Figure 6.9 for the real and imaginary part of the characteristic impedance of the laser diode, where the power-voltage definition is adopted for the characteristic impedance

calculation. Also here it can be seen that the characteristics impedance of the laser diode depends on both the modulation frequency and the bias voltage. When the frequency range increases from 1 GHz to 100 GHz, the real parts of the characteristics impedance change from 2.5 Ω to 13 Ω with bias, and 5 Ω to 15 Ω without bias, respectively. While the imaginary parts change from 2 Ω to 12 Ω for both cases of biased and unbiased laser. The increase in the characteristic impedance values with frequency is probably due to the skin effect in the various layers of the structure. The influence of the bias current on the characteristic impedance is not significant. The real part seems to be more affected because in forward bias more carriers are injected into the active layer which increases its conductivity. This equivalently short-circuits the lower *n*-doped layer in the substrate, consequently reducing the real part of the characteristic impedance of the laser diode.

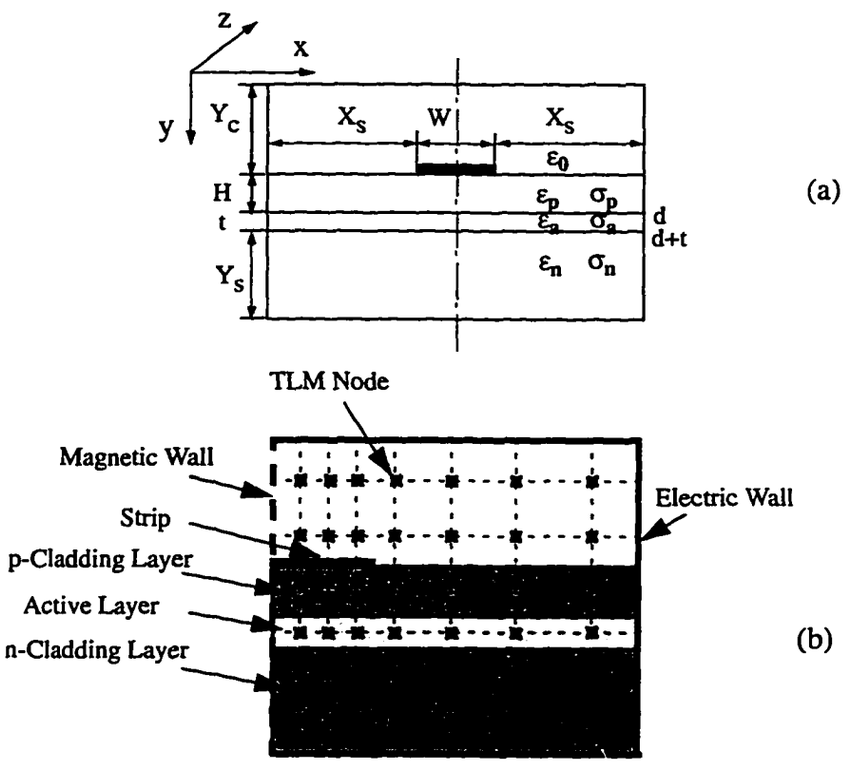

Figure 6.7 (a) Multilayered semiconductor substrate microstrip model for laser diode. (b) Layout of the FD-TLM graded mesh.

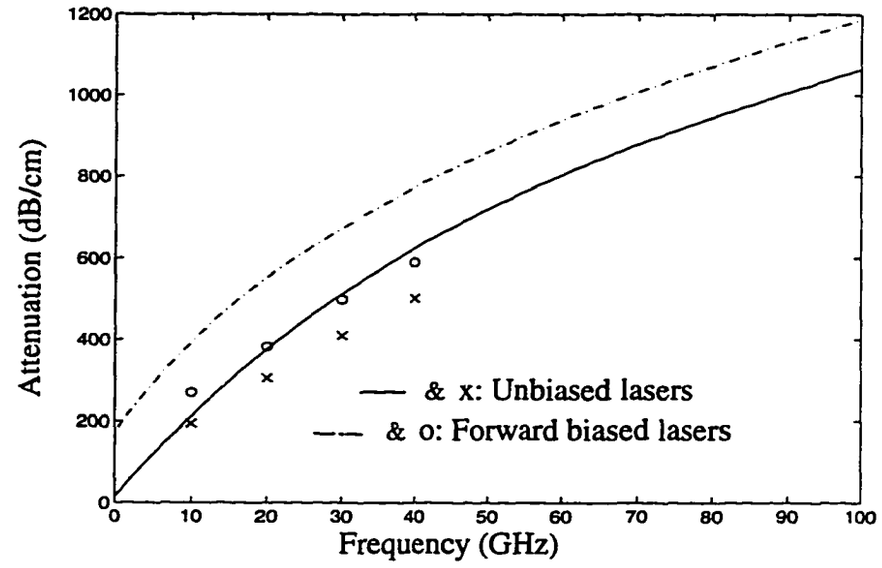

(a)

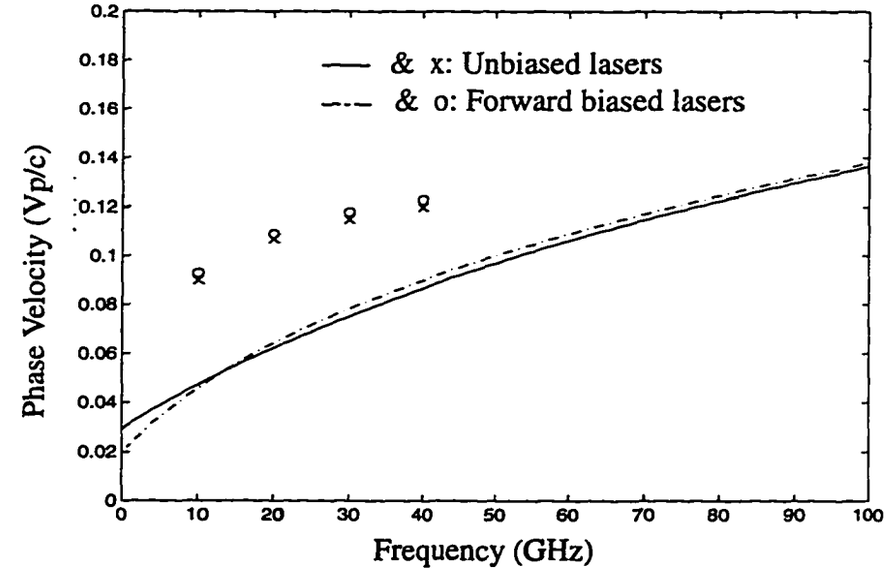

(b)

Figure 6.8 (a) Microwave attenuation per unit length vs. frequency. (b) Phase velocity, normalized to the speed of light in free space, vs. frequency. The solid line and dash-dot line represent numerical results from the FDTLM analysis and the points represent measured values given in [12].

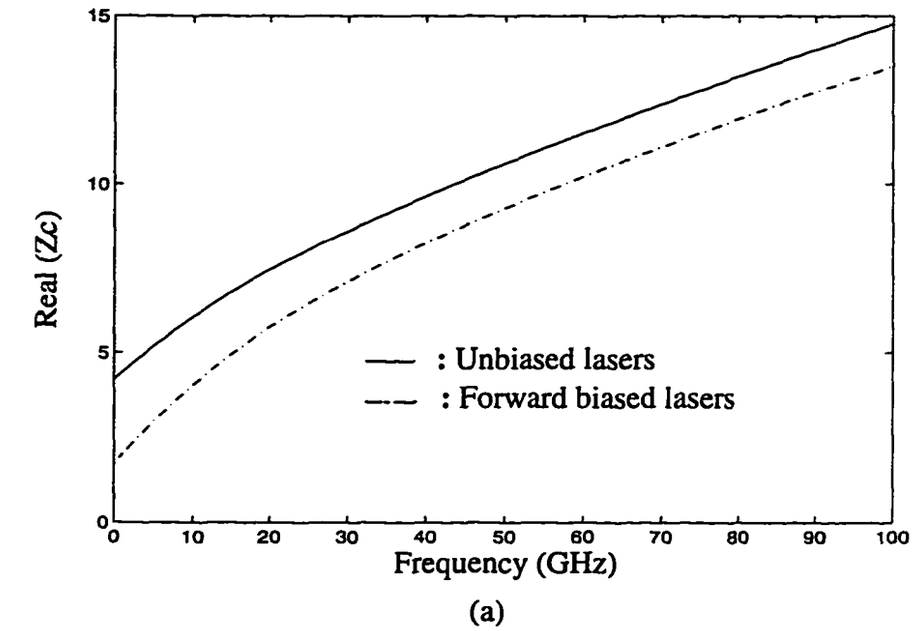

(a)

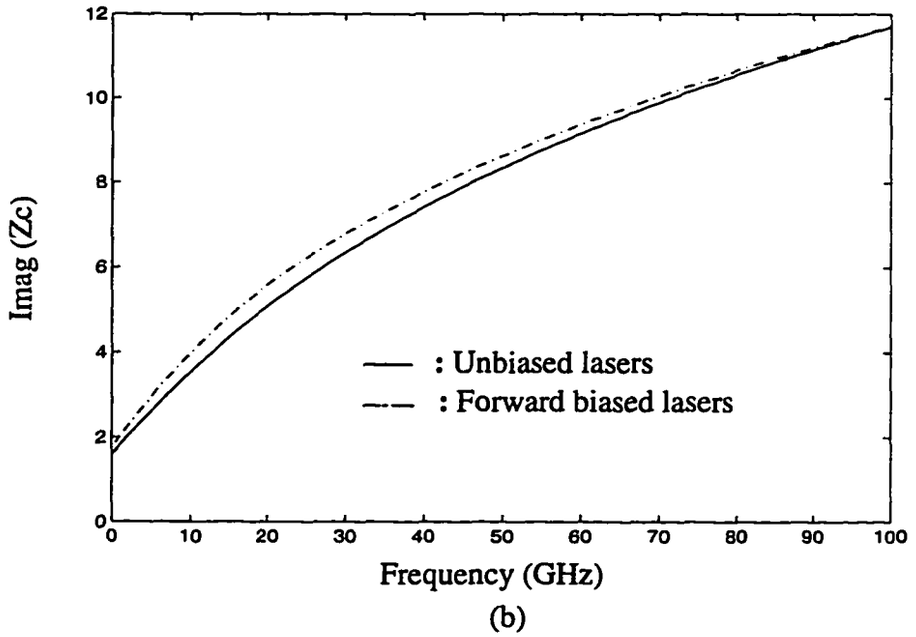

(b)

Figure 6.9 (a) The real part of characteristics impedance of the laser diode vs. frequency. (b) The imaginary part of characteristics impedance vs. frequency. The lines represent numerical results from the FDTLM analysis.

6.3.2.2 Interconnection of Laser Diode with Passive Transmission Line

Interconnecting the laser chip with a microstrip transmission line by an airbridge is sketched in Figure 6.10. The simulated results for the effect of the length of the laser cavity and airbridge on the coupling coefficients are demonstrated in Figure 6.11. The operating frequency is assumed to be 25 GHz and the laser chip emits light at 980nm. From Figure 6.11 (a) it is evident that the transmission coefficient changes slightly when the length of the laser cavity increases from 100μm to 400μm. From Figure 6.8 (a) it is evident that this is due to the high losses of the laser chip for a modulation frequencies of 25 GHz (α=600 dB/cm). Almost all the energy of the wave reflected from the far end of the laser cavity is attenuated over the length of 100μm. Therefore, the laser appears as a lossy transmission line of infinite length. Hence, the coupling coefficient depends only on the airbridge discontinuity and the mismatch between impedances of the microstrip line on the mother board and the laser chip. This is clearly shows in Figure 6.11 (b) where the laser chip length is kept constant but the length of the airbridge is varied. For short length of the airbridge the S_{11} is quite high. This is also due to the impedance mismatching between the 50 Ω microstrip line and a low-impedance laser chip. Meanwhile, the slow-wave propagation in the laser chip is an important effect for the high reflection at the input port. When the length of the airbridge is increased, the standing wave can be observed in the S-parameter versus the length of the airbridge. This is due to the fact that laser chip is with high slow-wave factor. Therefore, this standing wave effect shows the guided wavelength in laser chip is dramatically decreased.

The performance of the S_{11} of the airbridge and, for comparison, the flip-chip interconnection over the frequency range of 2.5 to 40 GHz is presented in Figure 6.12. The flip-chip (Figure 6.5 (b)) result presents the transition between the laser diode and a coplanar waveguide (CPW). From Figure 6.12 it is evident that the flip-chip transition is suitable for high frequencies applications. We will further discussion this issue in the next section.

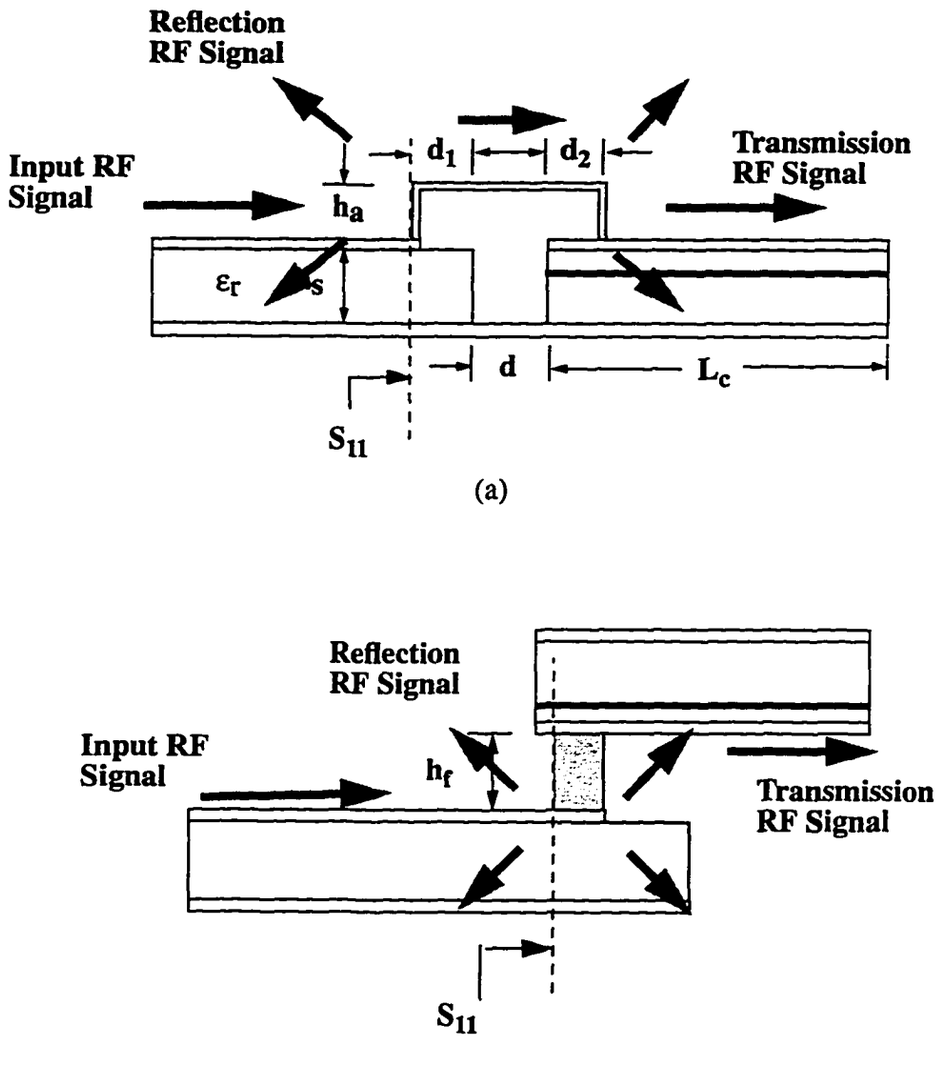

Figure 6.10 (a) The air-bridge (bonding wire) transition between semiconductor laser chip and microstrip transmission line. (b) The flip-chip transition between semiconductor laser chip and coplanar waveguide (CPW).

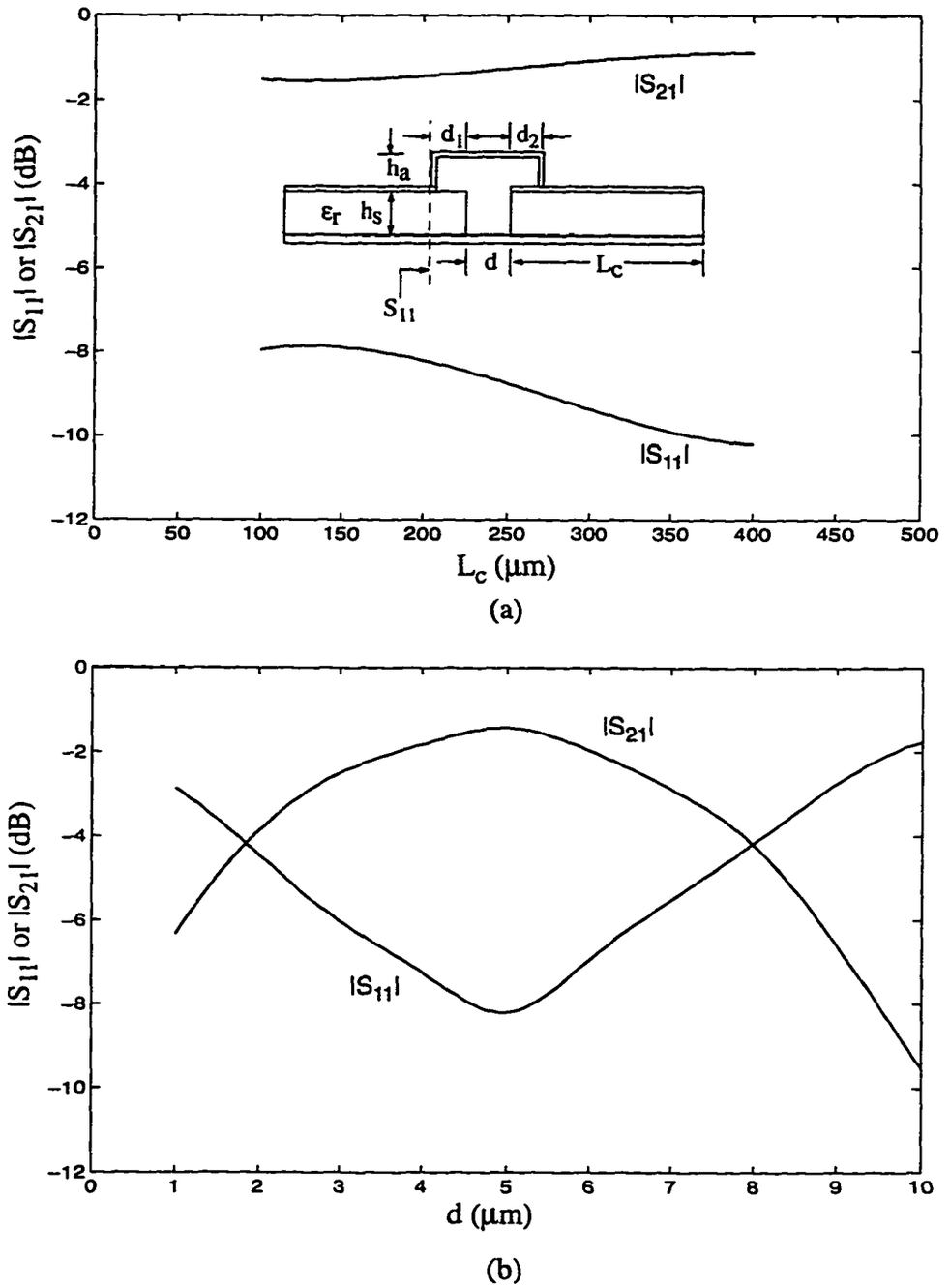

Figure 6.11 The S-parameters of the airbridge interconnect assembly (d_1=d_2=3μm, h_a=2μm, h_s=100μm, ε_r=12.9, f=25GHz). (a) as a function of the length L_c of the laser chip, and (b) the gap d between the mother board and the laser chip.

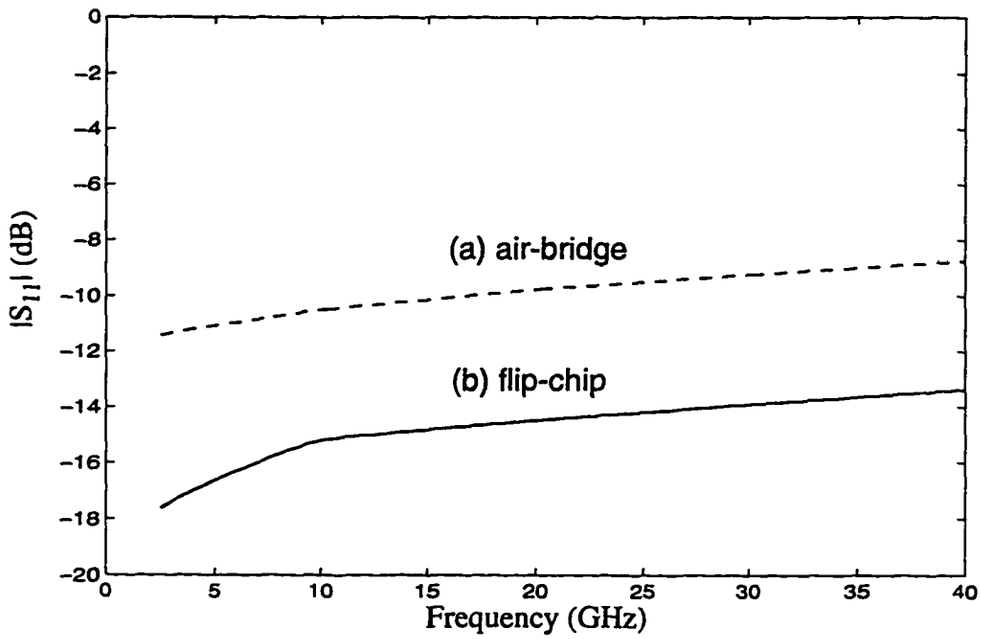

Figure 6.12 Comparison between a flip-chip transition and an airbridge interconnection. For the flip-chip transition a CPW with 6μm slot width and 12μm center conductor width is assumed. For the airbridge interconnection the data is given in Figure 6.11.

6.3.3 Discussion and Summary

As mentioned in the previous section, in comparison with bonding wire or airbridge interconnections, the flip-chip transition between the CPW to the laser chip two CPW's shows clearly the best electrical performance. A similar result was also shown in [66, 67] for two CPWs flip-chip transition, where both CPWs have same characteristic impedance. In this case the electrical performance of the junction was only determined by a bump connection between the center conductors and ground planes of both CPW's. Since this geometry ensures that the field orientation in both transmission lines remains essentially undisturbed, this good transfer characteristics is not surprising.

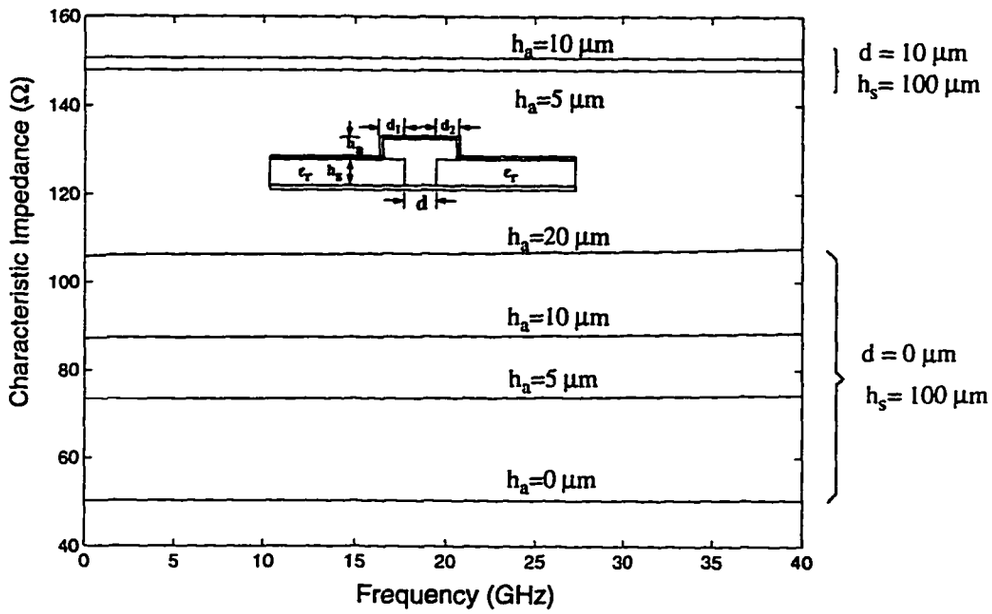

Figure 6.13 Characteristic impedance of the airbridge via frequency (h_s=100μm, ε_r=12.9).

For the case of an airbridge or bound wire connection between two microstrip lines of equal characteristic impedance, two problems are encountered: first, the field of the incident wave is significantly disturbed by the geometry of the junction and, second, the airbridge, which is essentially a short bond wire, shows very different characteristic impedances [68, 69, 70]. Depending on the height of the wire (or ribbon line in case of the airbridge) above the substrate, and depending on whether or not a dielectric gap between both transmission lines is considered, the characteristic impedance, Z_0, along the airbridge can vary considerably as shown in Figure 6.13. Here the characteristic impedance is calculated at the location where the dielectric gap between both transmission lines occurs. For a gap $d=0$, Z_0 ranges from 50 Ω to 106 Ω, depending on the height of the wire. This value increases significantly if an air gap of 10 μm between both transmission lines is considered. In this case and for example h_a=10 μm, the wire impedance varies from 106 Ω (at d_1) to 150 Ω (at d) and to 106 Ω (at d_2). Since very little dispersion is observed, the values of the effective dielectric constant, ε_{eff} and the characteristic impedance, Z_0,

obtained from the method of lines (MoL) [70] calculations are compared with those from a quasi-static analysis in [68] and the results are shown in Figure 6.14. Considerable differences in the ε_{eff}-values calculated by the different numerical methods can only be observed for zero and small conductor heights above the substrate. The effect of the impedance steps of the wire in conjunction with the discontinuity the junction presents to the incident wave results in an electrical performance that is inferior to that of the flip-chip transitions.

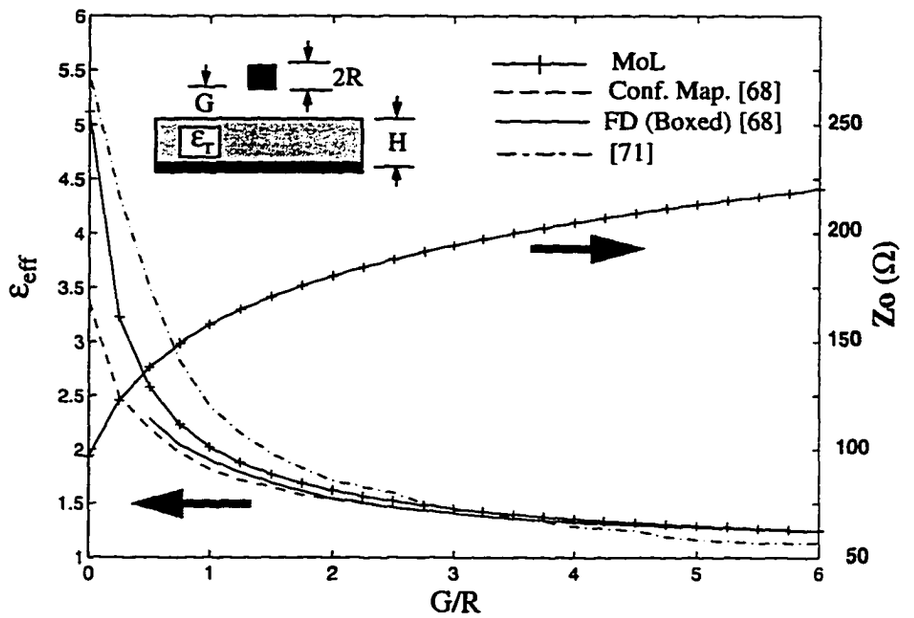

Figure 6.14 Effective dielectric constant and characteristic impedance versus spacing between wire and substrate for H/R=10 and ε_r=9.6.

6.4 Characteristics of Slow-Wave Propagation on Semiconductor based Coplanar MIS Structures

6.4.1 Background of Coplanar MIS Transmission Line

It is well known that metal-insulator-semiconductor (MIS) transmission lines

support slow-wave mode propagation. This phenomenon combined with the attractive features of CPW are of increasing interest in the design of monolithic microwave integrated circuits (MMIC) for wireless communications systems in the 1~2GHz range and for high-speed digital integrated circuits. The slow-wave mode propagating in such a structure can be considered as: The doped semiconductor is invisible to the magnetic field while the electric field of the wave is highly concentrated in a thin insulating layer between the doped semiconductor and the strip conductor. Hence, the condition for a slow-wave propagation is the separate storage of magnetic and electric energy in space. However, slow-wave mode propagation in semiconductor-based transmission lines comes at the price of relatively high losses and low Q-factors, which are problems that have prevented the widespread use of MIS CPW in the past. This problem has been studied experimentally and theoretically by several researchers [72, 73, 74, 75, 76, 77, 78] and it was found that thin-film MIS CPW are in general less lossy than thick-film structures [77, 79], but that the latter can sustain slow-wave mode propagation over a wider frequency range than the former. A compromise between maximum slow-wave factor and minimum losses can be found either by carefully controlling the doping layer thickness or by limiting the lateral width of the doping region. The latter approach was investigated by Wu and Vahldieck [79, 80] in that the doping level was gradually varied in lateral direction with maximum doping below the center conductor. Although this approach is generally helpful in reducing the losses and improving the Q-factor at a moderate slow-wave factor, its practical realization is difficult with epitaxial technology. A better approach is to keep the doping level constant within a laterally confined region. The lateral width of the doping region must then be optimized for maximum slow-wave factor and minimum losses.

In the following section, this problem is investigated in more detail with special consideration for the physical process of realizing MIS CPW. As it is well known, ion implantation into a semiconductor is easily achieved through a mask window. However, this results in an abrupt transition between the doped and the undoped region. Applied to a thin-film MIS CPW, the lateral doping profile changes abruptly rather than gradually

(Figure 6.18). To achieve the same or better slow-wave characteristics as those obtained by the gradual doping profile, an optimum lateral width of the doping region must be found. To investigate the effect of different lateral doping widths on the slow-wave characteristics, we have considered two different structures: bulk silicon and semiconductor-on-insulator (SOI). In both cases the p^+ -doping layer is realized by implanting boron ions (B^{2+}) through the photoresist mask window, whereby the size of the window determines the lateral width of the doping region. The added difficulty in this investigation is due to the fact that the doping level changes with penetration depth into the semiconductor and shows a Gaussian-like doping depth profile.

Since the optimized MIS CPW still exhibits considerable losses, the doping region length (in propagation direction of the wave) should be kept to a minimum. This leads inevitably to an abrupt transition between doped and undoped substrate (Figure 6.21 and Figure 6.22) and thus will introduce additional losses. This problem has not been discussed in the literature yet but is very important when slow-wave structures are integrated with other circuit parts. To quantify these losses we have calculated the scattering parameters for such transition. First, by considering only the transition from an undoped to a doped substrate of limited lateral extend and no step in the metal conductor in order to isolate the scattering effect of the doped substrate from that of the metal discontinuity. Second, by including also steps in the conductor widths of the CPW.

To calculate the electromagnetic field in transmission line cross-sections of this kind is very difficult because the doping distribution is inhomogeneous in lateral and vertical direction. While the lateral width of the doping region depends only on the dimensions of the photoresist mask, the (vertical) doping level depth depends on the doping process and shows approximately a Gaussian like profile for which the distribution can be found from the LSS range theory for amorphous targets [81]. Once the doping depth profile is known, the FDTLM method is applied to compute the slow-wave factor, the corresponding losses and the scattering matrix of the transitions. The advantages of the FDTLM method have been discussed in previous chapters. The structures investigated in the following underline again the flexibility of this approach.

6.4.2 Two Types of Coplanar MIS Structure

The geometrical layout of the two types of coplanar MIS structures investigated in this thesis is presented in Figure 6.15 (a) and Figure 6.15 (b), respectively. They are bulk silicon and silicon-on-insulator (SOI) structures. The first step in the analysis is to model the vertical conductivity distribution in the doping layer. Once this is accomplished, the cross-section of the structure is discretized by frequency-domain nodes. Each of these nodes represent the electromagnetic field at that location under the influence of the local material parameters. The FDTLM algorithm then governs the interaction of the electromagnetic field in-between the nodes. First, we outline the approach of how to determine the material parameters.

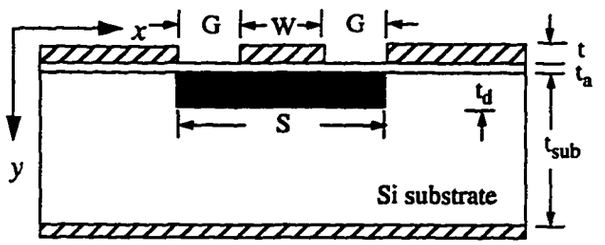

(a) *Bulk Silicon with Gauss Dope Profile structure*

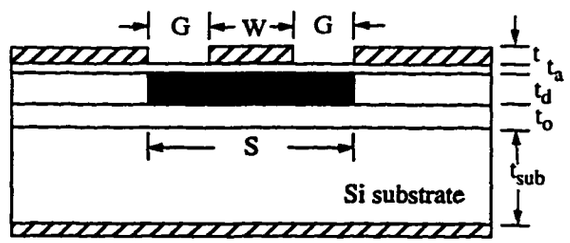

(b) *SOI (Silicon-On-Insulator) Structure*

- Metal - SiO_2 - Silicon

- p^+ Ion-implantation region

Figure 6.15 Cross-sections of two types of micro-sized MIS coplanar waveguides: (a) Bulk silicon and (b) SOI. The doping region is obtained by boron dopant ion implantation at energy levels of 200 keV.

Both structures in Figure 6.15 consist of a thin p^+-doping region separated from the silicon substrate by a thin insulating layer of SiO_2. While in conventional MIS CPW the semiconductor is doped homogeneously over the entire cross-section of the structure, we limit the doping range in lateral direction to the area below the center conductor and the two slots, because this is the area in which the electric field of the fundamental mode is most prominent. The p^+-doping region is fabricated by B^{2+} implantation into the silicon substrate. According to the LSS (the unified theory of atomic stopping by Lindhard, Scharff and Schiott) range theory for amorphous targets [81], the implanted B^{2+} concentration in silicon is approximately a Gaussian distribution function of depth, which may be expressed as

$$N(y) = \frac{D}{\sqrt{2\pi}\Delta Rp}\exp\left[-(y-Rp)^2/\Delta Rp^2\right] \tag{6.20}$$

where D is the total number of ions implanted per unit area, y is the distance measured along the axis of incidence, $N(y)$ is the density of the implanted B^{2+} that stop at the plane x, Rp is the projected range which estimates the depth at which the concentration of implanted dopants reaches its maximum value and ΔRp is the average fluctuation in the projected range. After taking into account diffusion effects that may occur during implantation or during the annealing treatment, Figure 6.16 shows the boron concentration distribution versus depth in silicon by implanting doses of $1x10^{15}$ ions/cm^2 at energy of 200 keV. After the carrier density has been determined, the conductivity profile can be easily converted by using the following empirical expressions for electron and hole mobilities in silicon [83]:

$$\mu_n = \frac{1265}{1+\left[\frac{N}{8.5\times10^{16}}\right]^{0.72}} + \frac{65}{1+\left[\frac{N}{5.0\times10^{20}}\right]^{1.5}} \quad \left(cm^2V^{-1}s^{-1}\right) \tag{6.21}$$

$$\mu_p = \frac{447.3}{1+\left[\frac{N}{1.9\times10^{17}}\right]^{0.76}} + 47.7 \quad \left(cm^2V^{-1}s^{-1}\right) \tag{6.22}$$

where N is the appropriate carrier density in cm^{-3}. Figure 6.17 illustrates the relative

conductivity depth profile of the very thin p^+-doping region (about 2 μm thickness) in the silicon substrate. The parameters of both MIS CPW structures in Figure 6.15 are:

W = 40 μm, G = 25 μm;
SiO_2 layer: t_a = 1000Å, ε_r = 3.9, σ = 0;
Doping region: t_d = 2.0 μm; σ = 30.6 ~ 0.5 S/mm;
SOI structure: t_d = 1 μm, ε_r = 11.8, ρ (SOI resistivity) = 10 Ω-cm, t_o = 2μm;
Si substrate: t_{sub} = 525 μm, ε_r = 11.8, ρ (Si substrate resistivity) = 20 Ω-cm.

It is noted that the conductivity depth profile shown in Figure 6.17 determines the material parameters at the location of the FDTLM nodes. The FDTLM algorithm then models the interaction of the electromagnetic field among the nodes. As we have already seen in the previous chapters that the FDTLM network is considered to be in steady-state where scattering and interconnection occurs simultaneously. The advantage of this approach is that a graded mesh layout with large grading ratio can be chosen because the dimensional parameters are all included in the characteristic impedance and the propagation constant of the FDTLM nodes. This is in particular useful in the present analysis because the very thin inhomogeneous substrate layers that are in close proximity to larger structural details.

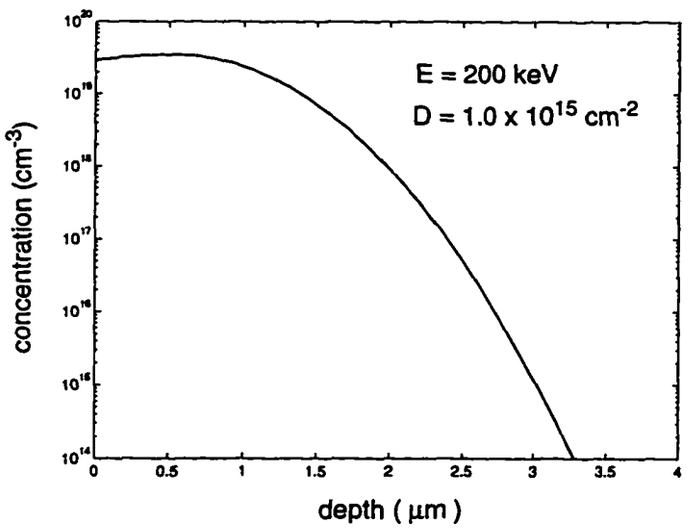

Figure 6.16 Boron ion-implantation distribution in silicon obtained by implanting doses of $1x10^{15}$ B^{2+} ions/cm^2 at energy of 200 keV (after annealing).

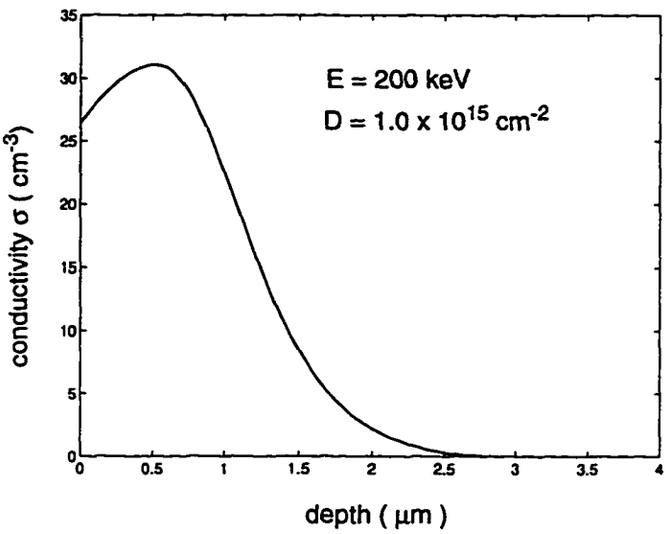

Figure 6.17 The resulting conductivity profile in silicon (p-type) after Baron ion-implantation with doses of $1x10^{15}$ B^{2+} ions/cm^2 at energy of 200 keV (after annealing).

6.4.3 Slow-Wave Propagation in MIS CPW

The structures of the MIS CPW lines investigated in the following are shown in Figure 6.15. They are made from bulk silicon (Figure 6.15 (a)) or SOI (Figure 6.15 (b)). For both structures the doping depth profile shows a Gaussian distribution. Four different lateral doping widths have been investigated as shown in Figure 6.18: (a) S = 0; (b) S=W+2*(G/2); (c) S = W+2*G; (d) S = doping over the entire CPW cross-section. For faster computation, the metallization thickness is assumed to be zero. This affects the results by approximately 1% [82] for a metallization thickness in the range of 1~5 μm. Figure 6.19 illustrates the propagation constant, loss factor and Q-factor of the bulk silicon MIS CPW for the different lateral doping widths of Figure 6.18. Figure 6.20 shows the corresponding results for the SOI MIS CPW. To verify the results, a comparison with the method of lines [79] is included. For both structures it was found that the configuration in Figure 6.18 (c) shows the lowest loss slow-wave mode propagating over the frequency range between 0.7 to 5.0 GHz. The highest slow-wave factor, however, can only be obtained from the structure in Figure 6.18 (d)

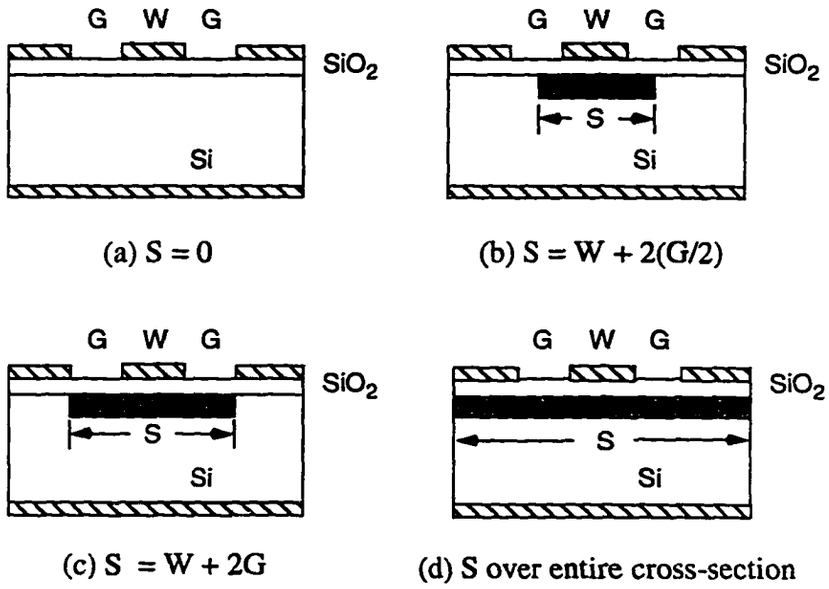

Figure 6.18 Bulk silicon and SOI MIS CPW with four different lateral doping regions.

6.4.3.1 The Bulk Silicon MIS CPW

Figure 6.19 (a) and (b) illustrates that a compromise exists between maximum slow-wave factor and minimum losses. For structure Figure 6.18(c) the maximum attenuation is less than 0.75 dB/mm at 5GHz and less than 0.3dB/mm at 2GHz. At the same time the slowing-factors λ_0/λ_g is between 12.5 ~ 13 with very little dispersion over the frequency range of 0.7 to 5.0 GHz. This slowing factor corresponds to an effective dielectric constant of 156.3 ~ 169.0, which is much larger than the dielectric constant of either the Si substrate or the SiO_2 insulating layer. The losses found with structures Figure 6.18 (c) are less than the data reported in the literatures [74]-[80] for structures with homogeneous doping over the entire transmission line cross-section. Also the quality factor, $Q(= \beta/2\alpha)$, shown in Figure 6.19 (c), reaches a higher value compared to the much larger MIS CPW structures on GaAs [72] or other microstructure CPW MIS transmission lines [75]. The numerical results for the structure in Figure 6.18 (b) are verified by measurements and shown in Figure 6.19. This good agreement indicates that also the other numerical results are a true picture of the physical reality.

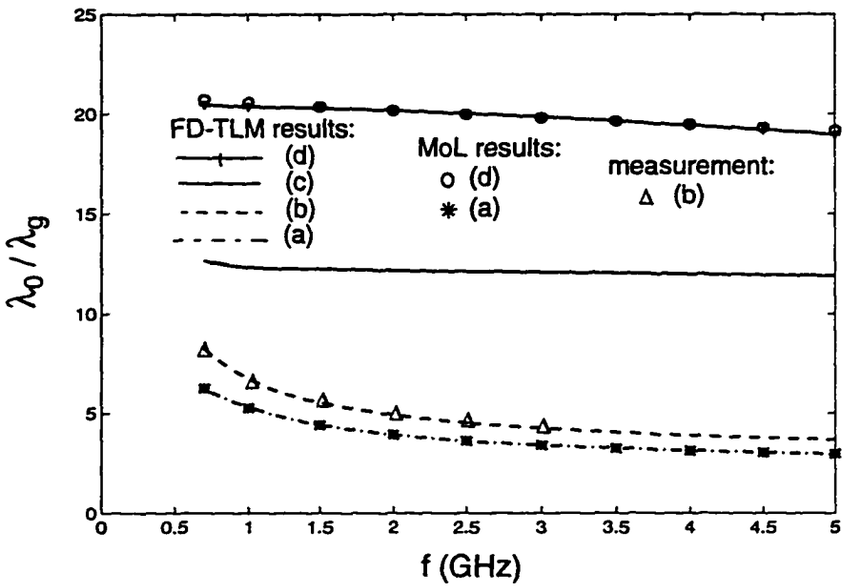

Figure 6.19 (a) Slow-wave factor versus frequency

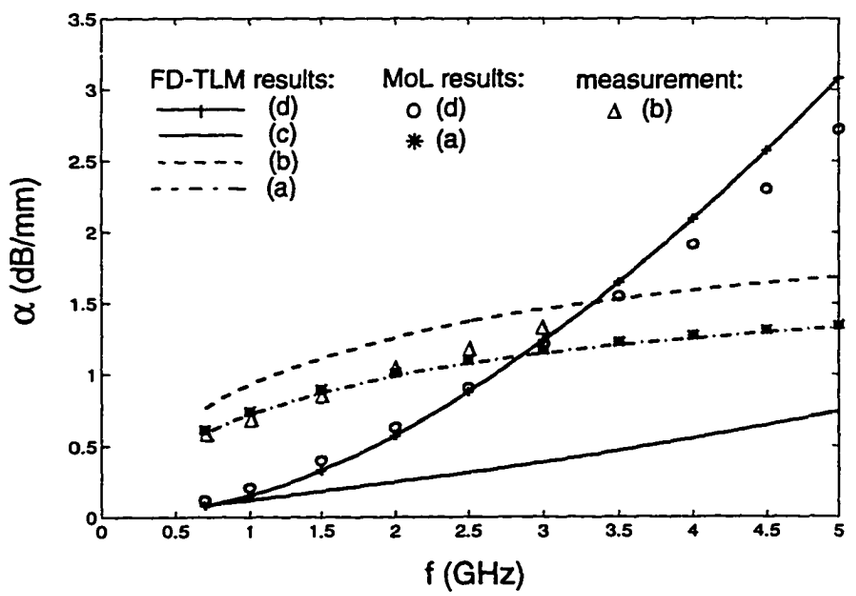

Figure 6.19 (b) Attenuation versus frequency

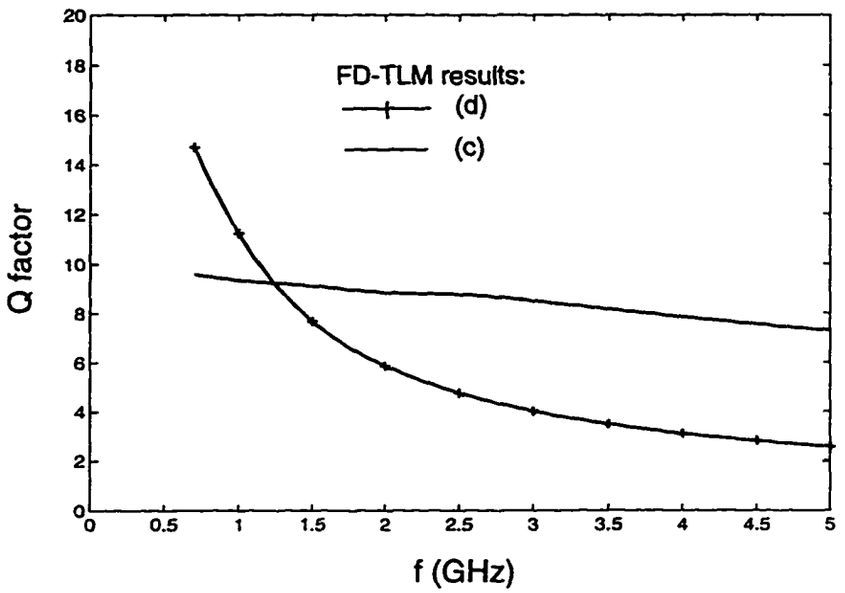

Figure 6.19 (c) Quality factor versus frequency

Figure 6.19 Slow-wave propagation characteristics of bulk silicon MIS CPW with different doping widths, *S*. $W = 40\ \mu m$ and $G = 25\ \mu m$

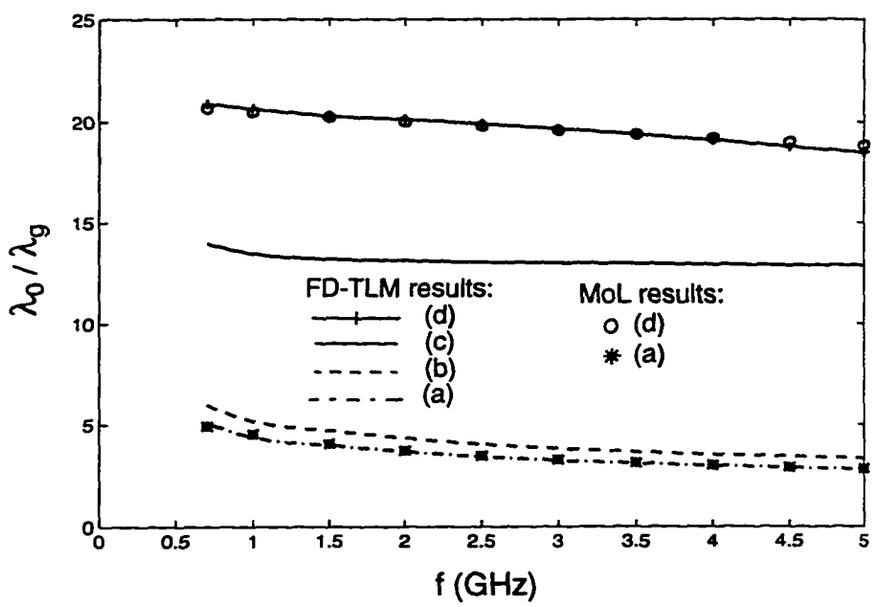

Figure 6.20 (a) Slow-wave factor versus frequency.

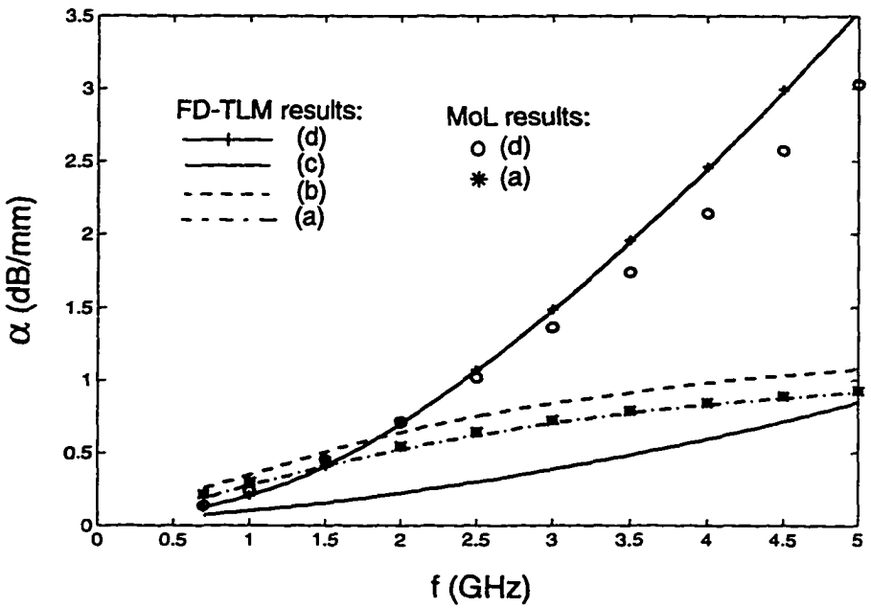

Figure 6.20 (b) Attenuation versus frequency

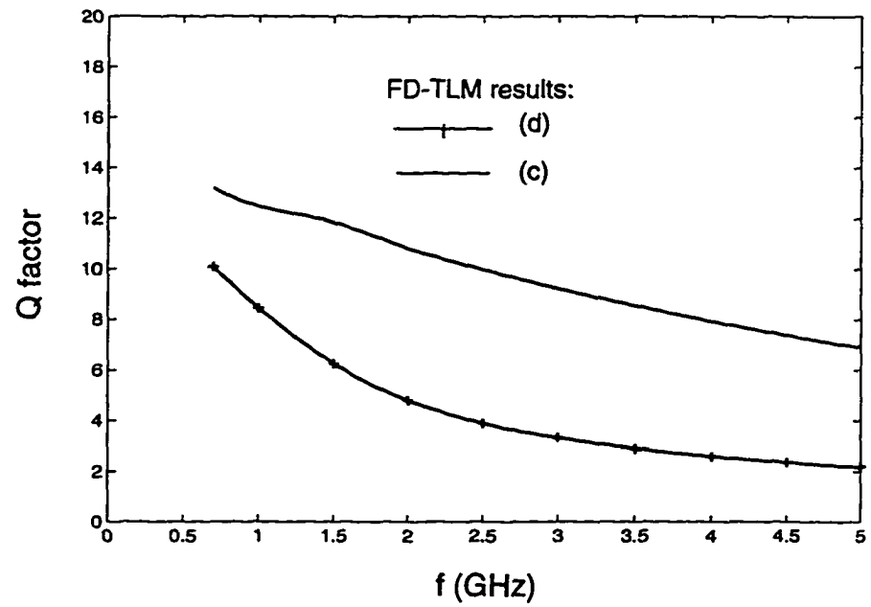

Figure 6.20 (c) Quality factor versus frequency

Figure 6.20 Slow-wave propagation characteristics of SOI MIS CPW with different doping widths, *S*. $W = 40\ \mu m$ and $G = 25\ \mu m$

6.4.3.2 The SOI MIS CPW

Similar characteristics can be observed for the SOI structure shown in Figure 6.20. In comparison with the silicon bulk structure, the slow-wave factor is generally approximately 15% higher and shows somewhat less dispersion. At the same time the attenuation is only 3.5% higher. The introduction of a lossless SiO_2 layer between the doping layer and the high resistivity Si substrate plays an important role in confining the electric field in the insulating layer beneath the coplanar conductors. This may be the reason why SOI structures with selected B^{2+} ion-implantation doping exhibit reasonably large slow-wave factors with little dispersion. The analysis indicates that the SOI structure with a lateral doping width as shown in Figure 6.18 (c) not only provides a better slow-wave factor but the Q-factor is also improved over that of the bulk structure.

6.4.4 Scattering Parameters of the Slow-Wave MIS CPW Discontinuity

Integrating the slow-wave structures of Figure 6.18 (c) and (d) into other circuit parts on undoped substrate results in an abrupt transition between the undoped and the doped silicon as depicted in Figure 6.21. Furthermore, since for a given characteristic impedance the conductor dimension in the slow-wave region is different from the undoped region, also steps in the conductor width must be considered. This is illustrated in Figure 6.22. The structure in Figure 6.21 is investigated first to isolate the effect of the confined doping region from the additional scattering effect introduced by a step discontinuity in the planar conductor.

The FDTLM method has been applied to characterize CPW discontinuities on lossless substrate and good agreement with other techniques and measurements were found. The present problem is more challenging due to the fact that now location-dependent lossy material parameters have to be accounted for in the FDTLM nodes. The S-parameter extraction technique developed for the FDTLM method remains the same and was discussed in the previous section. The MIS CPW section can be considered as a discontinuity region attached to two CPW transmission lines as input and output ports. The intrinsic scattering matrices for the discontinuity region and the two attached semi-

infinite CPW transmission lines are determined from a two-dimensional analysis.

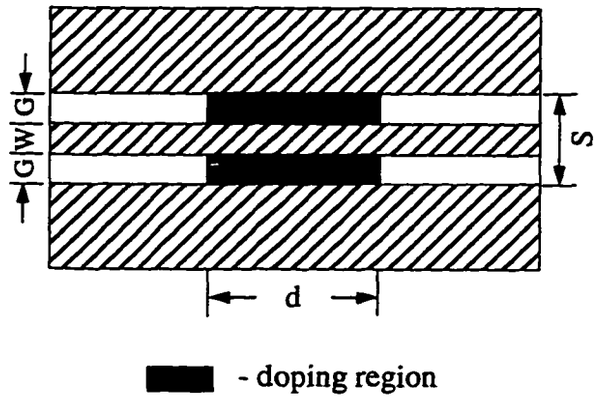

Figure 6.21 Top view of an abrupt discontinuity between undoped CPW on high resistivity silicon and MIS CPW with laterally confined doping region (S = W + 2G).

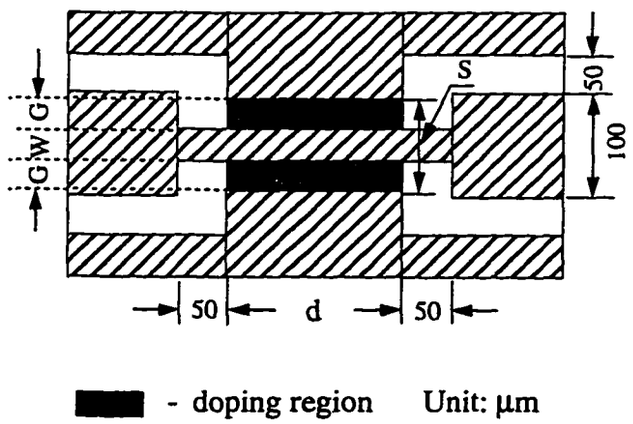

Figure 6.22 Top view of a double-step discontinuity between undoped CPW on high resistivity silicon and MIS CPW (top view) with laterally confined doping region (S = W + 2G).

6.4.4.1 S-Parameters for the Abrupt Transition between the MIS CPW and a CPW on Undoped High-Resistivity Silicon

To illustrate the scattering effects introduced by the transition from undoped to

doped substrate from that due to steps in the conductor widths, we first investigate the structure in Figure 6.21 with a homogeneous conductor dimensions and a lateral doping width of $S=W+2G$. By increasing the length of the doping region and the frequency, Figure 6.23, shows clearly that the transmission coefficient deteriorates significantly and the reflection coefficient exhibits a strong dependency on both parameters. The sensitivity of S_{11} is due to some back reflection from the opposite transition. The effect of the frequency on S_{11} is most likely caused by the skin effect of the doping layer. At higher frequencies (>5GHz) the electric field penetrates much less into the doping layer then at 1GHz. At frequencies higher than 5GHz the doping layer appears like a ground-plane separated by a 0.1μm thick SiO_2 insulating layer. In this case, the electric field is mostly concentrated between the center conductor of the CPW and the doping layer rather than in the 25 μm wide slots between the center conductor and the uniplanar ground plane. Hence, the characteristic impedance is not only very low but the wave encounters a transition from a CPW mode into a microstrip-like mode, which introduces even higher reflections. This explanation is also supported by the two cross points in Figure 6.23, which are the results from an analysis in which the conductivity of the doping layer is increased to that of a lossy conductor.

Figure 6.24 illustrates a comparison between two types of lateral doping widths for the structure in Figure 6.21: homogeneous doping over the entire transmission line cross-section and doping only over the strip and both slot regions. The results clearly indicate that homogeneous doping over the entire cross-section not only lowers the characteristic impedance of this CPW section and thus increases the reflection coefficient, but also increases the overall losses. This observation is in line with our previous conclusion that in order to achieve the lowest loss slow-wave mode, doping over the whole cross-section should be avoided. At the same time one would also achieve a lower reflection coefficient at the transition.

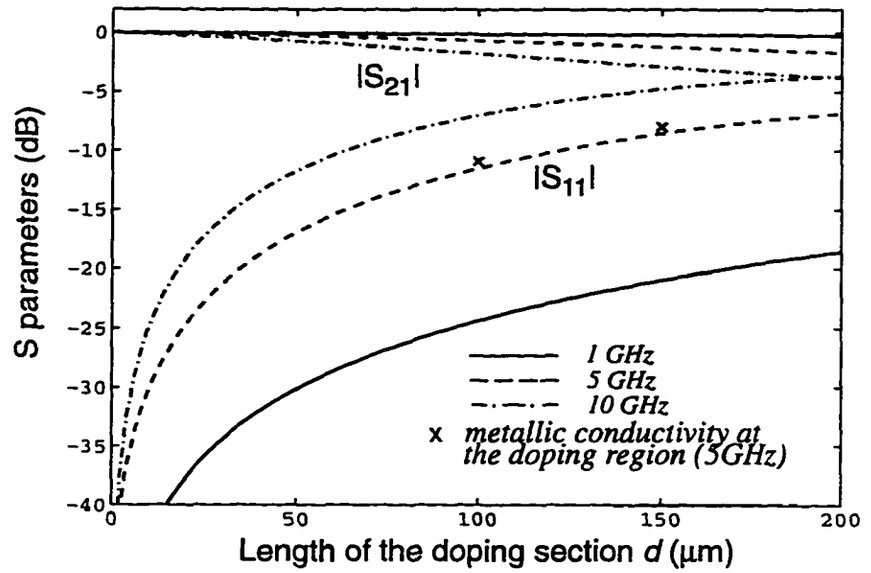

Figure 6.23 S-parameters for the abrupt discontinuity between the undoped CPW and the MIS CPW versus the length of the doping section, *d*, at frequencies 1, 5 and 10 GHz. (S = W + 2G, W = 40 μm, G = 25 μm, t_o = 0.1 mm, t_{sub} = 525 μm, ε_{ro} = 3.9, ε_r = 11.8)

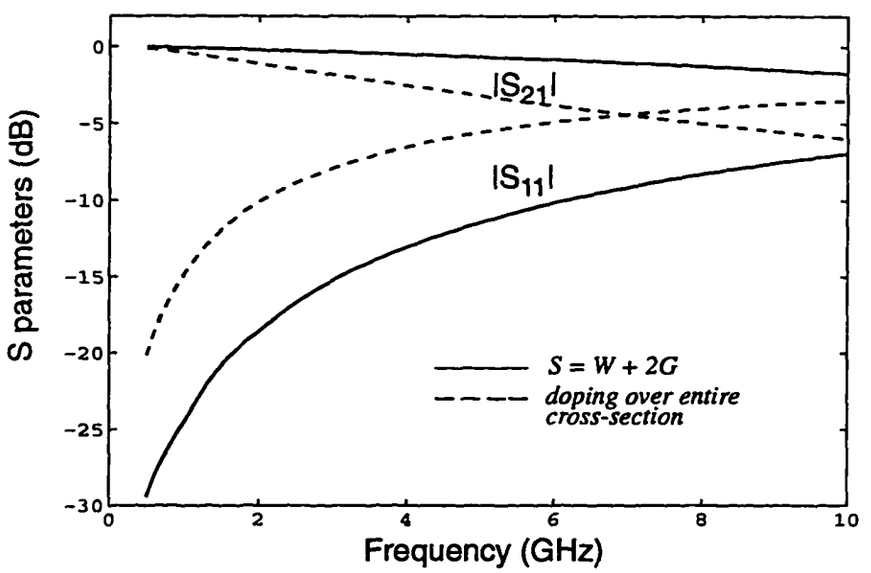

Figure 6.24 S-parameters for the abrupt discontinuity between the undoped CPW and the MIS CPW with different lateral doping widths. (a) $S = W + 2G$ & (b) *doping over entire cross-section*. (d = 100 μm, W = 40 μm, G = 25 μm, t_o = 0.1 μm, t_{sub} = 525 μm, ε_{ro} = 3.9, ε_r = 11.8)

6.4.4.2 Laterally Doped MIS CPW with Double-Step Discontinuity

Figure 6.25 illustrates S-parameters for an MIS CPW with laterally confined doping region ($S=W+2G$) and double-step discontinuity in the conductor and ground-plane (Figure 6.22), as well as for various CPW discontinuities on normal insulating substrate. The dimensions of the conductors on both sides of the discontinuity are designed for 50 Ω in the absence of any doped regions. In the presents of a doped layer, the characteristic impedance in this section drops to less than 5 Ω. The reflection coefficient of such a transition is shown in Figure 6.25 curve a) and c). For comparison, curves d), e) and b) represent transitions between 50Ω–25Ω–50Ω, 50Ω–10Ω–50Ω and 50Ω–50Ω–50Ω CPW transmission lines on insulating substrate, respectively. In particular curve e) seem to suggest that the impedance step between the 50Ω CPW on insulating substrate and the CPW on the doped substrate (curve c) or a)) is much larger than in e). However, as discussed before in conjunction with Figure 6.23, the doped region acts more like a ground-plane to the CPW mode, evidently changing the CPW mode to a microstrip-like mode and thus representing a more pronounced discontinuity to the CPW mode field incident into the discontinuity plane. The reflection coefficient for curve b) clearly indicates that, although both sides of the discontinuity are of 50Ω, the change in the conductor dimensions still represent a discontinuity to the electromagnetic field and thus causing the reflection to occur.

6.4.5 Summary

In this section, a numerical analysis of slow-wave propagation, losses and Q-factor in bulk silicon and semiconductor-on-insulator (SOI) MIS CPW has been pursued, including the characterization of field scattering. The analysis is based on the frequency-domain TLM method. It was found that large slowing factors at low losses can be achieved by optimizing the lateral extent of the semiconductor doping region. It was furthermore found that SOI structures show better Q-factor with less dispersion than the bulk silicon structures. Scattering effects at abrupt transitions between MIS CPW and undoped CPW discontinuities have been investigated as well. It was furthermore shown that, for the circuit dimensions investigated here, the transition from undoped to doped

region introduces a much larger effect on the scattering parameters than the conductor discontinuities. This is due to fact that the doping region not only introduces a very low characteristic impedance with correspondingly high reflection coefficient, but that the doping layer acts also as a lossy ground plane in close vicinity to the center conductor of the CPW and, thus, obviously changing the CPW mode to a microstrip-like mode in that region. This change in the field pattern introduces additional reflections that can not be explained by only considering the impedance step between the doped and undoped CPW section.

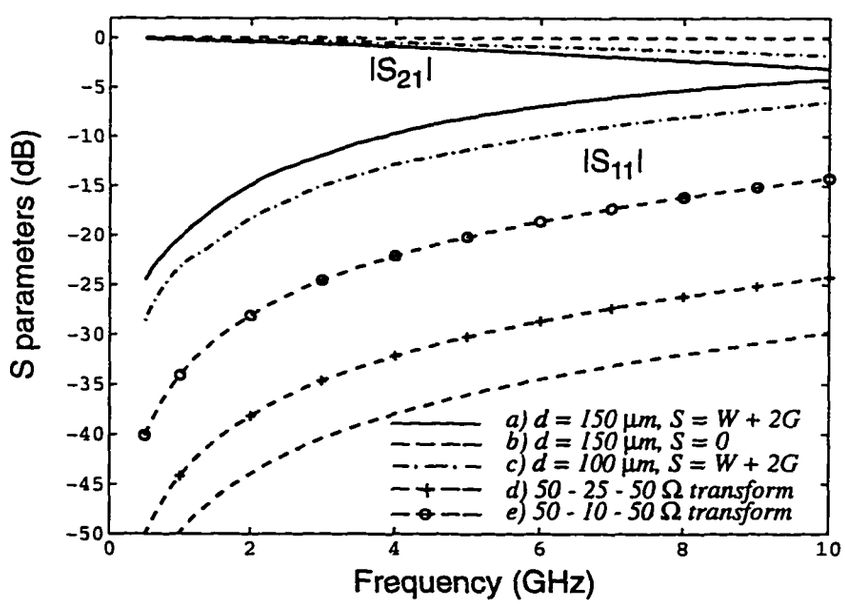

Figure 6.25 S-parameters for the double-step discontinuity. (d = 100 µm & 150 µm, W = 40 µm, G = 25 µm, t_o = 0.1 µm, t_{sub} = 525 µm, ε_{ro} = 3.9, ε_r = 11.8)

Chapter 7

Conclusions

7.1 Overall Discussion and Conclusion

The objective of this dissertation was to develop a methodology to extend the frequency-domain transmission line matrix (FDTLM) method to semiconductor-based microwave transmission line structures. These guided wave structures include a semiconductor laser diode and coplanar metal-insulator-semiconductor (MIS) coplanar waveguide (CPW). The main difference of these structures from the normal microstrip and coplanar waveguide is that they include multilayer semiconductor substrates. Therefore, these structures are lossy and inhomogeneous. The ratio of the layer thickness is usually more then 100. This type of transmission line configuration typically exhibits lossy slow-wave propagation characteristics. The theoretical analysis of such complicated structures is not possible using a single numerical technique. In this dissertation, therefore, a mixture of numerical techniques is applied to deal with this very challenging issue. First, a combination of the complex finite different method for consistently solving the device physics and then the frequency-domain transmission line matrix (FDTLM) method for the electromagnetic field problem is used to analyze semiconductor lasers and its interconnection with a normal microwave transmission line. Subsequently, a numerical analysis of MIS CPW slow-wave propagation in bulk silicon and semiconductor-on-insulator (SOI) MIS CPW has been performed. The analysis is based solely on the frequency-domain TLM method.

In Chapter 2 the development of the complex finite difference approach has been

described. This method is used to model the semiconductor laser as an active optical waveguide. The self-consistent algorithm solves the bias-dependent electric and optical characteristics of the devices with non-uniform strip discontinuity. It was found that the strip discontinuity not only significantly changes the refractive index in the active layer but also changes the optical behavior of the device. The important feature here is that the conductivity profile in the active layer varies with the biasing. This conductivity profiles can then be used as input parameter for the field theoretical analysis.

In the frequency-domain TLM approach, the three-dimensional (3D) space is modeled by a network of transmission lines known as the frequency-domain symmetrical condensed node (SCN), which has been considered as the core of the FDTLM method. The main work here was concentrated on the development and application of this method. As seen in Chapter 3, by using the simple and elegant empirical method proposed by Naylor and Ait-Sadi, adopting a new port numbering of the SCN, the 12-port scattering matrix at the center of the node has been rewritten. Unlike Johns [34] original derivation, The above derivation avoids the solution for a set of non-linear simultaneous equations, which is a tedious task. According to the FDTLM basic notation and the SCN's constitutive relations, the characteristic impedances and propagation constants of the link lines have been determined. The scattering matrix has been transferred from the nodal center to the ports leading to the different representations of the SCN in the frequency domain. It has been shown that the port scattering matrix well describes the scattering properties of a FDTLM symmetrical condensed nodes in the frequency domain.

After introducing the equivalent relation between the field components and the voltage waves, the derivation of the frequency-domain TLM SCN directly from Maxwell's equations by using centered differencing and averaging has been developed. Based on this derivation, a full equivalence between the TLM method and the symmetrical condensed node as well as the finite difference method based on Maxwell's equations has been established. From the equivalent network modeling perspective, the lossy stub-loaded (LSL) SCN is consistent with this derivation if the physical concept of

the normalized admittances and impedances to represent the electric and magnetic losses, respectively, is introduced. This lossy stub-loaded (GLSL) symmetrical condensed node in the frequency domain is an additional contribution to the FDTLM approach.

It is well known that dispersion errors are present if a spatial discretization scheme is used to model electromagnetic field problems. A detailed investigation of dispersion characteristics with the different frequency-domain SCNs was undertaken. The results were compared to the different uniform and graded meshes from other frequency-domain nodes. At the same time this dispersion analysis also takes the material parameters into account. It was found that the hybrid frequency-domain nodes have a better propagation characteristics than the other FDTLM nodes.

As mentioned in the beginning, a field theoretical analysis of the microwave effects in semiconductor-based guided wave structures was the main topic of this dissertation. The new development of the FDTLM method provides the means for accomplishing this goal. Two main problems were investigated: First, we demonstrated a field theoretical analysis of the distributed microwave effects in semiconductor lasers by using the frequency-domain TLM method. From the microwave perspective, the physical model for the semiconductor laser diode was considered a lossy and slow-wave microstrip transmission line with multi-layer inhomogeneous substrate. The conductivity in the active layer is bias-dependent and was found from a complex finite difference self-consistent solution described in Chapter 2. The results from this analysis was then used as input parameter for the FDTLM simulation. It was found that the attenuation factor, phase velocity and characteristics impedance of the semiconductor lasers so calculated are in good agreement with the measured data for both the forward and unbiased semiconductor lasers. Furthermore, the electrical performance of flip-chip and bond wire (or airbridge) transitions between passive microwave transmission lines and laser diodes has been investigated. A detailed discussion was conducted in Chapter 6. It was found that in case of interconnecting a low impedance laser diode with a 50 Ω CPW or microstrip, the flip-chip transition was better than an airbridge/bond wire transition.

Second, a field theoretical analysis of MIS CPW slow-wave structures in bulk silicon and semiconductor-on-insulator (SOI) has been investigated, This investigation also includes the characterization of the electromagnetic field scattering at the MIS CPW discontinuities. The analysis is based on the frequency-domain TLM method. It was found that there exist an optimum lateral doping width which provides not only a maximum slowing factor with low losses, but also provides the best scattering parameters at the transition from the undoped to doped CPW section.

Overall, the research presented in this dissertation is an important step towards more efficient numerical modeling of most general electromagnetic field problems in the frequency domain. By adding new features and combining the method with other numerical techniques, the FDTLM method has shown a great potential as a very efficient and flexible numerical tool in the analysis of semiconductor-based guided wave structures.

7.2 Suggested Future Research

In order to expand the scope of the FDTLM method, the future research should include the following aspects:

- **Open boundaries**: So far, in the FDTLM simulation we consider the electric or magnetic boundaries surrouding the compositional space. For the scattering problems, open boundaries are important. Open boundaries may be approximated by terminating the link lines adjacent to the boundary with a matched load. In the frequency domain this may be achieved by implementing a zero reflection coefficient at the link line boundary.

- **Node for a 90-degree bend**: Although the FDTLM approach has originally been developed for two-port network problems, the intrinsic scattering matrix describes a plane sheet in the structure. A two-port structure with a bend in the transmission line can not be handled. One option to solve this problem is to reformulate the intrinsic scattering matrix. An alternative solution is to develop a corner node to model this special application.

- **Cylindrical coordinate**: Cylindrical microwave structures such as circular waveguide bandpass filters are extensively used in microwave circuits. To simulate these structures, traditional FDTLM schemes with cylindrical coordinates are used. But they can not avoid the problem caused at the center of the grid, which represents a singularity for the node with unknown field distribution. Further research would be concentrated on the problem regarding node interconnections at the center region instead of putting a short-circuit (E-wall) or open-circuit (M-wall) boundary. This requires to develop a spider leg type node at the center region to increase the accuracy of the FDTLM method and to solve this particular electromagnetic field problem.

- **Modeling of anisotropic media**: In this dissertation, all applications are associated with inhomogeneous semiconductor substrates. The formulation of the FDTLM nodes, presented in this dissertation, should be generalized further to model anisotropic media described by non-diagonal tensors for the permeability and permittivity of material.

References

[1] T. Itoh, "Numerical techniques for microwave and millimeter-wave passive structures," John Wiley & Sons, New York, 1989.

[2] M.N.O. Sadiku, "Numerical techniques in electromagnetics," CRC Press, 1992.

[3] P.B. Johns and R.L. Beurle, "Numerical solution of 2-dimensional scattering problems using a transmission-line matrix," Proc. IEE, 1971, 118, (9), pp. 1203-1208.

[4] W.J.R. Hoefer, "The transmission line matrix (TLM) method", in Numerical Techniques for Microwave and Millimeter Wave Passive Structures, T. Itoh, Ed. New York, Wiley, 1989.

[5] Brewitt-Taylor, C.R. and P.B. Johns "On the construction and numerical solution of transmission line and lumped network models of Maxwell's equations", International Journal for Numerical Methods in Engineering 15, pp.13-30, 1980.

[6] H. Jin and R. Vahldieck, "The frequency-domain TLM method," 1992 IEEE Int. Microwave Symp. Dig., pp. 775-778, June 1992.

[7] H. Jin and R. Vahldieck, "The frequency-domain transmission line matrix method -- A new concept," IEEE Trans. Microwave Theory Tech., vol. MTT-40, pp. 2207-2218, Dec. 1992.

[8] D. P. Johns, A. J. Wlodarczyk, A. Mallik, and C. Christopoulos, "New TLM technique for steady-state field solutions in three dimensions," Electron. Lett., vol. 29, no. 18, pp.1692-1694, 1992.

[9] H. Jin and R. Vahldieck, "Direct derivations of TLM symmetrical condensed node and hybrid symmetrical condensed node from Maxwell' equations using centered differencing and averaging," IEEE Trans. Microwave Theory Tech.,vol. MTT-42, pp. 2554-2561, Dec. 1994.

[10] S. Weisser, J.D. Ralston, E.C. Larkins, I.Esquivas, P.J. Tasker, J. Flessner, and J. Rosensweig, "Efficient high-speed direct modulation in p-doped $In_{0.35}Ga_{0.65}As$/ GaAs multiquantum well lasers," Electron. Lett., vol. 28, pp. 2141-2143, 1992.

[11] L.F. Lester, S.S. O'Keefe, W.J. Schaff, and L.F. Eastman, "Multiquantum well strained-layer lasers with improved low frequency response and very low dumping," Electron. Lett., vol. 28, pp. 383-385, 1992.

[12] D. Tauber, R. Spickermann, R. Nagarajan, T.E. Reynolds, A.L. Holmes, Jr., and J.E. Bowers, "Distributed microwave effects in high speed semiconductor

lasers," 1994 IEEE Int. Microwave Symp. Dig., pp. 49-51, 1994.

[13] S.M. Sze, Physics of Semiconductor Devices, Second Edition, John Wiley & Sons, 1981.

[14] T. Ohtosh, K. Yamaguchi, C. Nagaoko, Y. Murayama, and N. Chinone, "A two-dimensional devices simulation of semiconductor laser," Solid-State Electron., Vol. 30, pp. 627-638, 1987.

[15] G.L. Tan, N. Bewtra, K. Lee, and J.M. Xu, "A two-dimensional nonisothermal finite element simulation of laser diodes," IEEE J. Quantum Electron., Vol. 29, pp. 822-835, 1993.

[16] R. Stratton, "Diffusion of hot and cold electrons in semiconductor barriers," Phys. Rev., vol. 126, no. 6, pp. 65-87, 1982.

[17] S.P. Gaur and D.H. Navon, "Two dimensional carrier flow in a transistor structure under nonisothemal conditions," IEEE Trans. Electron Device, vol. ED-23, pp. 50-57, 1976.

[18] H.C. Casey, Jr. and M.B. Panish, Heterostructure Lasers, Part A: Fundamental Principles, Academic Press, New York, 1978.

[19] D.P. Wilt and A. Yariv, "A self-consistent static model of the double-heterostructure laser," IEEE J. Quantum Electron., vol. 17, pp. 1941-1949, 1981.

[20] T. Kumar, R.F. Ormondroyd, and T.E. Rozzi, "A self-consistent model of the lateral behavior of a twin-stripe injection laser," IEEE J. Quantum Electron., Vol. 22, pp. 1975-1985, 1986.

[21] T. Kumar, R.F. Ormondroyd, and T.E. Rozzi, "Numerical solution of lateral current spreading and diffusion in near-threshold DH twin-stripe lasers," IEEE J. Quantum Electron., Vol. 21, pp. 421-433, 1985.

[22] S.M. Lee, S.L. Chuang, R.P. Bryan, C.A. Zmudzinski, and J.J. Coleman, "A self-consistent model of a nonplanar quantum-well periodic laser array," IEEE J. Quantum Electron., Vol. 27, pp. 1886-1899, 1991.

[23] W.B. Joyce and R.W. Dixon, "Analytic approximations for the Fermi energy of an ideal Fermi gas," Appl. Phys. Lett., Vol. 31, pp. 354-356, 1977.

[24] B.W. Hakki, "Carrier and gain spatial profiles in GaAs stripe geometry lasers," J. Appl. Phys., Vol. 44, pp. 5021-5028, 1973.

[25] E.A.J. Marcatili, "Dielectric rectangular waveguide and directional coupler for integrated optics," Bell Syst. Tech. J., Vol. 48, pp. 2071-2102, 1969.

[26] M. Koshiba, H. Saitoh, M. eguchi, and K. Hirayama, "Simple scalar finite element approach to optical rib waveguides," IEE Proc. J., Vol. 139, pp. 166-171, 1992.

[27] M.A. Matin and T.M. Benson, "New technique for finite difference analysis of optical waveguide problems," International J. Numerical Modeling: Electron.

Networks, Devices and Fields, Vol. 7, pp. 25-33, 1994.

[28] T.M. Benson, R.J. Bozeat, and P.C. Kendall, "Finite difference analysis of active optical waveguide devices," IEE 2nd International Conference on Computation in Electromagnetics, pp. 162-165, 1994.

[29] N. Mabaya, P.E. lagasse and P. Vamdenbulcke, "Finite-element analysis of optical waveguides," IEEE Trans. Microwave Theory Tech., Vol. 29, pp. 600-605, 1981.

[30] M. Koshiba, K. Hayata and M. Suzuki, "Approximate scalar finite-element analysis of anisotropic optical waveguides," Electron. Lett., Vol. 18, pp. 411-413, 1982.

[31] M.S. Stern, "Semivectorial polarised finite difference method for optical waveguides with arbitrary index profiles," IEE Proc. J, Vol. 135, pp. 56 - 63, 1988.

[32] S. Akhtarzad and P. B. Johns, "Solution of Maxwell's equations in three space dimensions and time by the TLM method of analysis," Proc. Inst. Elec. Eng., Vol. 122, pp. 134-1348, 1975.

[33] P. Saguet and E. Pic, "Utilization d'un nouveau type de noeud dans la methode TLM en trois dimensions," Electron. Lett., Vol. 18 pp. 478-480, 1982.

[34] P. B. Johns, "A symmetrical condensed node for the TLM method," IEEE Trans. Microwave Theory Tech., vol. MTT-35, pp. 370-377, 1987.

[35] J. Huang, R. Vahldieck and H. Jin, "Fast frequency-domain TLM analysis of 3-D circuit discontinuities," Proc. 9th Annual Review of Progress in Applied Computational Electromagnetics Symp., pp. 475-481, Mar. 1993.

[36] M. Krumpholz and P. Russer, "A field theoretical derivation of TLM", IEEE Trans. Microwave Theory Tech., vol. MTT-42, pp. 1660-1668, Sept., 1994.

[37] J. Huang, "Frequency domain transmission line matrix method and its applications to electromagnetic analysis," Ph. D. dissertation, University of Victoria, Canada, Aug. 1995.

[38] S. Chen and R. Vahldieck, "A new hybrid symmetrical condensed node for frequency-domain TLM method," 1996 IEEE Int. Microwave Symp. Dig., pp. 427-430, San Francisco, California, USA.

[39] S. Chen and R. Vahldieck, "Accuracy considerations of a class of frequency-domain TLM nodes," Proc. 12th Annual Review of Progress in Applied Computational Electromagnetics Symp.(ACES), pp.279-286, March 1996.

[40] D.A. Al-Mukhtar and J.E. Sitch, "Transmission-line matrix method with irregularly graded space", Proc. IEE, Vol 128, Pt. H, No. 6, Dec. 1981, pp.299-305.

[41] P. Naylor and R. Ait-Sadi, "Simple method for determining 3D TLM nodal

scattering in nonscalar problems'', Electronics Letters, Vol. 28(No.25), pp 2353-2354, Dec. 1992.

[42] V. Trenkic, C. Christopoulos and T. M. Benson, "New symmetrical super-condensed node for the TLM method", IEE Electronics Letters vol. 30, No. 4, pp. 329-330, Feb. 1994.

[43] C. Christopoulos, "The transmission-line modeling method," Series on Electromagnetic Wave Theory, IEEE/OUP Press, 1995.

[44] J. Herring, "Developments in the transmission-line modelling method for electromagnetic compatibility studies," Ph. D. dissertation, University of Nottingham, UK, May 1993.

[45] R. Scaramuzza and A.J. Lowery, ''Hybrid symmetrical condensed node for the TLM method''. Electronics Letters, Vol. 28(No. 23), pp 1947-1949, Nov. 1990.

[46] V. Trenkic, C. Christopoulos and T. M. Benson, "New symmetrical super-condensed node for the TLM method", IEE Electronics Letters vol. 30, No. 4, pp. 329-330, Feb. 1994.

[47] V. Trenkic, "The development and characterization of advanced nodes for the TLM method," Ph. D. dissertation, University of Nottingham, UK, Nov. 1995.

[48] H. Jin and R. Vahldieck, "A new frequecy-domain TLM symmetrical condensed node derived directly from Maxwell equations," 1995 IEEE Int. Microwave symp. Dig., pp. 487-490.

[49] M. Krumpholz, P. Russer and H. Zscheile, ''The derivation of the condensed symmetric TLM node from Maxwell's equations'', PIERS 1993, Pasadena, CA, July 1993, P. 150.

[50] Z. Chen, M. N. Ney, and W. J. R. Hoefer, "A new finite-differnce time-domain formulation and its equivalence with the TLM symmetrical condensed node," IEEE Trans. Microwave Theory Tech.,vol. MTT-39, pp. 2160-2169, Dec. 1991.

[51] P. Russer and M. Krumpholz, ''The Hilbert space formulation of the TLM method'', International Journal of Numerical Modelling, (Electronic Networks, Devices and Fields), Vol. 6, pp.29-45, 1993.

[52] M. Krumpholz, P. Russer, Q. Zhang and W.J.R. Hoefer, "Field-theoretic foundation of two-dimensional TLM based on a rectangular mesh", in IEEE MTT-S Intl. Microwave Symposium 1994 Digest, pp. 333-335, 1994.

[53] Q. Zhang, "Development and characterization of generalized TLM networks for electromagnetic modeling," Ph. D. dissertation, University of Victoria, Canada, March 1996.

[54] P. Naylor and R. A. Desai, "New three dimensional symmetrical dondensed lossy node for solution of electromagnetic wave problems by TLM," Electronics Lett. Vol. 26 (7), pp. 492-493, March 1990.

[55] F. J. German, G. K. Gothard, and L. S. Riggs,"Modelling of materials with electric and magnetic losses with the symmetrical dondensed TLM method," Electronics Lett. Vol. 26 (16), pp. 1307-1308, Aug. 1990.

[56] C. Huygens, "Traité de la Lumière", Leiden, 1690, Pierre vander Aa, reprinted in "Oevres Complètes de Christiaan Huygens", Société Hollandaise des Sciences, Vol. 19, Amsterdam 1967, Swets and Zeitlinger.

[57] J. Nielsen and W.J.R. Hoefer, "A complete dispersion analysis of the condensed node TLM mesh", IEEE Trans. on Mag. Vol.27, No 5, pp3982-3985, Sept. 1991.

[58] J. Nielsen and W.J.R. Hoefer, "Effects of dispersion in the 3D condensed node TLM mesh", in IEEE MTT-S Intl. Microwave Symposium Digest, pp. 1221-1223., 1992.

[59] J. Nielsen and W.J.R. Hoefer, "Generalized dispersion analysis and spurious modes of 2-D and 3-D TLM formulations," IEEE Trans. Microwave Theory Tech., Vol. 41, No. 8, pp. 1375-1384, Aug. 1993.

[60] R. E. Collin, "Foundations for microwave engineering", McGraw-Hill, 1966.

[61] D. P. Johns and C. Christopoulos, "dispersion of time-domain and frequecy-domain formulations of the symmetrical condensed TLM node," 2nd Intl. Conf. on Computation in Electromagnetics, pp. 295-298, Nottingham, NK, Apr. 1994.

[62] J. Nielsen, "TLM analysis of microwave and millimeter wave structures with embedded nonlinear devices," Ph. D. dissertation, University of Ottawa, Canada, 1992.

[63] T. Becks and I. Wolff, 'Analysis of 3D metallization structures by a full wave spectral domain technique', IEEE Trans. Microwave Theory Tech., vol. MTT-40, pp. 2219-2227, Dec. 1992.

[64] M. Drissi, F. Hanna, and J. Citerne, "Theoretical and experimental investigations of open microstrip gap discontinuities", Proc. European Microwave Conf., Stockholm, 1988.

[65] H. Hasegawa, M. Furukawa, and H. Yanai, "Properties of microstrip on Si-SiO2 system," IEEE Trans. Microwave Theory Tech., Vol. 19, No. 11, pp 869-881, Nov. 1971.

[66] H. Jin, R. Vahldieck, H. Minkus, and J. Huang, "Rigorous field theory analysis of flip-chip interconnections in MMICs using the FDTLM method," 1994 IEEE Int. Microwave Symp. Dig., pp. 1711-1714, June 1994.

[67] H. Jin, R. Vahldieck, and H. Minkus, "FDTLM analysis of flip-chip interconnections," 24th European Microwave conference Digest, pp. 1259-1264, 1994.

[68] F. Alimenti, U. Goebel, and R. Sorrentino, "Quasi static analysis of microstrip bondwire interconnections," 1995 IEEE Int. Microwave Symp. Dig., pp. 679-

682, May 1995.

[69] R. Vahldieck, S. Chen, H. Jin, and P. Russer, "Field theory analysis of distributed microwave effects in high speed semiconductor lasers and their interconnections with passive microwave transmission lines," 1995 IEEE Int. Microwave Symp. Dig., pp. 861-864, May 1995.

[70] R. Vahldieck, S. Chen, H. Jin, and P. Russer, "Flip-chip and bond wire/airbridge transitions between passive microwave transmission lines and laser diodes," 25th European Microwave conference Digest, 1995.

[71] R. H. Caverly, "Characteristic impedance of integrated circuit bond wires," IEEE Trans. Microwave Theory Tech., Vol. 34, No. 9, pp 982-984, Sept. 1986.

[72] H. Hasegawa and H. Olizaki, "MIS and Schottky slow-wave coplanar striplines on GaAs substrates," Electron. Lett., vol. 13, no. 22, pp. 663-664, Oct., 1977.

[73] Y. Fukuoka, Y. Shih, and T. Itoh, "Analysis of slow-wave coplanar waveguide for monolithic integrated circuits," IEEE Trans. Microwave Theory Tech., vol. MTT-31, pp. 567-573, July 1983.

[74] R. Sorrentino, G. Leuzzi, and A. Silbermann, "Characteristics of metal-insulator-semiconductor coplanar waveguides for monolithic microwave circuits," IEEE Trans. Microwave Theory Tech., vol. MTT-32, pp. 410-415, Apr. 1984.

[75] C. Seguinot, P. Kennis, P. Pribetich, and J. P. Villotte, "MIS slow-wave coplanar line: a comparison of theoretical and experimental characteristics," Proc. 16th European Microwave Conf. (Dublin), pp. 445-446, 1986.

[76] T. C. Mu, H. Ogawa, and T. Itoh, "Characteristics of multiconductor asymmetric slow-wave microstrip transmission lines," IEEE Trans. Microwave Theory Tech., vol. MTT-34, pp. 1471-1477, Dec. 1986.

[77] Y. R. Kwon, V. M. Hietala, and K.S. Champlin, "Quasi-TEM analysis of slow-wave mode propagation on coplanar microstructure MIS transmission lines," IEEE Trans. Microwave Theory Tech., vol. MTT-35, pp. 545-551, June 1987.

[78] K. Wu, "New prospective coplanar metal-insulator-semiconductor (MIS) monolithic structure," Electron. Lett., vol. 24, no. 5, pp. 262-264, Mar. 1988.

[79] K. Wu and R. Vahldieck, "Propagation characteristics of MIS transmission lines with inhomogeneous doping profile," IEEE Trans. Microwave Theory Tech., vol. MTT-38, pp. 1872-1878, Dec. 1990.

[80] K. Wu and R. Vahldieck, "Hybrid-mode analysis of homogeneously and inhomogeneously dope low-loss slow-wave coplanar transmission lines," IEEE Trans. Microwave Theory Tech., vol. MTT-39, pp. 1348-1360, Aug. 1991.

[81] J. W. Mayer, L. Eriksson, and J. A. Davies, *Ion Implantation in Semiconductors*, Chapter 2, Academic Press, New York, 1970.

[82] K. Beilenhoff, H. Klingbeil, W. Heinrich, and H. L. Hartnagel, "Open and short

circuits in conplanar MMIC's," IEEE Trans. Microwave Theory Tech., vol. MTT-41, pp. 1534-1537, Sep. 1983.

[83] P. Blood and J. W. Orton, "The electrical characterization of semiconductors: majority carriers and electron states," Academic Press, 1992.